Design and Fabrication of Nanostructures by Layer-by-Layer Assembly for Organic Photovoltaic Devices

Kohji MASUDA

2010

Contents

Chapter 1. General Introduction

Part I

Chapter 2. Fabrication and Conductive Properties of Multilayered Ultrathin Films Designed by Layer-by-Layer Assembly of Water-Soluble Fullerenes

Chapter 3. Conductive and Photovoltaic Properties of Multilayered Ultrathin Films Designed by Layer-by-Layer Assembly of Titanium Oxides

Part II

Chapter 4. Exiton Generation and Diffusion in Multilayered Organic Solar Cells Designed by Layer-by-Layer Assembly of Poly(*p*-phenylenevinylene)

Chapter 5. Solution-Processed Multilayered Polymer Solar Cells Designed by Layer-by-Layer Assembly of Poly(*p*-phenylenevinylene)s with Dimethylsulfoxide

Chapter 6. Hybrid Solar Cells of Layer-by-Layer Thin Film with Polymer/Fullerene Bulk Heterojunction

Chapter 1

General Introduction

1.1. Background and Motivation

Organic semiconductors such as π-conjugated polymers and small molecules exhibit tunable conductivity ranging from insulator to metallic level,[1,2] although most of conventional organic materials are insulators. Furthermore, some of them exhibit superconductivity.[3–6] Such conductivity is due to π-conjugation system of organic molecules, which serves as conductive pathways of freely mobile charged carriers generated: either by removing electrons from (oxidation), or inserting them into (reduction), the material. The remarkable progress in conductive organic materials was triggered by the discovery of conjugated polymers[7–9] and fullerenes.[10–12] Consequently, novel applications such as electromagnetic shielding of circuit, anti-static coating, and various electronic devices have been made. On the other hand, the π-conjugation raises the highest occupied molecular orbital (HOMO) level and lowers the lowest unoccupied molecular orbital (LUMO) level, resulting in a smaller bandgap. Consequently, typical organic semiconductors have absorption and emission bands in the visible region.[13,14] Therefore, organic semiconductors have drawn much attention for not only their excellent conductive properties but also their unique optical properties.

Recently, organic semiconductors have been intensively studied as key materials in organic electronic or optoelectronic devices such as organic light-emitting diodes (OLED),[15–18] organic field-effect transistors (OFET),[19–23] memory devices,[24,25] and organic photovoltaic cells.[26–33] Various electronic devices have marvelously improved our lives in the last decade, and will make them much more convenient on demand. The main parts of the present electronic/optoelectronic devices are made of metals and inorganic semiconductors such as silicon and germanium. These materials are stable and reliable in air and even at high temperatures. On the other hand, organic semiconductors are excellent features such as flexibility, light-weight, processability, and ease of chemical modification. The former points of these features are relating to good portability and smart design. The ease of chemical modification is of great importance for tuning properties such as conductivity and solubility. Furthermore, electronic/optoelectronic devices based on organic semiconductors can be fabricated simply by solution processes such as printing and coating techniques.[34–36] This is a great advantage for low-cost manufacturing due to large-area, high-throughput, and low-temperature processing.

Organic photovoltaic cells are one of the most important applications to organic optoelectronic devices. Photovoltaic cells are a clean and sustainable source of energy and are therefore expected to play an important role in global energy issues. Photovoltaic cells based on inorganic materials have been developed in the last few decades. These photovoltaic cells are already used commercially. On the other hand, photovoltaic cells based on organic materials have been actively studied as next-generation photovoltaic cells.[26–33] Compared to inorganic photovoltaic cells, organic photovoltaic cells are inferior in device performance at this moment. However, as mentioned above, have great advantages of easy tunability of conductive and optical properties and suitability for the solution processing based on printing and coating technologies.[35,36]

Organic photovoltaic cells are classified into three types: a) dye-sensitized solar cells (DSSC),[26,27,37,38] b) hybrid cells composed of inorganic and organic semiconductors,[28,29,39] and

c) organic thin-film solar cells.[30–33,40] Among them, DSSCs exhibit the highest power conversion efficiency (PCE >10%)[41] although the device stability is still a problem because of the use of liquid electrolytes. On the other hand, in hybrid cells and all solid-state organic cells, the primary issue is the improvement in PCE. Currently, PCE of hybrid cells has remained at 3.8%,[42] but that of organic thin-film photovoltaic cells has been increasing every year and now approaches to 8%.[43] For further improvement in PCE, novel materials with high performance have been extensively developed. As p-type semiconductors, various conjugated polymers have been newly synthesized.[44] In contrast, as n-type semiconductors, fullerene[45,46] and metal oxides such as titanium oxide[47–49] and zinc oxide[50,51] have been exclusively employed in organic photovoltaic cells because they are stable in air compared to organic semiconductors.[44] On the other hand, it is equally important to design and control the device structure precisely because each fundamental process in organic photovoltaic cells occurs on a scale of nanometers. In particular, the thickness of the light-harvesting layer should be comparable to the exciton diffusion length. The fundamental photophysical processes in organic photovoltaic cells are described in detail later.

The device structure of organic photovoltaics based on π-conjugated small molecules can be designed and controlled on a scale of nanometers by the vacuum deposition technique. Forrest and co-workers developed multilayered organic thin-film solar cells precisely designed by the vacuum deposition of π-conjugated small molecules such as phthalocyanine and fullerene.[52–55] They discussed quantitatively the fundamental photophysical processes such as the light absorption and the exciton diffusion on the basis of the multilayered structures.[40] For example, the photon absorption efficiency of each layer in multilayered cells can be quantitatively analyzed using optical simulation with interference effects due to the metal electrode. Therefore, the photon absorption efficiency in the light-harvesting layer can be optimized. Indeed, they demonstrated PCE of 5.7% for a tandem cell with optimized layered structures.[52] In the tandem cell, the front cell is designed to collect the light at longer wavelengths while the back cell is designed to collect the light at shorter wavelengths. This is because the antinodes of standing waves generated in the cells are located further from the reflective metal electrode as the wavelength is increased. On the other hand, the exciton diffusion efficiency can be evaluated quantitatively using one-dimensional diffusion model.[40] Only excitons arriving at a donor/acceptor interface can be dissociated into free carriers that can contribute to the photocurrent generation. In other words, excitons generated far from the interface cannot contribute to the photocurrent generation. In most organic semiconductors, the exciton diffusion length has been reported to be of the order of ~10 nm.[44] Therefore, the thickness of the light-harvesting layer should be designed precisely on a scale of nanometers. As mentioned above, such precise nanostructures can be designed by the vacuum deposition technique. However, it is difficult to fabricate multilayered devices with the nanometer precision by typical solution processes.[35] Furthermore, there are no reports on the analysis of a series of fundamental steps on the basis of layered structures of photovoltaic cells fabricated by the solution process.

Self-assembling is useful not only for designing and fabricating nanostructures by the solution process[56–58] but also for building up macroscopic devices.[59,60] This spontaneous assembling is due to inherent properties of materials in solution, at the liquid–liquid interface, at the air–liquid interface, or on substrates. The assembled materials in solution give various supramolecular nanostructures such as rod,[61] fibers,[62] tubes,[63] and vesicles.[64] Even if such fine and complicated nanostructures are prepared in solution, it is not available for solid devices unless they are immobilized on solid substrates. Langmuir–Blodgett (LB) technique provides highly-ordered self-assembled ultrathin films on substrates.[65–70] In this technique, a condensed monolayer of amphiphilic materials is first prepared on pure water, and then the monolayer floating on the water is transferred onto a solid substrate layer by layer. Thus, the thickness of LB films can be controlled by the number of transferred layers on a scale of nanometers. Self-assembled monolayer (SAM) is one of the most widely used techniques for the modification of solid surfaces.[66,68,71–73] For example, thiol-terminated molecules are employed for fabricating SAM onto gold substrates to obtain highly-oriented monolayer films. Such SAM structures can be immobilized even in pores of porous substrates with a uniform thickness. In this thesis, the layer-by-layer (LbL) deposition technique is employed to fabricate ultrathin films with nanostructures on substrates. The LbL deposition technique is a simple and versatile method with easy operation as described in the next section in detail.[74–77] Therefore, various materials can be introduced as components in nanostructured ultrathin films.[74–77] The thickness can be controlled by the number of deposition cycles on a scale of a few nanometers. This is slightly inferior to the LB technique but precise enough to control the fundamental processes in photovoltaic cells. More importantly, this is the most practical technique for industrial application because it has already been applied to roll-to-roll processes for large-area fabrication.[78,79]

1.2. Layer-by-Layer Deposition Technique

The layer-by-layer (LbL) deposition technique is a simple and versatile method for fabricating ultrathin films.[74–77,80–82] In pioneer work, multicharged polymers were used as polyelectrolytes. Since then, this technique has been applied to various materials such as metals, inorganic particles, dyes, peptides, oligonucleotides, proteins, and enzyme.[83] Furthermore, this technique has been employed to fabricate ultrathin-film-coated materials such as core-shell nanoparticles[77] and two- or three-dimensional patterned structures.[76]

Although various interactions such as charge transfer interaction[84] and hydrophobic interaction[85] are available as the driving force of the LbL deposition, electrostatic interaction is most widely employed. Here, the author explains the general procedure of this technique based on electrostatic interaction. Figure 1–1 shows a schematic illustration of the LbL deposition technique. First, substrates such as glass, quartz, and an indium–tin-oxide (ITO) coated glass are washed in detergent and in various solvents with different polarity by ultrasonication. The surface of these substrates can then be negatively charged by immersion in Piranha solution (70:30 (v/v) H_2SO_4 aq / H_2O_2 aq) or exposure to UV–ozone atmosphere. These treatments not only clean the surface of the substrate but also increase its hydrophilicity. Next, the substrate is immersed in a solution of positively-charged polyelectrolytes. Because of the electrostatic interaction, which is the driving force of the self-assembly,[81] positively-charged polyelectrolytes are deposited on the surface of the substrate. As the surface is covered by positively-charged polyelectrolytes, the surface charge is changed to positive. Consequently, positively-charged polyelectrolytes cannot be deposited on the surface furthermore because of the electric repulsion. In other words, the deposition is spontaneously stopped after the full coverage of polyelectrolytes. Therefore, the thickness of each layer can be regulated and controlled on a scale of a few nanometers because the deposition amount can be tuned by changing deposition conditions such as ionic strength and the charge density on polymer chains. In turn, negatively-charged polyelectrolytes can be deposited on the positively-charged surface. This deposition cycle gives one bilayer of positively-charged polyelectrolytes and negatively-charged polyelectrolytes. Therefore, multilayered ultrathin films can be fabricated by the repetition of alternate immersion in solutions of negatively- and positively-charged polyelectrolytes.

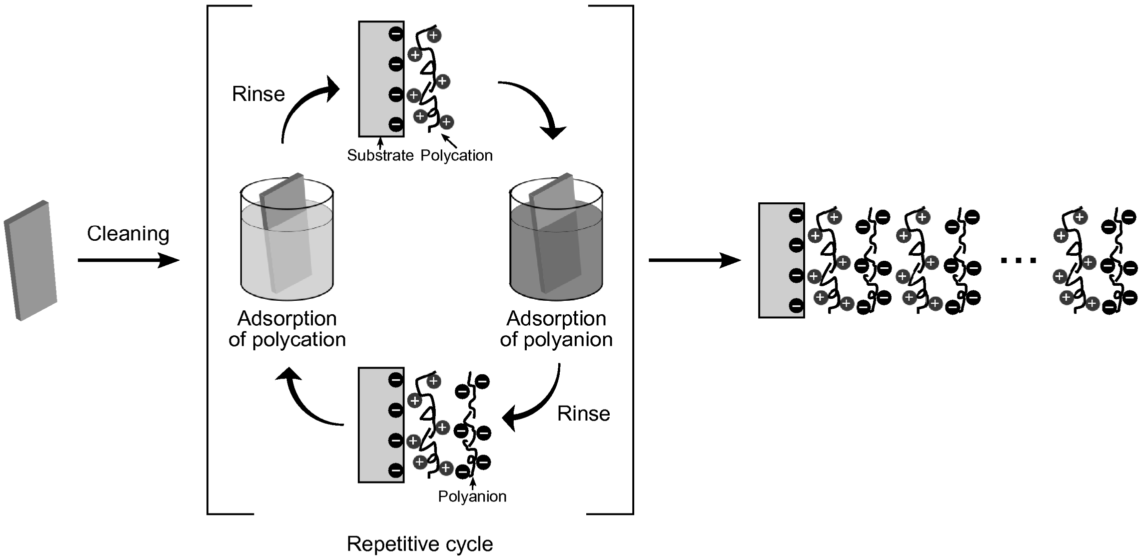

Figure 1–1. Schematic illustration of the layer-by-layer assembly.

Recently, various electronic/optoelectronic ultrathin films have been developed by the LbL deposition technique. As a hole-transporting material, for example, poly(3,4-ethylenedioxythiophene):poly(4-styrenesulfonate) (PEDOT:PSS) can be fabricated by the LbL technique because PEDOT:PSS is a negatively-charged polyelectrolyte. Wakizaka and co-workers demonstrated that PEDOT:PSS-based LbL films exhibit good hole-transporting ability comparable to that of spin-coating films.[86] As a light-harvesting material, poly(*p*-phenylenevinylene) (PPV) can be fabricated by the LbL technique because a precursor of poly(*p*-xylene tetrahydrothiophenium chloride) (pre-PPV) is a positively-charged polyelectrolyte. Mattoussi and co-workers demonstrated the photocurrent response of PPV-based LbL films employed as a light-harvesting layer,[87] which are converted from pre-PPV LbL films by thermal annealing at 230 °C. Ogawa and co-workers improved the optical and conductive properties of PPV-based LbL films by conversion of pre-PPV at a lower temperature of 100 °C.[88] Furthermore, they fabricated multilayered photovoltaic cells with

PPV LbL films as a light-harvesting layer, the layered structure of which were carefully designed and optimized, and demonstrated the best performance with PCE = 0.26% among LbL-based organic solar cells.[89] Other light-harvesting LbL films have also been reported for a polycation attached with a ruthenium derivative in the side chain[90] and copper(II) phthalocyanine-3,4',4'',4'''-tetrasulfonic acid tetrasodium salt.[91] As for an electron-transporting material, there are several reports on LbL films of fullerene[92–95] and carbon nanotube.[96] However, little is known about the conductive properties of such electron-transporting LbL films.

1.3. Organic Photovoltaic Cells

1.3.1. *Photovoltaic Conversion Processes*

The primary photophysical processes in organic thin-film solar cells can be divided into four sequential steps.[40] Figure 1–2 shows typical device structures consisting of three functional layers: a hole-transporting layer, a light-harvesting layer, and an electron-transporting layer. First, photons are absorbed by the light-harvesting layer, followed by exciton generation. Excitons generated in organic materials are tightly-bound electron–hole pairs that cannot be dissociated into free electron and hole at room temperature because of the Coulomb attraction. This is the most obvious difference between organic solar cells and inorganic solar cells: photon absorption in inorganic solar cells directly produces freely mobile charged carriers. The photon absorption efficiency η_A is defined as the ratio of the number of photons absorbed by the active layer to that of incident photons. Second, excitons migrate to a donor/acceptor interface: the interface of the light-harvesting (donor) layer, and the electron-transporting (acceptor) material. Excitons are randomly mobile as electron–hole pairs. Therefore, some of them can reach a donor/acceptor interface but others cannot. The exciton diffusion efficiency η_{ED} is defined as the ratio of the number of excitons arriving at a donor/acceptor interface before deactivating to the ground state to that of excitons generated. Third, excitons arriving at the interface are dissociated into free electron and hole with a driving force of the energy difference in HOMO or LUMO levels between two different materials. The charge transfer efficiency η_{CT} is defined as the ratio of the number of excitons dissociated into free carriers and that of excitons arriving at a donor/acceptor interface. Finally, dissociated electron and hole are collected to each electrode before charge recombination and hence contribute to the photocurrent generation. The charge collection efficiency η_{CC} is defined as the ratio of the number of free charged carriers collected to the electrode and that of free charged carriers generated at a donor/acceptor interface.

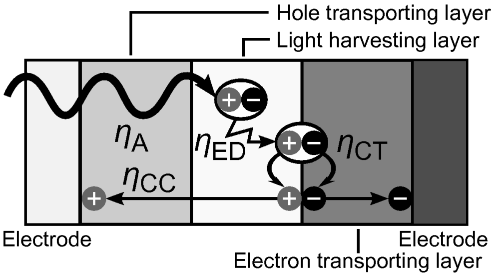

Figure 1–2. The layered structure of typical multilayered photovoltaic cells and the four fundamental steps of photovoltaic conversion processes.

The external quantum efficiency EQE is defined as the ratio of the number of free charged carriers collected to the electrodes to the number of incident photons, which is also called the incident photon-to-current conversion efficiency (IPCE). This efficiency can be directly evaluated by measuring the photocurrent and the intensity of the incident monochromatic light. On the other hand, EQE can also be expressed as the product of each efficiency of four sequential steps.[40]

$$\mathrm{EQE} = \eta_{\mathrm{A}} \times \eta_{\mathrm{ED}} \times \eta_{\mathrm{CT}} \times \eta_{\mathrm{CC}} \tag{1–1}$$

The photon absorption efficiency η_{A} in multilayered structures is quantitatively estimated by optical simulation as described in detail in the next section. The exciton diffusion efficiency η_{ED} is evaluated by the one-dimensional diffusion model, which is described in Chapter 4. The charge transfer efficiency η_{CT} is set to unity for conjugated polymer and fullerene. Indeed, ultrafast charge transfer has been reported for blend films of poly[2-methoxy-5-(3,7-dimethyloctyloxy)-1,4-phenylenevinylene] (MDMO-PPV) and [6,6]-phenyl-C_{61}-butyric acid methyl ester (PCBM).[97] Finally, the charge collection efficiency η_{CC} is calculated using the other parameters η_{A}, η_{ED}, η_{CT}, and EQE.

1.3.2. *Photon Absorption in Multilayered Thin Films*

Photocurrent is as mentioned above directly related to the number of absorbed photons, which is the upper limit of the photocurrent. For thick-film devices the time-averaged energy dissipated by light absorption $Q(x)$ can be simply described as a function of the optical path length x in the device by

$$Q(x) = \alpha I_0 e^{-\alpha x} \tag{1–2}$$

where α is the absorption coefficient and I_0 is the intensity of the incident light. The number of time-averaged absorbed photons is the product of $Q(x)$ and λ/hc where λ is the wavelength of the incident light, h is the Planck's constant, and c is the speed of light, respectively. For thin-film devices where x is comparable to λ, however, interference effects should be included in the calculation. In this section, the authors explains how to evaluate the number of absorbed photons in multilayered photovoltaic cells on the basis of the optical transfer-matrix theory described by Heavens,[98] previously applied to organic photovoltaic cells by Pettersson *et al.*,[99] and Yang *et al.*[100].

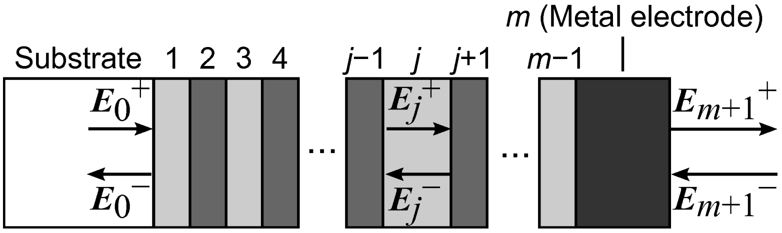

Figure 1–3. Illustrations of optical simulation in a general multilayered structure having *m* layers (including metal electrode). The optical electric field of waves propagating in the positive *x* direction and negative *x* direction are denoted as $\boldsymbol{E}^+$ and $\boldsymbol{E}^-$, respectively.

This model includes several assumptions as follows: 1) each layer is considered as homogeneous and isotropic and therefore its refractive index is considered to be a scalar complex, 2) all interfaces between layers are parallel and flat compared to the wavelength of the incident light, 3) the incident light can be described to a plane wave. Figure 1–3 shows the geometry of the multilayer stack employed in the optical electric field calculation. The time-averaged absorbed power of layer *j*, $Q_j(x)$, as a function of position *x* is given by

$$Q_j(x) = \frac{1}{2} c \varepsilon_0 \alpha_j n_j \left| \boldsymbol{E}_j(x) \right|^2 \qquad (1\text{–}3)$$

where ε_0 is the permittivity of free space and α_j is the absorption coefficient of layer *j*, $\boldsymbol{E}_j(x)$ is the optical electric field amplitude in layer *j*. Note that α_j is related to the extinction coefficient of layer *j*, k_j, as follows: $\alpha_j = 4\pi k_j/\lambda$. The number of time-averaged absorbed photons is obtained to be the product of $Q_j(x)$ and λ/hc. As a result, the efficiency of absorption of photons η_A is calculated by the ratio of the number of time-averaged absorbed photons to the number of the time-averaged incident photons.

Expanding eq. 1–3, another expression of $Q_j(x)$ is given by[99]

$$Q_j(x) = \alpha_j T_j I_0 \left[e^{-\alpha_j x} + \rho_j^{+2} e^{-\alpha_j (2d_j - x)} + 2\rho_j^+ e^{-\alpha_j d_j} \cdot \cos\left(\frac{4\pi n_j}{\lambda}(d_j - x) + \delta_j^+ \right) \right] \qquad (1\text{–}4)$$

where $T_j = (n_j/n_0)|t_j^+|^2$ is the internal intensity transmittance, and ρ_j^+ and δ_j^+ are the absolute value and the argument of the complex reflection coefficient for the positive-directing partial system. As seen in eq. 1–4, $Q_j(x)$ is described by three terms. The first term originates from the optical electric field propagating in the positive x direction. The second term originates from the optical electric field propagating in the negative x direction. The third term is due to interference of two waves. From the equation, photovoltaic cells, which have the highly reflected interface such as metal electrode, have a large impact on optical interference. In other words, optical interference effect should be considered in most photovoltaic cells of the multilayered thin film.

1.4. Outline of This Thesis

This thesis consists of six chapters. The first chapter describes the background and the motivation of this thesis. The following chapters are divided into two parts.

In Part I (Chapters 2–3), electron-transporting LbL films are described. In Chapter 2, ultrathin films of water-soluble fullerene derivatives are fabricated by the LbL deposition technique. The author discusses the deposition mechanism and characterizes the conductive properties of these films. Conductivity and electron mobility of the fullerene LbL films suggests that the fullerene films can serve as an efficient electron-transporting layer in well-defined nanostructures of LbL films. In Chapter 3, ultrathin films of titanium oxide are described. These films are obtained by thermal-conversion of the precursor film fabricated by the LbL deposition technique. The author characterizes conductive properties of those films, and applies as an electron-transporting layer in organic photovoltaic cells. Both of conductivity and electron mobility of the titanium oxide LbL film are as high as that of the titanium oxide semiconductor film. Furthermore, the author demonstrates that the LbL film can serve as an electron-transporting layer in organic photovoltaic cells.

In Part II (Chapters 4–6), poly(*p*-phenylenevinylene) (PPV) LbL films as a light harvesting layer are described. In Chapter 4, the correlation between internal nanostructures and the photovoltaic conversion process in multilayered solar cells based on PPV LbL films is described. The photon absorption efficiency η_{A} is evaluated using optical simulation. The exciton diffusion efficiency η_{ED} is estimated using a one-dimensional diffusion model from the photoluminescence measurement. From these results, the device performance is quantitatively analyzed on the basis of the device structure. In Chapter 5, the improvement in the light-harvesting efficiency of LbL films composed of PPV and a PPV derivative is discussed. Both absorption and emission of the PPV derivative in water/dimethylsulfoxide mixed solution are enhanced compared to that in water, suggesting that PPV derivative chains are likely to be expanded more in the mixed solvent. The improvement in the light-harvesting efficiency of PPV-based LbL films prepared in the mixed solution compared to that of the reference cell is demonstrated. In Chapter 6, interface effects of PPV LbL films in hybrid cells of an LbL film and a blend film are discussed. The author demonstrates the improvement in device performance as a result of the improvement in the light-harvesting efficiency and the suppression of charge recombination by PPV LbL films.

References

(1) Pope, M.; Swenberg, C. E. *Electronic Processes in Organic Crystals and Polymers*, 2nd ed.; Oxford University Press; New York, 1999; pp 581–645.

(2) MacDiarmid, A. G. *Angew. Chem. Int. Ed.* **2001**, *40*, 2581–2590.

(3) Ganin, A. Y.; Takabayashi, Y.; Khimyak, Y. Z.; Margadonna, S.; Tamai, A.; Rosseinsky, M. J.; Prassides, K. *Nat. Mater.* **2008**, *7*, 367–371.

(4) Mitsuhashi, R.; Suzuki, Y.; Yamanari, Y.; Mitamura, H.; Kambe, T.; Ikeda, N.; Okamoto, H.; Fujiwara, A.; Yamaji, M.; Kawasaki, N.; Maniwa, Y.; Kubozono, Y. *Nature* **2010**, *464*, 76–79.

(5) Shinagawa, J.; Kurosaki, Y.; Zhang, F.; Parker, C.; Brown, S. E.; Jérome, D.; Christensen, J. B.; Bechgaard, K. *Phys. Rev. Lett.* **2007**, *98*, 147002.

(6) Greene, R. L.; Street, G. B.; Sulter, L. J. *Phys. Rev. Lett.* **1975**, *34*, 577–579.

(7) Shirakawa, H.; Louis, E. J.; MacDiarmid, A. G.; Chiang, C. K.; Heeger, A. J. *J. Chem. Soc., Chem. Commun.* **1977**, 578–580.

(8) Ito, T.; Shirakawa, H.; Ikeda, S. *J. Polym. Sci., Part A: Polym. Chem.* **1974**, *12*, 11–20.

(9) Akagi, K.; Katayama, S.; Shirakawa, H. *Synth. Met.* **1987**, *17*, 241–246.

(10) Kroto, H. W.; Heath, J. R.; O'Brien, S. C.; Curl, R. F.; Smalley, R. E. *Nature* **1985**, *318*, 162–163.

(11) Ajie, H.; Alvarez, M. M.; Anz, S. J.; Beck, R. D.; Diederich, F.; Fostiropoulos, K.; Huffman, D. R.; Krätschmer, W.; Rubin, Y.; Schriver, K. E.; Sensharma, D.; Whetten, R. L. *J. Phys. Chem.* **1990**, *94*, 8630–8633.

(12) Haddon, R. C.; Hebard, A. F.; Rosseinsky, M. J.; Murphy, D. W.; Duclos, S. J.; Lyons, K. B.; Miller, B.; Rosamilia, J. M.; Fleming, R. M.; Kortan, A. R.; Glarum, S. H.;

Makhija, A. V.; Muller, A. J.; Eick, R. H.; Zahurak, S. M.; Tycko, R.; Dabbagh, G.; Thiel, F.A. *Nature* **1991**, *350*, 320–322.

(13) Gierschner, J.; Cornil, J.; Egelhaaf, H.-J. *Adv. Mater.* **2007**, *19*, 173–191.

(14) Haddon, R. C. *Acc. Chem. Res.* **1988**, *21*, 243–249.

(15) Kamtekar, K. T.; Monkman, A. P.; Bryce, M. R. *Adv. Mater.* **2010**, *22*, 572–582.

(16) Laquai, F.; Park, Y.-S.; Kim, J.-J.; Basché, T. *Macromol. Rapid Commun.* **2009**, *30*, 1203–1231.

(17) So, F.; Kido, J.; Burrows, P. *MRS Bull.* **2008**, *33*, 663–669.

(18) Kalinowski, J. *Opt. Mater.* **2008**, *30*, 792–799.

(19) Małachowski, M. J.; Żmija, J. *Opto-Electron. Rev.* **2010**, *18*, 121–136.

(20) Smith, J.; Hamilton, R.; McCulloch, I.; Stingelin-Stutzmann, N.; Heeney, M.; Bradley, D. D. C.; Anthopoulos, T. D. *J. Mater. Chem.* **2010**, *20*, 2562–2574.

(21) Wen, Y.; Liu, Y. *Adv. Mater.* **2010**, *22*, 1331–1345.

(22) Katz, H. E.; Huang, J. *Annu. Rev. Mater. Res.* **2009**, *39*, 71–92.

(23) Sirringhaus, H. *Proc. IEEE* **2009**, *97*, 1570–1579.

(24) Naber, R. C. G.; Asadi, K.; Blom, P. W. M.; de Leeuw, D. M.; de Boer, B. *Adv. Mater.* **2010**, *22*, 933–945.

(25) Burr, G. W.; Kurdi, B. N.; Scott, J. C.; Lam, C. H.; Gopalakrishnan, K.; Shenoy, R. S. *IBM J. Res. Dev.* **2008**, *52*, 449–464.

(26) Grätzel, M. *Acc. Chem. Res.* **2009**, *42*, 1788–1798.

(27) de Freitas, J. N.; Nogueira, A. F.; De Paoli, M.-A. *J. Mater. Chem.* **2009**, *19*, 5279–5294.

(28) Ong, P.-L.; Levitsky, I. A. *Energies* **2010**, *3*, 313–334.

(29) Günes, S.; Sariciftci, N. S. *Inorg. Chim. Acta* **2008**, *361*, 581–588.

(30) Chen, L.-M.; Xu, Z.; Hong, Z.; Yang, Y. *J. Mater. Chem.* **2010**, *20*, 2575–2598.

(31) Heremans, P.; Cheyns, D.; Rand, B. P. *Acc. Chem. Res.* **2009**, *42*, 1740–1747.

(32) Kippelen, B.; Brédas, J.-L. *Energy Environ. Sci.* **2009**, *2*, 251–261.

(33) Dennler, G.; Scharber, M. C.; Brabec, C. J. *Adv. Mater.* **2009**, *21*, 1323–1338.

(34) Calvert, P. *Chem. Mater.* **2001**, *13*, 3299–3305.

(35) Krebs, F. C. *Sol. Energy Mater. Sol. Cells* **2009**, *93*, 394–412.

(36) Brabec, C. J.; Durrant, J. R. *MRS Bull.* **2008**, *33*, 670–675.

(37) Gonçalves, L. M.; de Zea Bermudez, V.; Ribeiro, H. A.; Mendes, A. M. *Energy Environ. Sci.* **2008**, *1*, 655–667.

(38) O'Regan, B.; Grätzel, M. *Nature* **1991**, *353*, 737–740.

(39) Bouclé, J.; Ravirajan, P.; Nelson, J. *J. Mater. Chem.* **2007**, *17*, 3141–3153.

(40) Peumans, P.; Yakimov, A.; Forrest, S. R. *J. Appl. Phys.* **2003**, *93*, 3693–3723.

(41) Grätzel, M. In *The Advent of Mesoscopic Solar Cells*, International Symposium on Innovative Solar Cells 2009, Tokyo, Japan, 2009.

(42) Mor, G. K.; Kim, S.; Paulose, M.; Varghese, O. K.; Shankar, K.; Basham, J.; Grimes, C. A. *Nano Lett.* **2009**, *9*, 4250–4257.

(43) Solarmer Energy, Inc. Homepage. http://www.solarmer.com/ (accessed May 5, 2010).

(44) Brabec, C. J. *et al. Organic Photovoltaics*; Brabec, C. J.; Dyakonov, V.; Scherf, U., Eds.; Wiley-VCH Verlag GmbH & Co. KGaA; Weinheim, 2008; pp 3–210.

(45) Liang, Y.; Xu, Z.; Xia, J.; Tsai, S.-T.; Wu, Y.; Li, G.; Ray, C.; Yu, L. *Adv. Mater.* in press: DOI: 10.1002/adma.200903528.

(46) Park, S. H.; Roy, A.; Beaupré, S.; Cho, S.; Coates, N.; Moon, J. S.; Moses, D.; Leclerc, M.; Lee, K.; Heeger, A. J. *Nat. Photonics* **2009**, *3*, 297–303.

(47) Snaith, H. J.; Moule, A. J.; Klein, C.; Meerholz, K.; Friend, R. H.; Grätzel, M. *Nano*

Lett. **2007**, *7*, 3372–3376.

(48) Bouclé, J.; Chyla, S.; Shaffer, M. S. P.; Durrant, J. R.; Bradley, D. D. C.; Nelson, J. *Adv. Funct. Mater*. **2008**, *18*, 622–633.

(49) Mikroyannidis, J. A.; Stylianakis, M. M.; Suresh, P.; Sharma, G. D. *Sol. Energy Mater. Sol. Cells* **2009**, *93*, 1792–1800.

(50) Huang, J.-S.; Chou, C.-Y.; Lin, C.-F. *Sol. Energy Mater. Sol. Cells* **2010**, *94*, 182–186.

(51) Oosterhout, S. D.; Wienk, M. M.; van Bavel, S. S.; Thiedmann, R.; Koster, L. J. A.; Gilot, J.; Loos, J.; Schmidt, V.; Janssen, R. A. J. *Nat. Mater*. **2009**, *8*, 818–824.

(52) Xue, J.; Uchida, S.; Rand, B. P.; Forrest, S. R. *Appl. Phys. Lett*. **2004**, *85*, 5757–5759.

(53) Xue, J.; Rand, B. P.; Uchida, S.; Forrest, S. R. *Adv. Mater*. **2005**, *17*, 66–71.

(54) Perez, M. D.; Borek, C.; Forrest, S. R.; Thompson, M. E. *J. Am. Chem. Soc*. **2009**, *131*, 9281–9286.

(55) Tong, X.; Lassiter, B. E.; Forrest, S. R. *Org. Electron*. **2010**, *11*, 705–709.

(56) Ariga, K.; Hu, X.; Mandal, S.; Hill, J. P. *Nanoscale* **2010**, *2*, 198–214.

(57) Mao, Z.; Xu, H.; Wang, D. *Adv. Funct. Mater*. **2010**, *20*, 1053–1074.

(58) Ling, X. Y.; Reinhoudt, D. N.; Huskens, J. *Pure Appl. Chem*. **2009**, *81*, 2225–2233.

(59) Yan, Y.; Huang, J. *Coord. Chem. Rev*. **2010**, *254*, 1072–1080.

(60) Matsushita, Y.; Takano, A.; Hayashida, K.; Asari, T.; Noro, A. *Polymer* **2009**, *50*, 2191–2203.

(61) Palmer, L. C.; Stupp, S. I. *Acc. Chem. Res*. **2008**, *41*, 1674–1684.

(62) Zhao, Y.; Fan, Y.; Mu, X.; Gao, H.; Wang, J.; Zhang, J.; Yang, W.; Chi, L.; Wang, Y. *Nano Res*. **2009**, *2*, 493–499.

(63) Lee, H. Y.; Nam, S. R.; Hong, J.-I. *Chem. Asian J*. **2009**, *4*, 226–235.

(64) Anraku, Y.; Kishimura, A.; Oba, M.; Yamasaki, Y.; Kataoka, K. *J. Am. Chem. Soc.* **2010**, *132*, 1631–1636.

(65) Langmuir, I; Blodgett, K. B. *Kolloid Z.* **1935**, *73*, 257–263.

(66) Ariga, K.; Hill, J. P.; Lee, M. V.; Vinu, A.; Charvet, R.; Acharya, S. *Sci. Technol. Adv. Mater.* **2008**, *9*, 014109.

(67) Giancane, G.; Bettini, S.; Valli, L. *Colloids Surf., A* **2010**, *354*, 81–90.

(68) Ujihara, M.; Imae, T. *Polym. Int.* **2010**, *59*, 137–144.

(69) Acharya, S.; Hill, J. P.; Ariga, K. *Adv. Mater.* **2009**, *21*, 2959–2981.

(70) Chatterji, D.; Rajdev, P. *Curr. Sci.* **2008**, *95*, 1226–1236.

(71) Miozzo, L.; Yassar, A.; Horowitz, G. *J. Mater. Chem.* **2010**, *20*, 2513–2538.

(72) Vilar, M. R.; do Rego, A. M. B. *J. Electron. Spectrosc. Relat. Phenom.* **2009**, *172*, 27–35.

(73) Zacher, D.; Shekhah, O.; Wöll, C.; Fischer, R. A. *Chem. Soc. Rev.* **2009**, *38*, 1418–1429.

(74) Decher, G. *Science* **1997**, *277*, 1232–1237.

(75) Ariga, K.; Hill, J. P.; Ji, Q. *Phys. Chem. Chem. Phys.* **2007**, *9*, 2319–2340.

(76) Hammond, P. T. *Adv. Mater.* **2004**, *16*, 1271–1293.

(77) Caruso, F. *Adv. Mater.* **2001**, *13*, 11–22.

(78) Fujita, S.; Fujimoto, K.; Naka, T.; Shiratori, S. *IEICE Trans. Electron.* **2004**, *E87–C*, 2064–2070.

(79) Fujimoto, K.; Fujita, S.; Ding, B.; Shiratori, S. *Jpn. J. Appl. Phys.* **2005**, *44*, L126–L128.

(80) Decher, G,; Hong, J. D. *Makromol. Chem. Macromol. Symp.* **1991**, *46*, 321–327.

(81) Decher, G.; Hong, J. D.; Schmitt, J. *Thin Solid Films* **1992**, *210/211*, 831–835.

(82) Bertrand, P.; Jonas, A.; Laschewsky, A.; Legras, R. *Macromol. Rapid Commun.* **2000**, *21*, 319–348.

(83) *Multilayer Thin Films*; Decher, G.; Schlennoff, J., Eds.; Wiley-VCH Verlag GmbH & Co. KGaA; Weinheim, 2003.

(84) Shimazaki, Y.; Mitsuishi, M.; Ito, S.; Yamamoto, M. *Langmuir* **1997**, *13*, 1385–1387.

(85) Shimazaki, Y.; Mitsuishi, M.; Ito, S.; Yamamoto, M.; Inaki, Y. *Thin Solid Films* **1998**, *333*, 5–8.

(86) Wakizaka, D.; Fushimi, T.; Ohkita, H.; Ito, S. *Polymer* **2004**, *45*, 8561–8565.

(87) Mattoussi, H.; Rubner, M. F.; Zhou, F.; Kumar, J.; Tripathy, S. K.; Chiang, L. Y. *Appl. Phys. Lett.* **2000**, *77*, 1540–1542.

(88) Ogawa, M.; Kudo, N.; Ohkita, H.; Ito S.; Benten, H. *Appl. Phys. Lett.* **2007**, *90*, 223107.

(89) Benten, H.; Ogawa, M.; Ohkita, H.; Ito, S. *Adv. Funct. Mater.* **2008**, *18*, 1563–1572.

(90) Fushimi, T.; Oda, A.; Ohikita, H.; Ito, S. *Langmuir* **2005**, *21*, 1584–1589.

(91) Benten, H.; Kudo, N.; Ohkita, H.; Ito, S. *Thin Solid Films* **2009**, *517*, 2016–2022.

(92) Liu, Y.; Wang, Y.; Lu, H.; Claus, R. O. *J. Phys. Chem. B* **1999**, *103*, 2035–2036.

(93) Rosenlehner, K.; Schunk, T.; Jux, N.; Brettreich, M.; Hirsch, A. *Org. Biomol. Chem.* **2008**, *6*, 2697–2705.

(94) Guldi, D. M.; Zilbermann, I.; Anderson, G.; Kotov, N. A.; Tagmatarchis, N.; Prato, M. *J. Mater. Chem.* **2005**, *15*, 114–118.

(95) Mwaura, J. K.; Pinto, M. R.; Witker, D.; Ananthakrishnan, N.; Schanze, K. S.; Reynolds, J. R. *Langmuir* **2005**, *21*, 10119–10126.

(96) Lee, S. W.; Kim, B.-S.; Chen, S.; Shao-Horn, Y.; Hammond, P. T. *J. Am. Chem. Soc.* **2009**, *131*, 671–679.

(97) Brabec, C. J.; Zerza, G.; Cerullo, G.; Silvestri, S. D.; Luzzati, S.; Hummelen, J. C.; Sariciftci, S. *Chem. Phys. Lett.* **2001**, *340*, 232–236.

(98) Heavens, O. S. *Optical Properties of Thin Solid Films*; Dover; New York, 1965.

(99) Pettersson, L. A. A.; Roman, L. S.; Inganäs, O. *J. Appl. Phys.* **1999**, *86*, 487–496.

(100) Sievers, D. W.; Shrotriya, V.; Yang, Y. *J. Appl. Phys.* **2006**, *100*, 114509.

Part I

Chapter 2

Fabrication and Conductive Properties of Multilayered Ultrathin Films Designed by Layer-by-Layer Assembly of Water-Soluble Fullerenes

2.1. Introduction

Fullerenes and their derivatives have attracted extensive attention as a promising material in organic electronic devices owing to the prominent electron-accepting ability and the high electron mobility.[1–4] Fullerenes are inherently insoluble in aqueous solutions because of their extremely hydrophobic nature, but can be made amphiphilic and hence soluble by incorporating appropriate functional groups such as ionic units. Fullerene amphiphilic derivatives have drawn increasing attention because of their self-assembling property to form various supramolecular nanostructures.[5–7] For example, cationic fullerenes such as fulleropyrrolidiniums have been reported to self-assemble into nanorods,[8,9] vesicles,[8,10] and spheres.[9] Some anionic fullerenes also form stable large bilayered vesicles similar to those of chain-based surfactants and lipids.[11,12] From the detailed structural analysis, the potassium salt of a pentaphenyl fullerene derivative was found to spontaneously associate into bilayers and to form spherical vesicles with an average hydrodynamic radius of ~17 nm. Furthermore, fullerene derivatives with long alkyl chains yield hierarchically-ordered supramolecular assemblies such as vesicles, fibers, disks, and cones.[13] The self-assembling properties of fullerene derivatives play a vital role not only in fullerene-based nanoscience but also in application to organic electronic devices.

The layer-by-layer (LbL) deposition technique is a simple and versatile method for fabricating ultrathin films,[14] and therefore applicable to fabricate various types of ultrathin-films coated on applied materials.[15–17] Water-soluble fullerene derivatives also can be electrostatically self-assembled into multilayered films in an LbL fashion. Claus and co-workers have reported self-assembly of micrometer-thick LbL films of fullerene with excellent homogeneity.[18] Since the first report of the preparation of uniform fullerene films through solution chemistry, fullerene LbL films have been developed with various water-soluble fullerenes such as fullerols,[19] sulfonated derivatives,[20–22] carboxylated derivative,[23] and amine-attached derivatives.[21,24–26] Furthermore, photovoltaic devices have been reported for a combination of water-soluble fullerenes and conjugated polymers.[19–21,24,25] Schanze, Reynolds, and co-workers reported photovoltaic cells based on LbL thin films of poly(*p*-phenylene ethynylene)-based anionic conjugated polyelectrolytes and water-soluble cationic fullerene derivatives.[24] The LbL-based solar cells exhibited a short-circuit current of 0.5 mA cm^{-2} and a power conversion efficiency of 0.04% at AM1.5 solar conditions, suggesting that water-soluble fullerene can serve as an electron-transporting material in the devices. However, the deposition mechanism and the conductive properties of such fullerene-based LbL films are not fully understood.

In this chapter, the author fabricates ultrathin films of water-soluble fullerene derivatives by the LbL deposition technique and discuss the deposition mechanism and the conductive properties of those films. Although there are several reports on the fabrication of LbL films of water-soluble fullerenes, the deposition mechanism has not been discussed on the basis of various self-assembled states of water-soluble fullerenes in aqueous solutions. In most cases, the linear growth of the film thickness is employed as a simple criterion for the LbL deposition. Furthermore, there are no reports on the conductivity and the electron mobility of fullerene-based LbL films, which are fundamental properties for developing organic electronic devices. Herein the author employs two water-soluble fullerenes to fabricate ultrathin LbL films. The dispersion state of the fullerenes in aqueous solutions is analyzed by the dynamic light scattering measurement, upon which the deposition mechanism of the LbL films is discussed. Furthermore, the conductivity and the electron mobility of the fullerene LbL films evaluated quantitatively suggest that the fullerene films can serve as an efficient electron-transporting layer in well-defined nanostructure of LbL films.

2.2. Experimental Section

2.2.1. *Materials*

Two kinds of water-soluble fullerene derivatives were synthesized as reported previously:[27–29] one is an anionic fullerene with dicarboxylic groups $C_{61}(COO^-)_2$ (FDCA) and the other is a cationic fullerene with a quaternized amine group $C_{60}C_2H_4N(CH_3)_2^+$ (FMAC). For the LbL deposition, water was purified by deionization, distillation, and passing through a filtration system (Barnstead Nanopure II). The anionic fullerene was dissolved at 2 mM with water and the cationic fullerene was dissolved at 0.5 mM with a mixed solvent of water and dimethylsulfoxide (DMSO) (3:1 by volume). An aqueous solution of poly(3,4-ethylenedioxythiophene):poly(4-styrenesulfonate) (PEDOT:PSS; Aldrich, 1.3 wt% dispersion in water, conductive grade) was diluted to 10 mM with water. Poly(sodium 4-styrenesulfonate) (PSS; Aldrich, M_w = 70,000 g mol^{-1}) was dissolved at 10 mM with water. An aqueous solution of poly(diallyldimethylammonium chloride) (PDDA; Aldrich, 20 wt% in water, M_w = 100,000–200,000 g mol^{-1}) was diluted to 10 mM with water. These solutions were employed as polyelectrolyte solutions for the LbL deposition. Polystyrene (PS; Aldrich, M_w = 280,000 g mol^{-1}) was purified by reprecipitation from a toluene solution into methanol three times. A blend solution of PS and C_{60} (Frontier Carbon Co Ltd.) in *o*-dichlorobenzene (Aldrich) was used for the fabrication of C_{60}-dispersed PS films by spincoating. The volume fraction of C_{60} in the blend film was varied from 24 to 72 vol% (from 33 to 80 wt% as the weight fraction). Figure 2–1 shows the chemical structures of materials employed in this chapter.

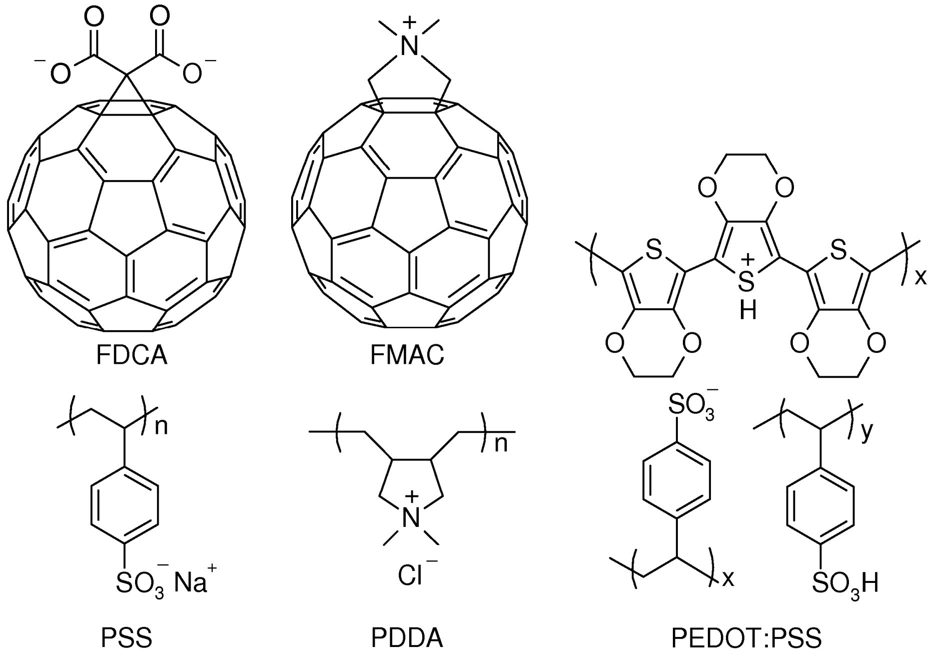

Figure 2–1. Chemical structures of water-soluble anionic fullerene (FDCA) and cationic fullerene (FMAC) and polyelectrolytes employed in this chapter.

2.2.2. *Fabrication of LbL Films*

For UV–visible absorption and sheet-resistance measurements, quartz substrates were employed for the LbL deposition. These substrates were cleaned by ultrasonication in toluene, acetone, and ethanol for 15 min each, then dried with a N_2 flow, and further treated with a UV–O_3 cleaner for 1 h. For the fabrication of the anionic fullerene LbL films, the substrates were immersed in the cationic solution of PDDA for 5 min, and rinsed in water for 3 min. Subsequently, they were immersed in the anionic solution of FDCA for 5 min, and rinsed in water for 3 min. This cycle gives one bilayer of PDDA/FDCA. The anionic fullerene LbL films with *n* bilayers of PDDA and FDCA are abbreviated as $(\mathrm{PDDA/FDCA})_n$. For the fabrication of the cationic fullerene films, 4 bilayers of PDDA and PSS were prepared as a precoating film on the quartz substrate. The precoated substrates were immersed in the cationic solution of FMAC for 5 min, and rinsed in water for 3 min. Subsequently, they were immersed in the anionic solution of PSS for 5 min, and rinsed in water for 3 min. The cationic fullerene LbL films with (n + 0.5) bilayers of FMAC and PSS are abbreviated as $(\mathrm{FMAC/PSS})_n/\mathrm{FMAC}$. Note that LbL films were completely dried under a flow of air for 4–6 min after each immersion and rinse except for the deposition of FMAC. For *J*–*V* characteristics measurements, indium–tin-oxide (ITO)-coated glass substrates (10 Ω square^{-1}) were employed for the LbL deposition. The substrates were cleaned as described above. First, a buffer layer was prepared by the LbL deposition of PEDOT:PSS and PDDA as reported previously.[30] The thickness was 100 nm. Second, anionic or cationic fullerene LbL films were fabricated on the buffer layer. Finally, LiF and Al were thermally deposited at 2.5×10^{-6} Torr on top of the LbL film. Each electrode thickness was <1 nm for LiF and 50 nm for Al. The layered structure is abbreviated as $\mathrm{ITO|PEDOT{:}PSS|(PDDA/FDCA)}_n\mathrm{|LiF|Al}$ or $\mathrm{ITO|PEDOT{:}PSS|(FMAC/PSS)}_n\mathrm{/FMAC|LiF|Al}$. As a control, C_{60}:PS blend films were also prepared by spincoating from the blend solution of PS and C_{60} for the sheet-resistance and the *J*–*V* characteristics measurements.

2.2.3. *Measurements*

The particle size and zeta potential of fullerene clusters dispersed in solution were evaluated by dynamic light scattering measurement (Otsuka Electronics, ELS-Z2). Before the measurements, the fullerene-dispersed solutions were ultrasonicated, followed by filtering through a 0.45-μm syringe filter. The distribution of the particle size was calculated using the algorithm of Marquardt. The UV–visible absorption and fluorescence spectra of fullerene-dispersed solutions and anionic or cationic fullerene LbL films were measured with a spectrophotometer (Hitachi, U-3500) and a fluorescence spectrophotometer (Hitachi, F-4500), respectively. The film thickness and surface morphology of anionic or cationic fullerene LbL film were measured with an atomic force microscope (AFM; Shimadzu, SPM-9500J) in contact mode. The surface resistivity ρ_s of anionic or cationic fullerene LbL films and C_{60}:PS blend films was measured with a ring probe (Mitsubishi Chemical Analytech, UR-SS) connected to a digital electrometer (Advantest, R8252). In this measurement, the sample resistance is typically so high that the contact resistance between the electrodes and the sample is negligible. The *J*–*V* characteristics of the films were measured with a DC voltage current source/monitor (Advantest, R6243). The electron mobility μ_e was evaluated from the space charge limited current (SCLC), which is described by

$$J = \frac{9}{8}\varepsilon_0\varepsilon_r\mu_e\frac{(V - V_{BI} - V_{RS})^2}{d^3} \qquad (2–1)$$

where ε_0 is the permittivity of free space and ε_r is the relative dielectric constant. The effective ε_r of multicomponent films was estimated as the volume average of each component: $\varepsilon_r(C_{60}) = 4.4$,[31] $\varepsilon_r(\text{PDDA}) = 1.8$,[32] $\varepsilon_r(\text{PS}) = 2.6$,[32] and $\varepsilon_r(\text{PSS}) = 2.3$.[33,34] The value of V_{RS} is the voltage drop due to the series resistance r_s, where V_{RS} was obtained as the product of r_s

and the device area. The built-in-voltage V_{BI} and r_s were treated as fitting parameters.[35] All measurements were performed in air at room temperature.

2.3. Results and Discussion

2.3.1. *Fullerene Dispersion in Aqueous Solution*

For the successive LbL deposition, materials should have at least two charged groups and hence polyelectrolytes are most preferable to a component of LbL films. However, water-soluble fullerenes employed in this chapter have only one or two ionic groups in one side of the molecule: FDCA has two carboxyl anion groups and FMAC has only one amino cation group. In other words, if these water-soluble fullerenes were molecularly dispersed in aqueous solutions, the successive LbL deposition would be impossible. As shown in Figure 2–2, no characteristic absorption peak but just a broad absorption tail was observed for both FDCA and FMAC solutions. These broad absorption spectra are ascribed to the formation of fullerene aggregates.[36,37] Interestingly, some amphiphilic fullerene derivatives have been reported to form bilayer vesicles in aqueous solutions.[8,11] To clarify the dispersion state of the water-soluble fullerenes in aqueous solutions, the author measured the dynamic light scattering of the solution. As shown in Figure 2–3, both materials exhibited bimodal peaks in the distribution of the particle size: a major peak at ~20 nm and a minor peak at ~70 nm were observed for FDCA, and a minor peak at ~60 nm and a major peak at ~180 nm were observed for FMAC. A previous TEM study reported that FMAC in aqueous solutions forms vesicles with a diameter of 10–70 nm and a shell thickness of 3–6 nm.[8] The author therefore ascribes the minor peak to FMAC vesicles and the major peak to aggregates of FMAC vesicles. The same could be said for FDCA. Indeed, pentaphenyl anionic fullerenes have been reported to form stable spherical bilayer vesicles in water.[11] On the other hand, the zeta potential was found to be −28 mV for FDCA and +27 mV for FMAC, which are indicative of stable dispersion as polyanion and polycation, respectively,[38] because of the electric repulsion. In other words, both water-soluble fullerenes are considered to be dispersed as stable polyelectolytes in the aqueous solutions, which are preferable to the LbL deposition.

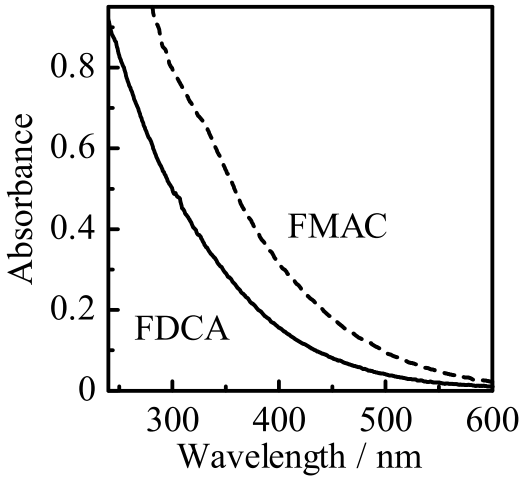

Figure 2–2. Absorption spectra of FDCA in water (solid line) and FMAC in a mixed solvent of water and DMSO (3/1 by volume) (broken line). The concentration of water-soluble fullerenes was 2.0×10^{-5} M.

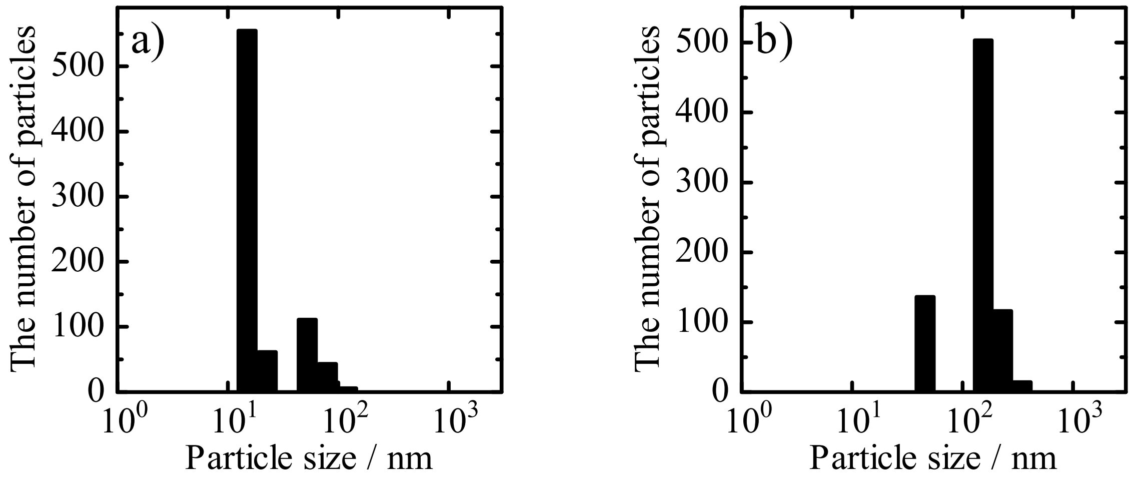

Figure 2–3. Apparent distribution of the particle size: a) FDCA and b) FMAC in the aqueous solutions.

2.3.2. *Fabrication of Fullerene LbL Films*

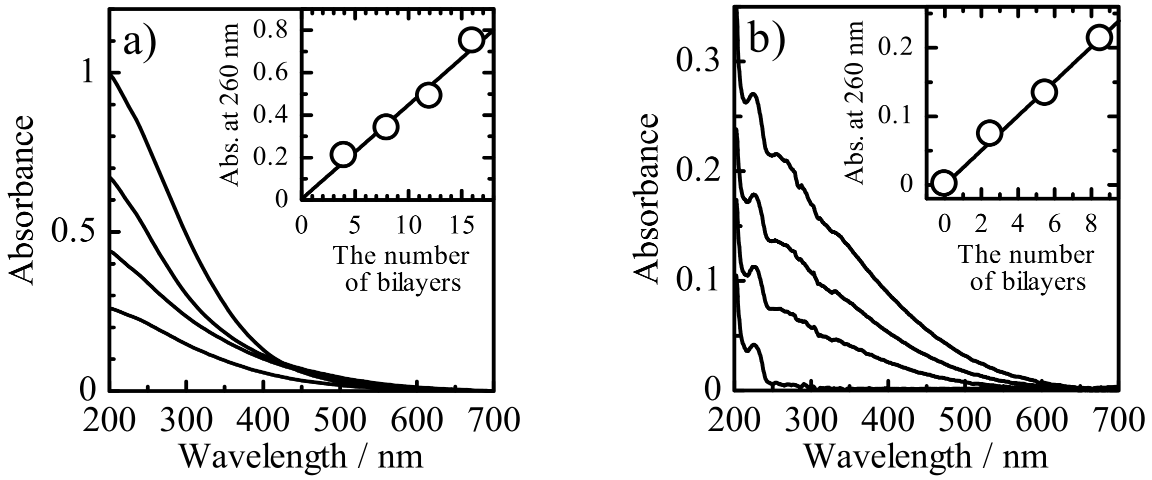

Figure 2–4. Absorption spectra of fullerene LbL films on quartz substrates: a) PDDA/FDCA (4, 8, 12, 16 bilayers) and b) FMAC/PSS (0, 2.5, 5.5, 8.5 bilayers) where the spectrum of 0 bilayers is due to a precursor film of $(PDDA/PSS)_4$. The insets show plots of the absorbance at 260 nm against the number of bilayers.

Figure 2–4a shows absorption spectra of anionic fullerene LbL films on quartz substrates. The absorption increased with an increase in the number of bilayers of PDDA/FDCA. This broad absorption is ascribed to FDCA because PDDA has no absorption in this wavelength range. On the other hand, Figure 2–4b shows absorption spectra of cationic fullerene LbL films on quartz substrates. The absorption also increased with an increase in the number of bilayers of FMAC/PSS. Note that the absorption spectrum of 0 bilayers is ascribed to PSS in the precoating film of $(PDDA/PSS)_4$. In other words, the absorption at 225 nm and the broad absorption are ascribed to PSS and FMAC, respectively. As shown in the insets of the figure, the absorbance at 260 nm increased in proportion with the number of bilayers. This linear growth indicates that both FDCA and FMAC can be quantitatively deposited in the LbL fashion. Figure 2–5 shows AFM images of anionic or cationic fullerene LbL films: (a) a $(PDDA/FDCA)_6$ LbL film and (b) a $(FMAC/PSS)_5/FMAC$ LbL film. The bright area on the right side is the surface of the LbL film and the dark area on the left side is the surface of the quartz substrate exposed by scratching. Both LbL thin films were pinhole-free and the surface roughness was less than 10 nm, suggesting homogeneous deposition of FDCA or FMAC. From the difference in height between these levels, the total thickness was evaluated to be 40 nm for both anionic fullerene and cation LbL films. As shown in Figure 2–6, the thicknesses of fullerene LbL films increased in proportion with the number of bilayers. The linear growth is consistent with the linear increase in the absorbance mentioned above, suggesting again quantitative deposition of both FDCA and FMAC in the LbL fashion. From the slopes in Figure 2–6, the bilayer thickness was evaluated to be 5.8 nm for the anionic fullerene LbL film and 4.5 nm for the cationic fullerene LbL film.

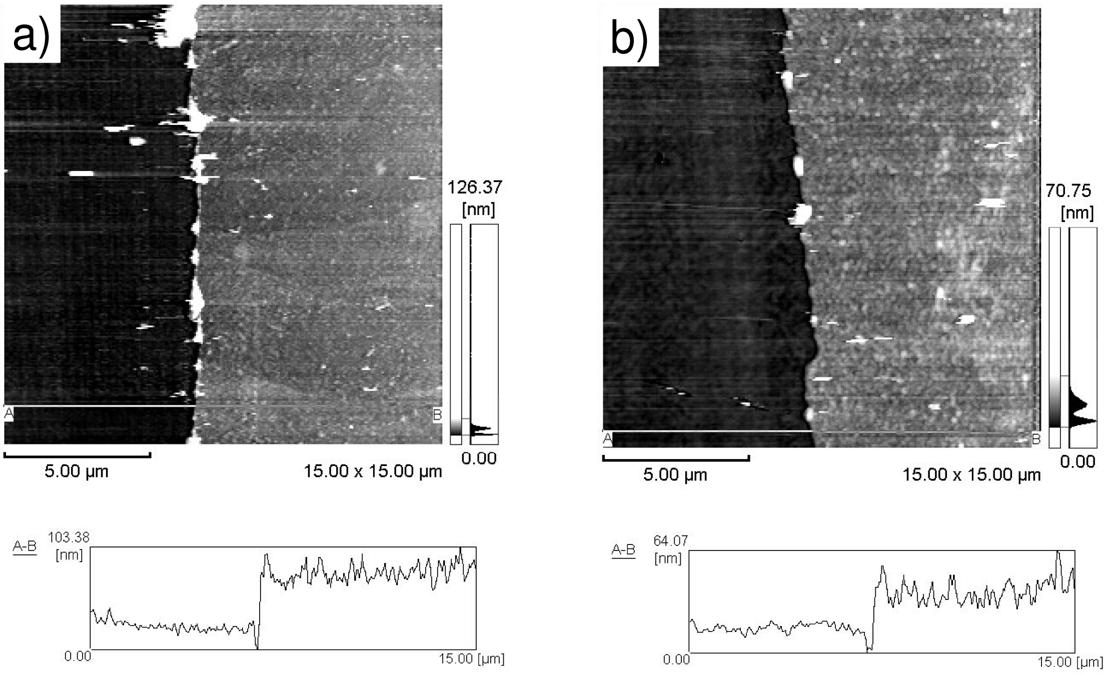

Figure 2–5. AFM images of fullerene LbL films on quartz substrates: a) $(PDDA/FDCA)_6$ and b) $(FMAC/PSS)_5/FMAC$ films. In each image, the left side of the film was scratched out.

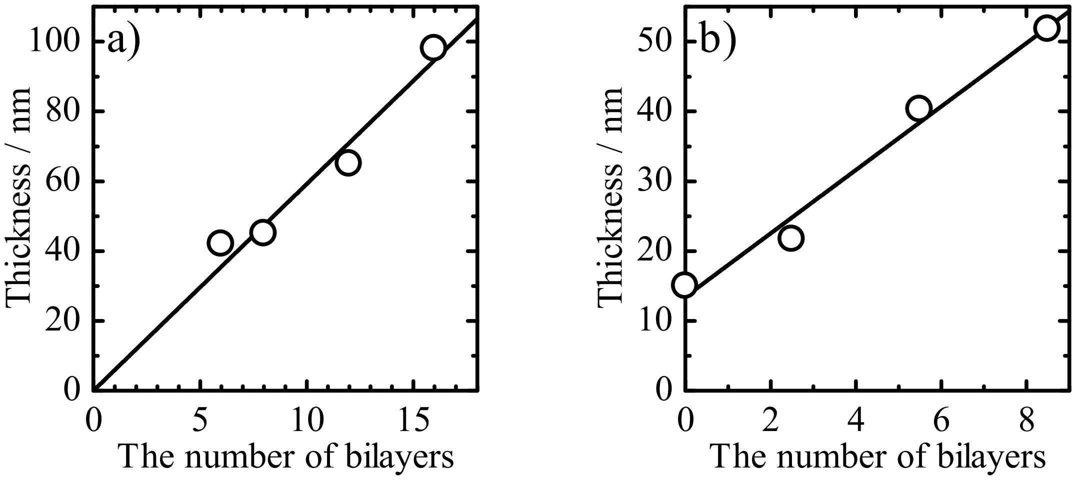

Figure 2–6. Plots of the thickness of fullerene LbL films against the number of bilayers: a) PDDA/FDCA (6, 8, 12, 16 bilayers) and b) FMAC/PSS (0, 2.5, 5.5, 8.5 bilayers) where the thickness of 0 bilayers is due to a precursor film of $(PDDA/PSS)_4$.

From the absorption band of PSS at 225 nm, the author can evaluate the thickness of PSS layer in the cationic fullerene LbL film by using an absorption coefficient of 170,000 cm^{-1} at 225 nm, which was measured for a spincoating film of PSS. Figure 2–7 shows the thickness of PSS layers plotted against the number of bilayers. From the slope in Figure 2–7, the monolayer thickness of PSS was estimated to be 0.5 nm. Consequently, the monolayer thickness of FMAC was estimated to be 4 nm. In other words, the volume fraction of FMAC in the cationic fullerene LbL film is as large as ~80 vol%, suggesting that there exist conductive pathways of fullerene in the LbL film as described below. On the other hand, as shown in Figure 2–4a, no absorption of PDDA was observed for the anionic fullerene LbL films. Therefore, the author cannot quantitatively estimate the volume fraction of each component in the anionic fullerene LbL films. The author will discuss later the electron mobility in the cationic fullerene LbL film on the basis of the volume fraction.

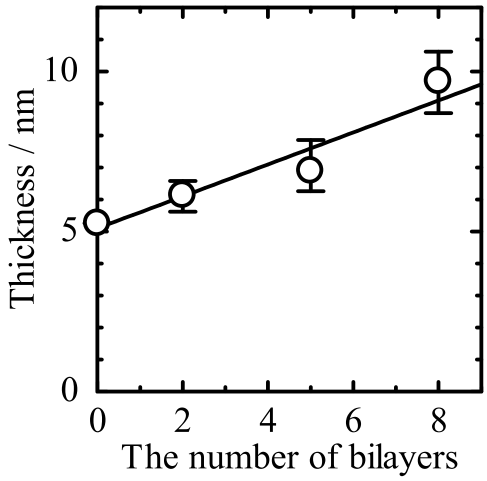

Figure 2–7. Plots of the thickness of PSS layers in cationic fullerene LbL films against the number of bilayers. The thickness is evaluated by using an absorption coefficient of 170,000 cm^{-1} at 225 nm for PSS.

It is worth noting that the particle size of fullerene vesicles in the aqueous solutions is more than 10 times larger than the monolayer thickness of the fullerene LbL films. As shown in Figure 2–5, there are no signs of the direct deposition of such large vesicles as they are. Boxer and co-workers proposed that the adsorption of vesicles on a substrate results in bilayer formation in the following four steps[39,40] 1) adsorption of single vesicle on a substrate, 2) fusion of vesicles on the surface to form larger vesicles, 3) rupture of the fused vesicles to form bilayer disks on the surface, 4) merging of the isolated bilyer disks to form a continuous bilayer film. Consequently, the film thickness should correspond to the shell thickness of bilayer vesicles. As mentioned above, the shell thickness of bilayer FMAC vesicles is known to be 3–6 nm, which is in good agreement with the monolayer thickness of the cationic fullerene LbL films (4 nm). The author therefore concludes that fullerene LbL films are formed in a fashion similar to that described above and hence homogeneous and pin-hole free. Figure 2–8 summarizes the proposed formation mechanism and the layered structure of fullerene LbL films.

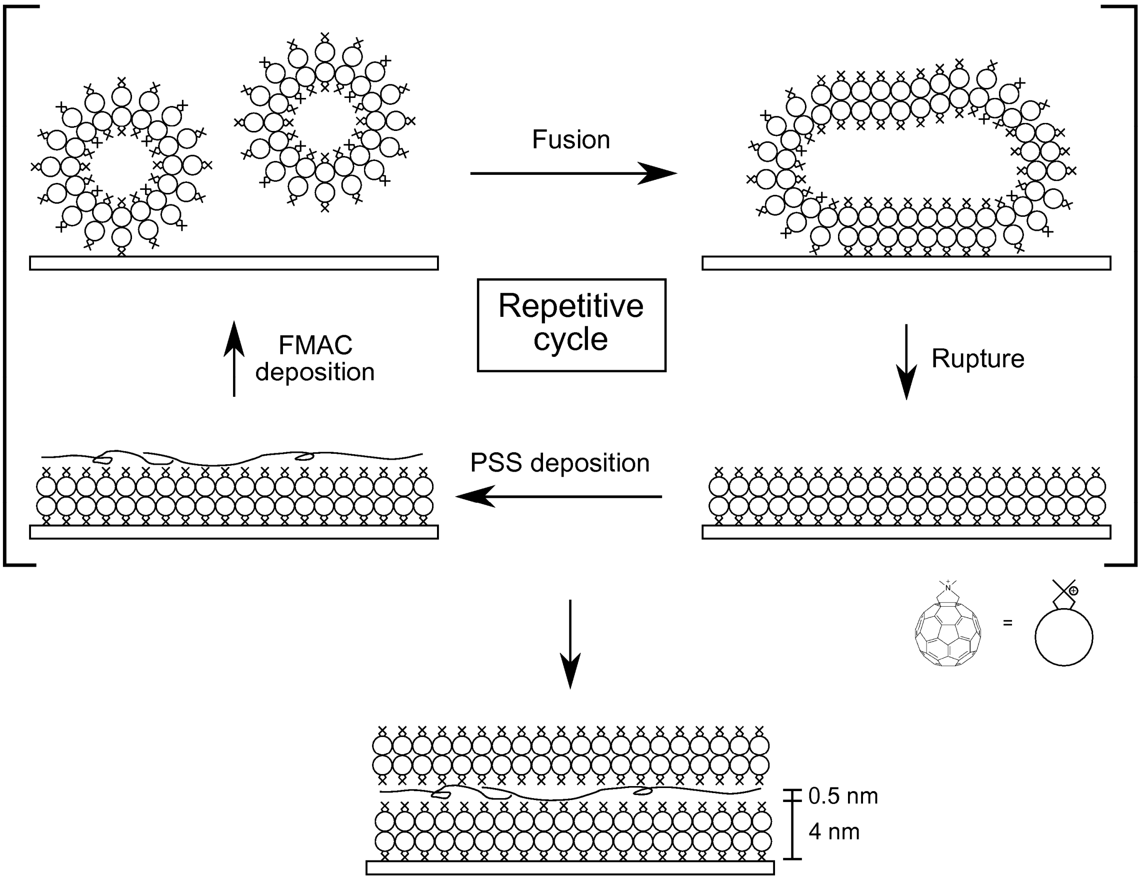

Figure 2–8. Schematic illustration of the proposed formation mechanism and the resultant layered structure of fullerene LbL films.

2.3.3. *Conductive Properties of Fullerene LbL Films*

2.3.3.1. *C_{60}:PS Blend Films*

To discuss the conductive properties of fullerene LbL films, the author first measured the electronic properties such as conductivity σ and electron mobility μ_e of C_{60}:PS blend films for comparison. The volume fraction of C_{60} in the blend film was varied from 24 to 72 vol%. The conductivity σ of C_{60}:PS blend films was evaluated to be 2×10^{-8} S cm^{-1} at a C_{60} fraction of 72 vol% and 4×10^{-11} S cm^{-1} at a C_{60} fraction of 39 vol% from the surface resistivity measurement. Note that the conductivity of a C_{60}:PS blend film (24 vol% C_{60}) was too low to be measured because of undetectable current. The electron mobility μ_e of C_{60}:PS blend films was evaluated from the space-charge limited current. Figure 2–9a shows semi-logarithmic plots of the J–V characteristics of C_{60}:PS blend films against $V - V_{BI} - V_{RS}$: The circles, triangles, and squares represent the J–V characteristics of C_{60}:PS blend films with a C_{60} fraction of 72, 39, and 24 vol%, respectively. The solid lines represent the fitting curves by using eq. 2–1. Table 2–1 summarizes μ_e of C_{60}:PS blend films evaluated from the fitting analysis. As shown in Figure 2–9b, μ_e increased with an increase in the volume fraction of C_{60}, suggesting that a better electric network was fixed for the transport of charge carriers at higher volume fractions of C_{60} in the blend films. These values are in good agreement with those in previous reports.[35,41,42] This ensures the reliability of the measurements.

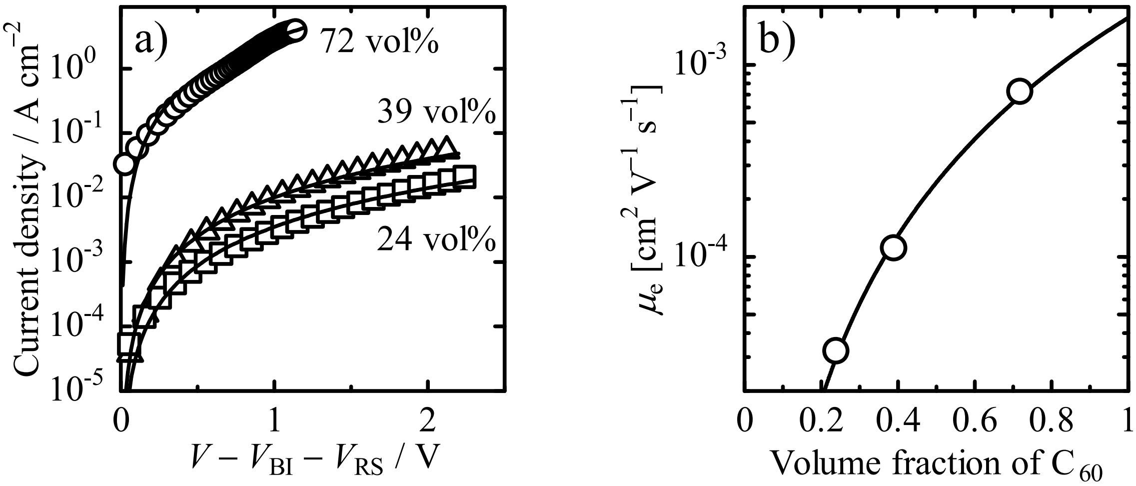

Figure 2–9. a) Semi-logarithmic plots of the J–V characteristics of C_{60}:PS blend films against $V - V_{BI} - V_{RS}$: The circles, triangles, and squares represent plots of C_{60}:PS blend film of 72 vol% (film thickness $d = 45$ nm, $V_{BI} = 0.5$ V, series resistance $r_s = 12\ \Omega$, $\mu_e = 7 \times 10^{-4}$ cm^2 V^{-1} s^{-1}), 39 vol% ($d = 150$ nm, $V_{BI} = 0.2$ V, $r_s = 10\ \Omega$, $\mu_e = 1 \times 10^{-4}$ cm^2 V^{-1} s^{-1}), and 24 vol% ($d = 140$ nm, $V_{BI} = 0.2$ V, $r_s = 10\ \Omega$, $\mu_e = 3 \times 10^{-5}$ cm^2 V^{-1} s^{-1}) C_{60} fraction, respectively. The solid lines represent the fitting curves using eq. 2–1. b) Plots of μ_e of C_{60}:PS blend films against the volume fraction of C_{60}. The solid line is guided by eye.

Table 2–1. The conductivity σ and the electron mobility μ_e of the C_{60}:PS blend film and fullerene LbL films.

	C_{60} fraction / vol%	σ / S cm^{-1}	μ_e / $cm^2\ V^{-1}\ s^{-1}$
C_{60}:PS blend film	0.24	—[a]	3×10^{-5}
	0.39	4×10^{-11}	1×10^{-4}
	0.72	2×10^{-8}	7×10^{-4}
PDDA/FDCA LbL film	—	6×10^{-10}	—
FMAC/PSS LbL film	0.8	5×10^{-8}	3×10^{-5}

[a] The value of σ for a C_{60}:PS blend film with 24 vol% C_{60} fraction was not obtained because of the large surface resistivity.

2.3.3.2. *Fullerene LbL Films*

In the same way, the conductivity of fullerene LbL films was estimated to be 6×10^{-10} S cm^{-1} for FDCA and 5×10^{-8} S cm^{-1} for FMAC. These values are comparable to those of C_{60}:PS blend films with higher C_{60} fractions. This finding is consistent with the previous report that LbL films exhibit efficient hole transport comparable to spincoat films,[30] suggesting that there exist percolating networks in the direction normal to the substrate even in the LbL films. Such effective percolation in the fullerene LbL films is owing to the large volume fraction of ionic fullerenes as high as ~80 vol%, in addition to the interpenetrating characteristics of LbL films as reported previously.[30] To prove the electron transport in the networks, the author evaluated the electron mobility μ_e of cationic fullerene LbL films. Figure 2–10 shows the semi-logarithmic plots of the J–V characteristics of cationic fullerene LbL films against $V - V_{BI} - V_{RS}$. The solid line represents fitting curves for the J–V characteristics by using eq. 2–1 where ε_r was estimated to be 4.2 considering the volume fraction of fullerene in LbL films. As a result, μ_e of cationic fullerene LbL films was 3 ×

10^{-5} cm^2 V^{-1} s^{-1}. This value is one order of magnitude smaller than that of C_{60}:PS blend film at a similar fraction of C_{60} (~72 vol%), but is rather comparable to that at a lower fraction of C_{60} (24 vol%). This result is different from the case of LbL films based on poly(*p*-phenylenevinylene) (PPV) and PSS. As reported previously, the hole mobility μ_h of PPV/PSS LbL films is even higher than that of PPV pristine films because of the interpenetrating structure.[43] In polymer LbL films, a polyelectrolyte chain can easily contact with other chains interpenetrating from the adjacent layers because there are many adsorption sites in a molecule. In contrast, fullerene bilayers cannot directly contact with other bilayers, because insulated by PSS anions as shown in Figure 2–8. Nonetheless, μ_e of cationic fullerene LbL films is comparable to the hole mobility in PPV/PSS LbL films that can serve as an efficient hole-transporting material in organic solar cells. This is probably because the PSS insulating layer is as thin as 0.5 nm and therefore unlikely to prevent the charge transport. The author therefore concludes that the cationic fullerene LbL films also can serve as an efficient electron-transporting material.

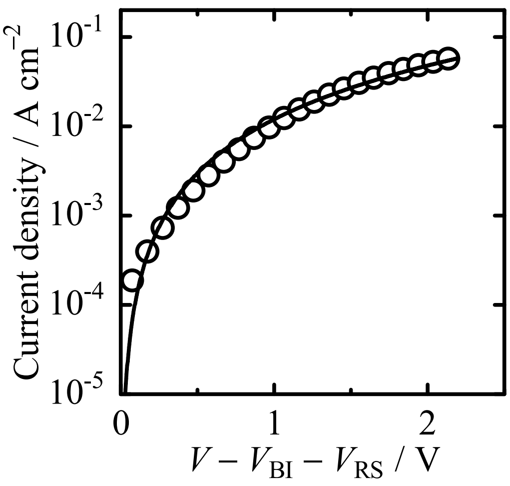

Figure 2–10. Semi-logarithmic plots of the J–V characteristics of cationic fullerene LbL films against V–V_{BI}–V_{RS} (d = 103 nm, V_{BI} = 0.9 V, r_s = 10 Ω, $\mu_e = 3 \times 10^{-5}$ cm^2 V^{-1} s^{-1}). The solid line represents the fitting curve using eq. 2–1.

2.4. Conclusions

The author fabricated fullerene ultrathin films by the LbL deposition and characterized the layered structure and the conductive properties. Two types of water-soluble fullerenes were employed: one is an anionic fullerene $C_{61}(COO^-)_2$ (FDCA) and the other is a cationic fullerene $C_{60}C_2H_4N(CH_3)_2^+$ (FMAC). From the dynamic light scattering measurement, the particle size dispersed in aqueous solutions was evaluated to be ~20 nm (the major fraction) and ~70 nm (the minor fraction) for FDCA and ~60 nm (the minor fraction) and ~180 nm (the major fraction) for FMAC. The zeta potential was as high as −28 mV for FDCA and +27 mV for FMAC, suggesting that both water-soluble fullerenes are stably dispersed as polyelectrolytes in aqueous solutions. The author ascribed the stable polyelectrolytes to fullerene vesicles on the basis of comparison with previous reports. The fullerene ultrathin films were successfully deposited by LbL assembly of PDDA/FDCA and

FMAC/PSS. The film thickness increased in proportion to the number of deposition cycles, which is indicative of the linear growth in the LbL fashion. The bilayer thickness was evaluated to be 5.8 nm for PDDA/FDCA and 4.5 nm for FMAC/PSS LbL films. The monolayer thickness of FMAC in the LbL film was estimated to be 4 nm, which is consistent with the shell thickness of FMAC vesicles in aqueous solutions. The author therefore concludes that fullerene LbL films consist of counter polymer films and fullerene bilayer films formed by rupture of fullerene vesicles. The conductivity σ was 6×10^{-10} S cm^{-1} for PDDA/FDCA and 5×10^{-8} S cm^{-1} for FMAC/PSS LbL films. These values are comparable to that of C_{60}:PS blend films with higher C_{60} fractions, suggesting that there exist effective percolating networks in the fullerene LbL films. Indeed, the electron mobility μ_e of cationic fullerene LbL films was as high as 3×10^{-5} cm^2 V^{-1} s^{-1}. This is primarily due to the large volume fraction of FMAC, which was as high as ~80 vol%, in the cationic fullerene LbL film. The electron mobility μ_e of cationic fullerene LbL films is comparable to the hole mobility in PPV/PSS LbL films that can serve as an efficient hole-transporting material in organic solar cells. The author therefore concludes that the LbL assembly of water-soluble fullerenes is useful for fabricating efficient electron-transporting ultrathin films of fullerene materials with a precisely-controlled thickness.

References and Notes

(1) Makarova, T. L. *Semiconductors* **2001**, *35*, 243–278.

(2) Echegoyen, L.; Echegoyen, L. E. *Acc. Chem. Res.* **1998**, *31*, 593–601.

(3) Guldi, D. M.; Prato, M. *Acc. Chem. Res.* **2000**, *33*, 695–703.

(4) Imahori, H.; Sakata, Y. *Eur. J. Org. Chem.* **1999**, 2445–2457.

(5) Ariga, K.; Nakanishi, T.; Hill, J. P. *Curr. Opin. Colloid Interface Sci.* **2007**, *12*, 106–120.

(6) Guldi, D. M.; Zerbetto, F.; Georgakilas, V.; Prato, M. *Acc. Chem. Res.* **2005**, *38*, 38–43.

(7) Nakamura, E.; Isobe, H. *Acc. Chem. Res.* **2003**, *36*, 807–815.

(8) Cassell, A. M.; Asplund, C. L.; Tour, J. M. *Angew. Chem. Int. Ed.* **1999**, *38*, 2403–2405.

(9) Georgakilas, V.; Pellarini, F.; Prato, M.; Guldi, D. M.; Melle-Franco, M.; Zerbetto, F. *Proc. Natl. Acad. Sci. U.S.A.* **2002**, *99*, 5075–5080.

(10) Sano, M.; Oishi, K.; Ishi-i, T.; Shinkai, S. *Langmuir* **2000**, *16*, 3773–3776.

(11) Zhou, S.; Burger, C.; Chu, B.; Sawamura, M.; Nagahama, N.; Toganoh, M.; Hackler, U. E.; Isobe, H.; Nakamura, E. *Science* **2001**, *291*, 1944–1947.

(12) Burger, C.; Hao, J.; Ying, Q.; Isobe, H.; Sawamura, M.; Nakamura, E.; Chu, B. *J. Colloid Interface Sci.* **2004**, *275*, 632–641.

(13) Nakanishi, T.; Schmitt, W.; Michinobu, T.; Kurth, D. G.; Ariga, K. *Chem. Commun.* **2005**, 5982–5984.

(14) Decher, G. *Science* **1997**, *277*, 1232–1237.

(15) Ariga, K.; Hill, J. P.; Ji, Q. *Phys. Chem. Chem. Phys.* **2007**, *9*, 2319–2340.

(16) Hammond, P. T. *Adv. Mater.* **2004**, *16*, 1271–1293.

(17) Caruso, F. *Adv. Mater.* **2001**, *13*, 11–22.

(18) Liu, Y.; Wang, Y.; Lu, H.; Claus, R. O. *J. Phys. Chem. B* **1999**, *103*, 2035–2036.

(19) Piok, T.; Brands, C.; Neyman, P. J.; Erlacher, A.; Soman, C.; Murray, M. A.; Schroeder, R.; Graupner, W.; Heflin, J. R.; Marciu, D.; Drake, A.; Miller, M. B.; Wang, H.; Gibson, H.; Dorn, H. C.; Leising, G.; Guzy, M.; Davis, R. M. *Synth. Met.* **2001**, *116*, 343–347.

(20) Mattoussi, H.; Rubner, M. F.; Zhou, F.; Kumar, J.; Tripathy, S. K.; Chiang, L. Y. *Appl. Phys. Lett.* **2000**, *77*, 1540–1542.

(21) Durstock, M. F.; Spry, R. J.; Baur, J. W.; Taylor, B. E.; Chiang, L. Y. *J. Appl. Phys.* **2003**, *94*, 3253–3259.

(22) Li, H.; Zhou, Y.; Li, Y.; Song, Y.; Fang, H.; Xiao, S.; Liu, H.; Gan, H.; Jiu, T.; Zhu, D. *Chem. Phys. Lett.* **2004**, *383*, 230–234.

(23) Rosenlehner, K.; Schunk, T.; Jux, N.; Brettreich, M.; Hirsch, A. *Org. Biomol. Chem.* **2008**, *6*, 2697–2705.

(24) Mwaura, J. K.; Pinto, M. R.; Witker, D.; Ananthakrishnan, N.; Schanze, K. S.; Reynolds, J. R. *Langmuir* **2005**, *21*, 10119–10126.

(25) Guldi, D. M.; Zilbermann, I.; Anderson, G.; Kotov, N. A.; Tagmatarchis, N.; Prato, M. *J. Mater. Chem.* **2005**, *15*, 114–118.

(26) Jiang, L.; Chang, Q.; Ouyang, Q.; Liu, H.; Wang, Y.; Zhang, X.; Song, Y.; Li, Y. *Chem. Phys.* **2006**, *324*, 556–562.

(27) Lamparth, I.; Hirsch, A. *J. Chem. Soc., Chem. Commun.* **1994**, 1727–1728.

(28) Maggini, M.; Scorrano, G. *J. Am. Chem. Soc.* **1993**, *115*, 9798–9799.

(29) Bullard-Dillard, R.; Creek, K. E.; Scrivens, W. A.; Tour, J. M. *Bioorg. Chem.* **1996**, *24*, 376–385.

(30) Wakizaka, D.; Fushimi, T.; Ohkita, H.; Ito, S. *Polymer* **2004**, *45*, 8561–8565.

(31) Hebard, A. F.; Haddon, R. C.; Fleming, R. M.; Kortan, A. R. *Appl. Phys. Lett.* **1991**, *59*, 2109–2111.

(32) Asmatulu, R.; Geist, B.; Spillman, W. B. Jr; Claus, R. O. *Smart Mater. Struct.* **2005**, *14*, 1493–1500.

(33) The value of ε_r of PSS was calculated as the square of the refractive index of PSS taken from Ref 34.

(34) Liu, L.; Li, P.; Asher, S. A. *J. Am. Chem. Soc.* **1999**, *121*, 4040–4046.

(35) Tuladhar, S. M.; Poplavskyy, D.; Choulis, S. A.; Durrant, J. R.; Bradley, D. D. C.; Nelson, J. *Adv. Funct. Mater.* **2005**, *15*, 1171–1182.

(36) Guldi, D. M.; Hungerbühler, H.; Asmus, K.-D. *J. Phys. Chem.* **1995**, *99*, 13487–13493.

(37) Guldi, D. M.; Hungerbühler, H.; Asmus, K.-D. *J. Phys. Chem. A* **1997**, *101*, 1783–1786.

(38) Freitas, C.; Müller, R. H. *J. Microencapsulation* **1999**, *16*, 59–71.

(39) Johnson, J. M.; Ha, T.; Chu, S.; Boxer, S. G. *Biophys. J.* **2002**, *83*, 3371–3379.

(40) Schönherr, H.; Johnson, J. M.; Lenz, P.; Frank, C. W.; Boxer, S. G. *Langmuir* **2004**, *20*, 11600–11606.

(41) Mihailetchi, V. D.; Koster, L. J. A.; Blom, P. W. M.; Melzer, C.; de Boer, B.; van Duren, J. K. J.; Janssen, R. A. J. *Adv. Funct. Mater.* **2005**, *15*, 795–801.

(42) Adamopoulos, G.; Heiser, T.; Giovanella, U.; Ould-Saad, S.; van de Wetering, K. I.; Brochon, C.; Zorba, T.; Paraskevopoulos, K. M.; Hadziioannou, G. *Thin Solid Films* **2006**, *511–512*, 371–376.

(43) Ogawa, M.; Kudo, N.; Ohkita, H.; Ito, S.; Benten, H. *Appl. Phys. Lett.* **2007**, *90*,

223107.

Chapter 3

Conductive and Photovoltaic Properties of Multilayered Ultrathin Films Designed by Layer-by-Layer Assembly of Titanium Oxides

3.1. Introduction

Titanium oxide, titania, has drawn attention because of its attractive optical and electronic characteristics. Various applications have been reported, such as optical filters, photocatalysts, and electronic devices.[1–4] Titania thin films have been fabricated not only by dry processes such as thermal deposition, sputtering, and chemical vapor deposition[1,3,5] but also by the sol–gel method and other solution processes.[6–8] The solution processes are suitable for large-area and low-temperature fabrication, and are also applicable to the fabrication of organic–inorganic hybrid materials. Titanium alkoxides have been widely used as a precursor of titania. However, it is difficult to control the particle size precisely because of the rapid reaction of alkoxides in water. Thus, chemical additives are needed to control hydrolysis and condensation moderately.[9] Recently, bis(ammonium lactato)titanium dihydroxide (TALH) has been developed as a useful starting material of titania synthesis from an aqueous solution, because TALH is stable even in water at ambient temperature in contrast to titanium alkoxides. The hydrolysis and conversion of TALH into titania have been studied by Möckel and co-workers in detail. They reported that titania converted from TALH is composed of monodisperse nanoparticles.[10] Furthermore, TALH serves as a negatively-charged ion in water, and is therefore applicable as an adsorbate in the layer-by-layer (LbL) deposition technique. Consequently, various nanostructures of titania such as core–shell nanoparticle,[11] nanotube,[12] and three-dimensional porous film[13,14] have been reported so far.

The LbL deposition technique, which has been developed by Decher, is based on electrostatic self-assembly of oppositely-charged species, and is now widely employed as a simple and versatile method for fabricating multilayered nanostructures.[15–18] As mentioned above, there are several reports on titania thin films developed by the LbL assembly of TALH. Caruso and co-workers fabricated multilayered thin films of TALH and some polyelectrolytes by the LbL deposition technique.[19] Kim and co-workers applied titania-based LbL thin films converted from TALH to transparent photocatalyst[20] and anti-reflection film.[21] On the other hand, titania has been widely used as an excellent electron-transporting material in photovoltaic cells. For example, titania nanoporous thin layers are employed as an electron-transporting material in dye-sensitized solar cells,[22] and titania nanoparticles are blended as an electron-accepting material with a conjugated donor polymer in organic–inorganic hybrid solar cells.[23] Thus, titania-based LbL thin films are a promising material in multilayered photovoltaic cells. However, there are no reports on the conductive properties of titania-based LbL thin films.

In this chapter, the author fabricates titania-based LbL films from TALH, characterizes the conductive properties, and demonstrates their application to photovoltaic cells. The dispersion state of TALH in water is analyzed by the dynamic light scattering measurement to discuss the deposition of TALH in the LbL assembly. The layered structure of the films is revealed by absorption and AFM measurements. The conductivity and electron mobility of the titania-based LbL films are evaluated quantitatively, suggesting that the titania-based LbL films can serve as an efficient electron-transporting material. Finally, photovoltaic properties are also demonstrated with multilayered solar cells designed by LbL assembly of TALH/poly(diallyldimethylammonium chloride) (PDDA) and poly(*p*-phenylenevinylene) (PPV)/poly(sodium 4-styrenesulfonate) (PSS).

3.2. Experimental Section

3.2.1. *Materials*

For the LbL deposition, water was purified by deionization, distillation, and passing through a filtration system (Barnstead Nanopure II). An aqueous solution of titanium(IV) bis(ammonium lactato)dihydroxide (TALH; Aldrich, 50 wt% in water), which is a precursor of titania, was diluted to 5 wt% aqueous solution with water. An aqueous solution of poly(diallyldimethylammonium chloride) (PDDA; Aldrich, 20 wt% in water, M_w = 100,000–200,000 g mol^{-1}) was diluted to 1 mg mL^{-1} with 0.5 M NaCl aqueous solution. Poly(*p*-xylene tetrahydrothiophenium chloride) (pre-PPV; Aldrich, 0.25 wt% in water), which is a precursor of poly(*p*-phenylenevinylene) (PPV), was diluted to 1 mM with water. Poly(sodium 4-styrenesulfonate) (PSS; Aldrich, M_w = 70,000 g mol^{-1}) was dissolved at 10 mM with water. The pre-PPV solution was adjusted to pH 8–9 with an NaOH aqueous solution. An aqueous solution of poly(3,4-ethylenedioxythiophene):poly(4-styrenesulfonate) (PEDOT:PSS; Aldrich, 1.3 wt% dispersion in water, conductive grade) was diluted to 10 mM with water. These solutions were employed as polyelectrolyte solutions for the LbL deposition. An aqueous solution of anatase TiO_2 nanoparticles with a diameter of 20 nm (Solaronix SA) was used for the fabrication of a nanoporous (np)-TiO_2 film. Poly(3-hexylthiophene) (P3HT; Aldrich, regioregular, M_n = 45,000–65,000, 99.995%) was dissolved to 1 wt% solution with chlorobenzene. Figure 3–1 shows the chemical structures of materials employed in this chapter.

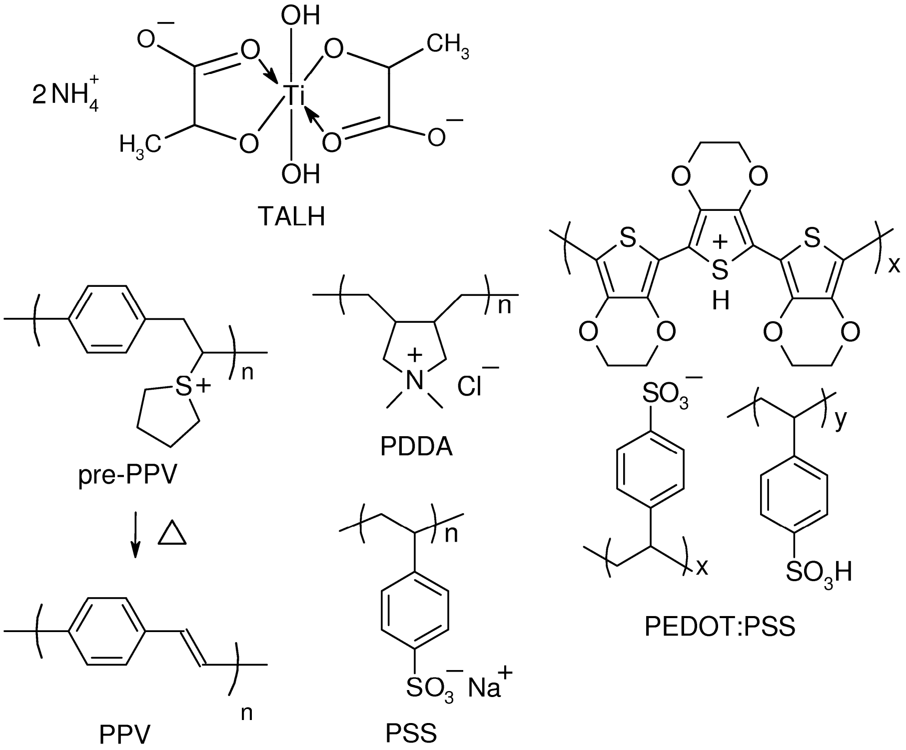

Figure 3–1. Chemical structures in this chapter.

3.2.2. *Fabrication of LbL Films*

For UV–visible absorption and sheet-resistance measurements, quartz substrates were employed for the LbL deposition. These quartz substrates were cleaned by ultrasonication in toluene, acetone, and ethanol for 15 min each, then dried with a N_2 flow, and treated with a UV–O_3 cleaner for 1 h. The substrates were immersed in a cationic solution of PDDA for 15 min, and rinsed in water twice for 2 min and 1 min each. Subsequently, they were immersed in an anionic solution of TALH for 15 min, and rinsed in water for 3 min. This cycle gives one bilayer of PDDA/TALH. The LbL films with n bilayers of PDDA and TALH are abbreviated as (PDDA/TALH)$_n$. Note that PDDA/TALH LbL films were not dried after each immersion and rinsing. The PDDA/TALH LbL films were annealed in air to convert to PDDA/TiO$_x$ LbL films. The LbL films were annealed first at 65 °C for 3 h, and then at different temperatures from 70 to 220 °C for 24 h. Similarly, pre-PPV/TALH LbL films were fabricated as described in Ref 24 and PPV/TiO_x LbL films were obtained by annealing at 220 °C for 12 h under vacuum.

For the electron-mobility measurement, the indium–tin-oxide (ITO)-coated glass substrates (10 Ω square^{-1}) were employed for the LbL deposition. The substrates were cleaned and treated as described above. First, a buffer layer was prepared by the LbL deposition of PEDOT:PSS and PDDA as reported previously.[25] The thickness was 100 nm. Second, PDDA/TALH LbL films were fabricated on the buffer layer. Third, the LbL film was annealed as described above. Finally, Al was thermally deposited at 2.5×10^{-6} Torr on top of the LbL film. The thickness of Al was 100 nm. The layered structure is abbreviated as ITO|$(PEDOT:PSS/PDDA)_{20}$|$(PDDA/TiO_x)_{30}$|Al. For comparison, np-TiO_2 films were prepared by spincoating followed by sintering at 150 °C in air for the sheet-resistance and electron mobility measurements.

Photovoltaic cells with a planar heterojunction structure were fabricated by the LbL deposition technique. First, an acceptor layer was fabricated by the LbL assembly of TALH and PDDA on a cleaned ITO substrate as described above. Second, a donor layer was fabricated by the LbL assembly of pre-PPV and PSS as reported previously.[24] Third, a buffer layer of PEDOT:PSS was prepared by spincoating, followed by annealing at 100 °C for 24 h under vacuum. Finally, Au was thermally deposited. The thickness was 80 nm for the PEDOT:PSS layer and 100 nm for the Au electrode. The layered structure shown in Figure 3–2 is abbreviated as ITO|$(PDDA/TiO_x)_5$/PDDA|$(PPV/PSS)_5$/PPV|PEDOT:PSS|Au. For comparison, dense TiO_2 (d-TiO_2) films were prepared by the sol–gel method as reported previously.[26]

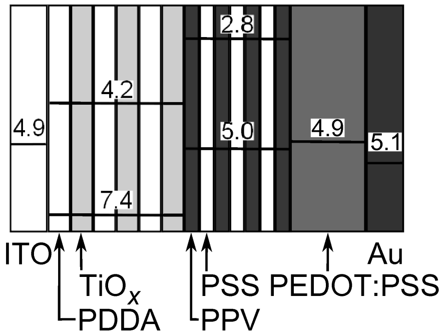

Figure 3–2. The layered structure and the energy diagram of the photovoltaic cell with the TiO$_x$ LbL film.

3.2.3. *Measurements*

UV–visible absorption spectra of PDDA/TALH LbL films were measured before and after thermal annealing with a spectrophotometer (Hitachi, U-3500). The thickness and surface morphology of LbL films were measured with an atomic force microscope (AFM, Shimadzu, SPM-9500J) in contact mode. The particle size of TALH in water was evaluated by the dynamic light scattering measurement (DLS, Otsuka Electronics, ELS-Z2). The dynamic light scattering data were analyzed by the cumulant approach. The surface resistivity of LbL films and np-TiO$_2$ film was measured with a ring probe (Mitsubishi Chemical Analytech, UR-SS) connected to a digital electrometer (Advantest, R8252). The conductivity σ is obtained from an inverse of the volume resistivity, which is given by the product of the surface resistivity and the film thickness. The *J–V* characteristics of devices were measured with a DC voltage current source/monitor (Advantest, R6243). The electron mobility μ_e was evaluated from the space-charge limited current (SCLC), which is described by

$$J = \frac{9}{8}\varepsilon_0 \varepsilon_\mathrm{r} \mu_\mathrm{e} \frac{(V - V_\mathrm{BI} - V_\mathrm{RS})^2}{d^3} \qquad (3\text{–}1)$$

where ε_0 is the permittivity of free space and ε_r is the relative dielectric constant. The effective ε_r of multicomponent films was estimated as the volume average of each component where $\varepsilon_r(TiO_2)$ and ε_r(PDDA) were set at 45[27] and 1.8,[28] respectively. The value of V_{RS} is the voltage drop, which was given by the product of the series resistance r_s, the device area, and the current density J. The built-in-voltage V_{BI} and r_s were treated as fitting parameters.[29] The J–V characteristics of photovoltaic cells were measured with the DC voltage current source/monitor in the dark and under AM1.5G simulated solar illumination at 100 mW cm^{-2}. The external quantum efficiency spectra were measured with the digital electrometer under monochromatic light illumination from a 500-W Xe lamp (Thermo Oriel, Model 66921) with a monochromator (Thermo Oriel, UV–visible Conerstone) and several optical cut-filters (IRQ80, HOYA L-38, and AND-50S-25). All measurements were performed in air at room temperature.

3.3. Results and Discussion

3.3.1. *TALH Dispersion in Water*

To clarify the deposition state of TALH in water, the author measured the dynamic light scattering of an aqueous solution of TALH. As shown in Figure 3–3, the average particle size of TALH was estimated to be 5.7 nm by the cumulant approach, with a narrow distribution: the polydispersity index less than 0.01. The particle size remained the same even after several hours, suggesting that TALH is stable and does not form larger aggregates (oligomer or cluster) in water. These results are consistent with previous studies on TiO_x nanoparticles thermally converted from TALH at < 100 °C, in which the size of the TiO_x nanoparticles was reported to be 3–5 nm.[30,31] Thus, the stability of TALH against both hydrolysis and condensation to TiO_x is probably due to two bulky ligands in TALH, which is a chelate compound of a titanium ion coordinated by two ammonium lactates. The author therefore concludes that TALH is dispersed in water as small aggregates with a diameter of ~6 nm, which can be deposited on a substrate as described later.

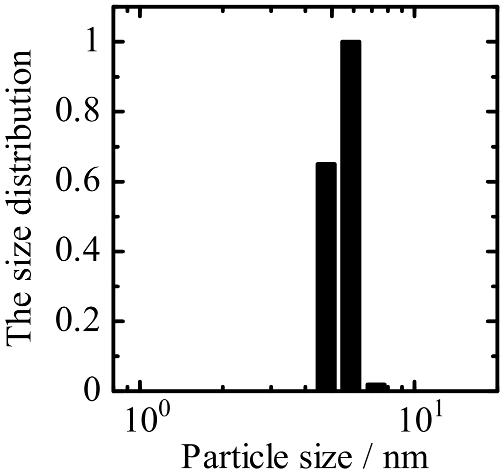

Figure 3–3. Normalized size distribution of TALH nanoparticles dispersed in water. The concentration of TALH is 5 wt% in aqueous solution.

3.3.2. *Fabrication of TiO_x LbL Films*

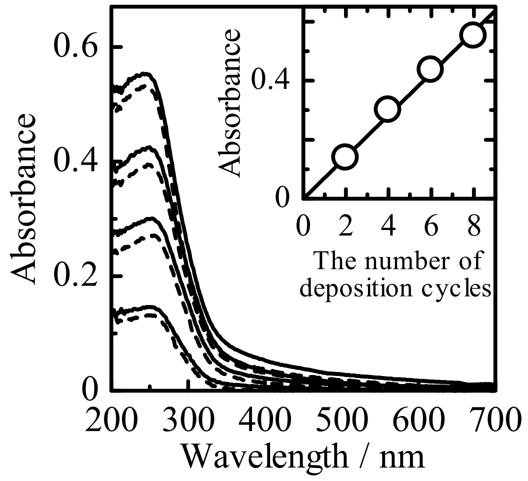

Figure 3–4. Absorption spectra of PDDA/TALH LbL films (2, 4, 6, 8 deposition cycles) before (broken lines) and after (solid lines) thermal annealing. The inset shows the absorbance at 250 nm plotted against the number of deposition cycles.

Figure 3–4 shows absorption spectra of PDDA/TALH LbL films on quartz substrates after various numbers of deposition cycles (n = 2, 4, 6, 8). The broken and solid lines represent the absorption spectra before and after thermal annealing at 95 °C for 24 h, respectively. The absorption at ~250 nm is ascribed to TiO_x because PDDA has no absorption in this wavelength range and TALH has slightly different absorption. This absorption slightly increased after thermal annealing at 95 °C, as shown in the figure, but remained the same after additional thermal annealing at 220 °C for 12 h (data not shown). These results indicate that TALH is partially converted into TiO_x because of drying during the LbL deposition, and completely converted into TiO_x after thermal annealing at 95 °C. As shown in the inset of the figure, the absorbance at 250 nm increased in proportion with the number of deposition cycles. This linear growth indicates that TALH nanoparticles are quantitatively deposited in an LbL fashion. Figure 3–5 shows an AFM image of an LbL film of (PDDA/TiO$_x$)$_6$ on a quartz substrate. The LbL film was pinhole-free with a surface roughness of <10 nm, which is indicative of homogeneous deposition of TALH nanoparticles. The bright area on the right side is the surface of the LbL film and the dark area on the left side is the surface of quartz substrate where the LbL film was scratched out. From the difference in height between these levels, the total thickness of the LbL film was evaluated to be 32 nm. As shown in the inset of Figure 3–5, the thickness of PDDA/TALH LbL films after thermal annealing increased in proportion with the number of deposition cycles. This is consistent with the linear growth in the absorbance mentioned above, suggesting again that TALH nanoparticles are quantitatively deposited in the LbL fashion. From the slope in the inset, the thickness of PDDA/TiO$_x$ bilayer was estimated to be 6.2 ± 0.1 nm.

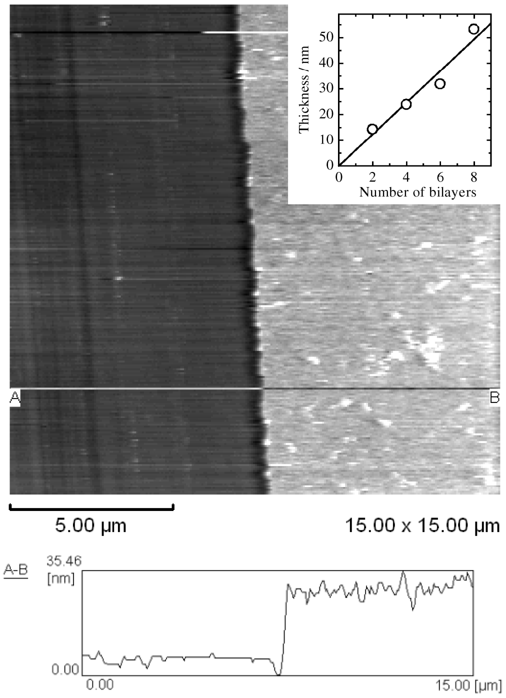

Figure 3–5. AFM image of a PDDA/TiO$_x$ LbL film with 6 bilayers (after annealing). The left side of the film was the surface of quartz substrate where the LbL film was scratched out. The inset shows the thickness of PDDA/TiO$_x$ LbL films plotted against the number of bilayers.

To evaluate the monolayer thickness of TiO$_x$ and PDDA in LbL films, the author estimates the absorption coefficient of TiO$_x$ layer as follows. First, PPV/TiO$_x$ LbL films were prepared by thermal conversion of pre-PPV/TALH LbL films. The thickness of the PPV monolayer can be evaluated using the absorption coefficient 330,000 cm^{-1} at 400 nm.[32] Next, the total thickness of PPV/TiO$_x$ LbL films can be evaluated by AFM measurement as described above. Thus, the thickness and the absorption coefficient of the TiO$_x$ monolayer can be estimated from the difference. Figure 3–6 shows absorption spectra of PPV/TiO$_x$ LbL films with various numbers of bilayers (n = 2, 4, 6) on quartz substrates. The absorption increased in proportion with the number of PPV/TiO$_x$ bilayers as shown by the solid line in the inset). From the slope of the solid line, the monolayer thickness of PPV in PPV/TiO_x LbL films was estimated to be 0.9 ± 0.1 nm. On the other hand, as shown by the broken line in the inset, the total thickness of PPV/TiO_x LbL films also increased in proportion with the number of PPV/TiO_x bilayers. From the slope of the broken line, the bilayer thickness of PPV/TiO_x LbL films was estimated to be 5.7 ± 0.1 nm. Therefore, the monolayer thickness of TiO_x in PPV/TiO_x LbL films was estimated to be 4.8 ± 0.2 nm and the absorption coefficient of the TiO_x layer was evaluated to be 300,000 cm^{-1} at 250 nm. On the basis of the absorption coefficient, the monolayer thickness of PDDA/TiO_x LbL films was estimated to be 2.2 nm for PDDA and 4 nm for TiO_x. Interestingly, the monolayer thickness of TiO_x is 4–5 nm independently of counter polycations, which is consistent with the particle size of TALH in water. Thus, this finding also indicates that TALH nanoparticles are stably dispersed in water and quantitatively adsorbed on a substrate during the LbL deposition.

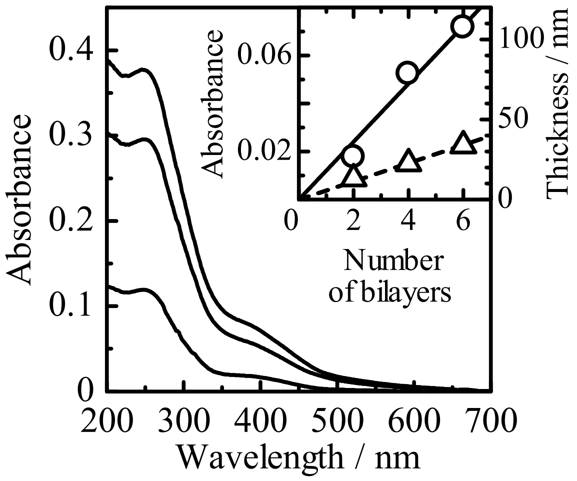

Figure 3–6. Absorption spectra of PPV/TiO_x LbL films (2, 4, 6 bilayers). The inset shows the absorbance at 400 nm (circles, solid line) and the thickness (triangles, broken line) plotted against the number of bilayers.

3.3.3. *Conductive Properties of TiO_x LbL Films*

To discuss the conductive properties of PDDA/TiO_x LbL films, the author measured the conductivity σ and the electron mobility μ_e. For comparison, np-TiO_2 films were prepared by sintering of TiO_2 nanoparticles at 150 °C. Figure 3–7 shows the conductivity σ of PDDA/TiO_x LbL films annealed at different temperatures (open circles) and that of a np-TiO_2 film (closed circle). The conductivity σ of PDDA/TiO_x LbL films was almost constant in the range of $1–3 \times 10^{-9}$ S cm^{-1} below 150 °C. It increased steeply above 180 °C and reached 4×10^{-8} S cm^{-1} at 220 °C, which is rather comparable to that of the np-TiO_2 film (2×10^{-7} S cm^{-1}). These high conductivities σ of PDDA/TiO_x LbL films are indicative of semiconductors although the insulating polymer PDDA is involved in the film. This finding shows that there are conductive carriers and pathways in the LbL film due to percolating networks of TiO_x in the direction normal to the substrate. Higher conductivities σ of PDDA/TiO_x LbL films annealed above 180 °C are probably attributed to degradation of insulating PDDA at higher temperatures.[33]

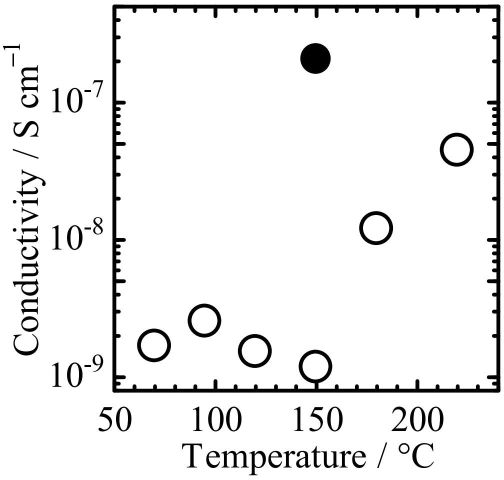

Figure 3–7. Plots of the conductivity of PDDA/TiO$_x$ LbL films (open circles) and a np-TiO$_2$ film (closed circle) against annealing temperatures. The thickness of PDDA/TiO$_x$ LbL film and the np-TiO$_2$ film were 130 nm and 160 nm, respectively.

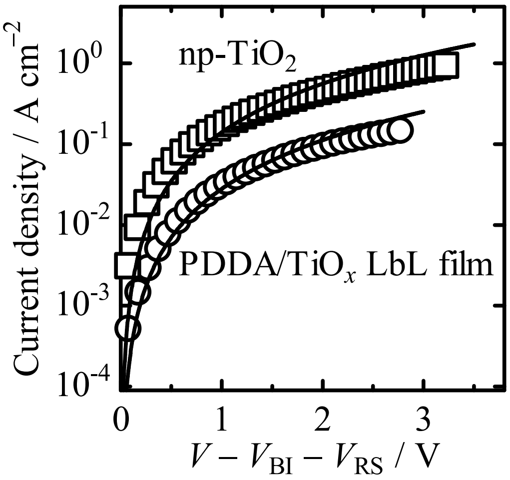

Figure 3–8. Semi-logarithmic plots of the *J–V* characteristics of PDDA/TiO$_x$ LbL (circles) films and np-TiO$_2$ film (squares) against $V{-}V_{BI}{-}V_{RS}$. The solid lines represent fitting curves using the eq. 3–1 with the following parameters: PDDA/TiO$_x$ LbL films; film thickness d = 180 nm, V_{BI} = 0 V, r_s = 10 Ω, $\mu_e = 7 \times 10^{-5}$ cm^2 V^{-1} s^{-1} and np-TiO$_2$ film; d = 160 nm, V_{BI} = 0 V, r_s = 10 Ω, $\mu_e = 2 \times 10^{-4}$ cm^2 V^{-1} s^{-1} at ε_r = 24.

To prove the presence of the electron-transporting networks, the author evaluated the electron mobility μ_e of PDDA/TiO$_x$ LbL films. Figure 3–8 shows semi-logarithmic plots of J–V characteristics of PDDA/TiO$_x$ LbL films (circles) and a np-TiO$_2$ film (squares) against $V - V_{BI} - V_{RS}$. The solid lines represent fitting curves for the J–V characteristics by using eq. 3–1. The dielectric constant ε_r of PDDA/TiO$_x$ LbL films was estimated to be 30 considering the volume fraction of TiO$_x$ in the LbL film (0.65). The dielectric constant ε_r of the np-TiO$_2$ film was set to be 34 considering the volume fraction of TiO$_2$ in the np-TiO$_2$ film (0.74) estimated from the assumption of the closest packing. As a result, the electron mobility μ_e of the PDDA/TiO$_x$ LbL film was evaluated to be 6×10^{-5} cm^2 V^{-1} s^{-1}, which is comparable to 2×10^{-4} cm^2 V^{-1} s^{-1} evaluated for the np-TiO$_2$ film. The high electron mobility shows that there are effective percolating networks of TiO$_x$ in the film. This is mainly due to the high volume fraction of TiO$_x$ as mentioned above and also due to the interpenetrating characteristics of LbL films as reported previously.[25] Table 3–1 summarizes σ and μ_e of the PDDA/TiO$_x$ LbL films and the np-TiO$_2$ film. The author therefore concludes that the PDDA/TiO$_x$ LbL films converted from TALH can serve as an efficient electron-transporting material.

Table 3–1. The conductivity σ and the electron mobility μ_e of TiO$_x$-based LbL films and a np-TiO$_2$ film.

Structures	Annealing temperature / °C	σ / S cm^{-1}	μ_e / cm^2 V^{-1} s^{-1}
TiO$_x$ LbL	95	$2.6 \pm 0.3 \times 10^{-9}$	6×10^{-5}
np-TiO$_2$	150	$2.1 \pm 0.2 \times 10^{-7}$	2×10^{-4}

3.3.4. ***Photovoltaic Performance***

Finally, the author demonstrates the application of TiO_x LbL films to photovoltaic cells. Figure 3–9 shows *J–V* characteristics of photovoltaic cells of ITO|$(PDDA/TiO_x)_6$|$(PPV/PSS)_5$/PPV|PEDOT:PSS|Au (TiO_x LbL-based cells, solid line) and of ITO|d-TiO_2|$(PPV/PSS)_5$/PPV|PEDOT:PSS|Au (d-TiO_2-based cells, broken line) under AM1.5G-simulated solar illumination at 100 mW cm^{-2}. Device performance of TiO_x LbL-based cells was as follows: the short-circuit current density J_{SC} = 0.14 mA cm^{-2}, the open-circuit voltage V_{OC} = 0.77 V, the fill factor FF = 0.27, and the power conversion efficiency PCE = 0.03 %. On the other hand, device performance of d-TiO_2-based cells was as follows: J_{SC} = 0.08 mA cm^{-2}, V_{OC} = 0.60 V, FF = 0.17, and PCE = 0.01%. In other words, TiO_x LbL-based cells exhibited higher performance in all device parameters than those of d-TiO_2-based cells. Figure 3–10 shows external quantum efficiency (EQE) of the two photovoltaic cells. Both cells should have the same absorption efficiency because of the same thickness of PPV LbL film. Thus, the larger EQE of TiO_x LbL-based cells suggests that the interfacial area would be larger in TiO_x LbL-based cells than in d-TiO_2-based cells. As shown in Figure 3–5, the PDDA/TiO_x LbL film was pin-hole free but had a surface roughness of <10 nm. This is probably due to TiO_x nanoparticles being as small as 6 nm. Considering the particle size of TiO_x, the surface area of TiO_x LbL films is roughly estimated to be 1.5 times compared to that of d-TiO_2 films. The author therefore attributes the increase in J_{SC} to the larger interface area in TiO_x LbL films. The interpenetration between TiO_x and PPV layers at the interface also contributes to the increase in J_{SC}. Thus, the author concludes that the TiO_x LbL film can be employed as an effective electron-transporting layer and an acceptor layer in photovoltaic cells.

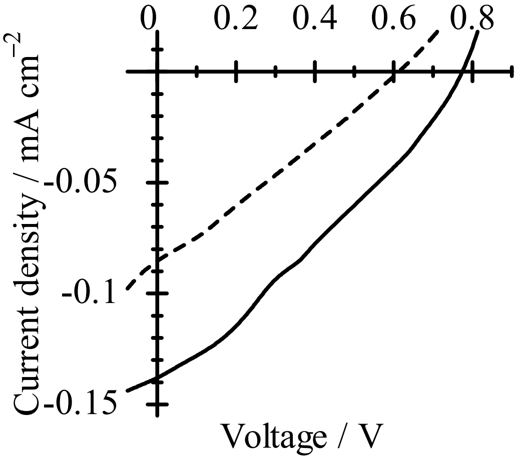

Figure 3–9. *J–V* characteristics of photovoltaic cells with layered structures of ITO|(PDDA/TALH)$_6$ (40 nm)|(PPV/PSS)$_5$/PPV (12 nm)|PEDOT:PSS (80 nm)|Au (solid line) and ITO|d-TiO$_2$ (60 nm)|(PPV/PSS)$_5$/PPV (12 nm)|PEDOT:PSS (80 nm)|Au (broken line).

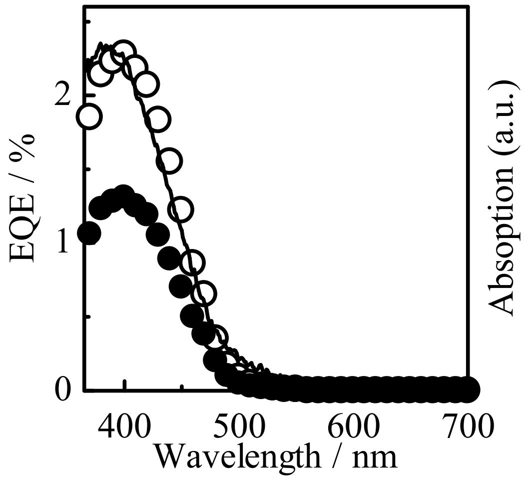

Figure 3–10. EQE spectra of photovoltaic cells of ITO|(PDDA/TALH)$_6$ (40 nm)|(PPV/PSS)$_5$/PPV (12 nm)|PEDOT:PSS (80 nm)|Au (open circles) and ITO|d-TiO$_2$ (60 nm)|(PPV/PSS)$_5$/PPV (12 nm)|PEDOT:PSS (80 nm)|Au (closed circles). The solid line depicts the absorption spectrum of a PPV LbL film annealed at 100 °C 2 h.

3.4. Conclusions

The author fabricated titania-based ultrathin films by the LbL assembly of TALH and PDDA or PPV where TALH was completely converted into TiO_x in the LbL films by thermal annealing at 95 °C for 24 h. The thickness of ultrathin films was successfully controlled by the LbL deposition on a scale of nanometers. From the absorption and AFM measurements, the monolayer thickness of each layer was estimated to be 2.2 nm for PDDA and 4 nm for TiO_x in PDDA/TiO_x LbL films and 0.9 nm for PPV and 4.8 nm for TiO_x in PPV/TiO_x LbL films. Consequently, the volume fraction was as high as ~65% for PDDA/TiO_x LbL films and ~85% for PPV/TiO_x LbL films. The monolayer thickness of TiO_x (4–5 nm) is consistent with the particle size (~6 nm) of TALH in water evaluated by the dynamic light scattering measurement. The author therefore concludes that TALH is stably dispersed in water as monodisperse nanoparticles with a diameter of ~6 nm and quantitatively adsorbed on a substrate during the LbL deposition. The conductivity σ of PDDA/TiO_x LbL films was 1–3 $\times 10^{-9}$ S cm^{-1} at annealing temperatures below 150 °C, increased steeply above 180 °C, and then reached 4×10^{-8} S cm^{-1} at 220 °C, which is indicative of semiconductors. The electron mobility μ_e of PDDA/TiO_x LbL film was evaluated to be 6×10^{-5} cm^2 V^{-1} s^{-1}, which is comparable to that of a np-TiO_2 film. The author therefore concludes that there exist effective percolating networks of TiO_x in the direction normal to the substrate in the LbL films. This is mainly due to the high volume fraction of TiO_x in the film. Furthermore, the author demonstrated planar heterojunction photovoltaic cells with PPV-based LbL films as an electron-donating layer and TiO_x-based LbL films as an electron-accepting layer. The photovoltaic cells exhibited a higher device performance than the reference cells with a d-TiO_2 layer because of the larger interface area due to TiO_x nanoparticles. The author thus concludes that the TiO_x-base LbL films reported in this chapter can serve not only as an electron-transporting but also as an electron-accepting material.

References

(1) Chen, X.; Mao, S. S. *Chem. Rev.* **2007**, *107*, 2891–2959.

(2) Mor, G. K.; Varghese, O. K.; Paulose, M.; Shankar, K.; Grimes, C. A. *Sol. Energy Mater. Sol. Cells* **2006**, *90*, 2011–2075.

(3) Martinu, L.; Poitras, D. *J. Vac. Sci. Technol., A* **2000**, *18*, 2619–2645.

(4) Kalyanasundaram, K.; Grätzel, M. *Coord. Chem. Rev.* **1998**, *77*, 347–414.

(5) Wu, J.-M.; Shih, H. C.; Wu, W.-T.; Tseng, Y.-K.; Chen, I-C. *J. Cryst. Growth* **2005**, *281*, 384–390.

(6) Wang, C.-C.; Ying, J. Y. *Chem. Mater.* **1999**, *11*, 3113–3120.

(7) Watanabe, T.; Fukayama, S.; Miyauchi, M.; Fujishima, A.; Hashimoto, K. *J. Sol-Gel Sci. Technol.* **2000**, *19*, 71–76.

(8) Li, Y.; Kunitake, T.; Fujikawa, S. *J. Phys. Chem. B* **2006**, *110*, 13000–13004.

(9) Schubert, U. *J. Mater. Chem.* **2005**, *15*, 3701–3715.

(10) Möckel, H.; Giersig, M.; Willig, F. *J. Mater. Chem.* **1999**, *9*, 3051–3056.

(11) Mayya, K. S.; Gittins, D. I.; Caruso, F. *Chem. Mater.* **2001**, *13*, 3833–3836.

(12) Yu, A.; Lu, G. Q. M.; Drennan, J.; Gentle, I. R. *Adv. Funct. Mater.* **2007**, *17*, 2600–2605.

(13) Wang, Z.; Ergang, N. S.; Al-Daous, M. A.; Stein, A. *Chem. Mater.* **2005**, *17*, 6805–6813.

(14) Dionigi, C.; Greco, P.; Ruani, G.; Cavallini, M.; Borgatti, F.; Biscarini, F. *Chem. Mater.* **2008**, *20*, 7130–7135.

(15) Decher, G. *Science* **1997**, *277*, 1232–1237.

(16) Ariga, K.; Hill, J. P.; Ji, Q. *Phys. Chem. Chem. Phys.* **2007**, *9*, 2319–2340.

(17) Hammond, P. T. *Adv. Mater.* **2004**, *16*, 1271–1293.

(18) Caruso, F. *Adv. Mater.* **2001**, *13*, 11–22.

(19) Shi, X.; Cassagneau, T.; Caruso, F. *Langmuir* **2002**, *18*, 904–910.

(20) Kim, J.-H.; Fujita, S.; Shiratori, S. *Thin Solid Films* **2006**, *499*, 83–89.

(21) Kim, J.-H.; Fujita, S.; Shiratori, S. *Colloids Surf., A* **2006**, *284–285*, 290–294.

(22) O'Regan, B.; Grätzel, M. *Nature* **1991**, *353*, 737–740.

(23) Ravirajan, P.; Haque, S. A.; Durrant, J. R.; Bradley, D. D. C.; Nelson, J. *Adv. Funct. Mater.* **2005**, *15*, 609–618.

(24) Ogawa, M.; Kudo, N.; Ohkita, H.; Ito, S.; Benten, H. *Appl. Phys. Lett.* **2007**, *90*, 223107.

(25) Wakizaka, D.; Fushimi, T.; Ohkita, H.; Ito, S. *Polymer* **2004**, *45*, 8561–8565.

(26) Grant, C. D.; Schwartzberg, A. M.; Smestad, G. P.; Kowalik, J.; Tolbert, L. M.; Zhang, J. Z. *Synth. Met.* **2003**, *132*, 197–204.

(27) O'Hayre, R.; Nanu, M.; Schoonman, J.; Goossens, A. *J. Phys. Chem. C* **2007**, *111*, 4809–4814.

(28) Asmatulu, R.; Geist, B.; Spillman, W. B. Jr; Claus, R. O. *Smart Mater. Struct.* **2005**, *14*, 1493–1500.

(29) Tuladhar, S. M.; Poplavskyy, D.; Choulis, S. A.; Durrant, J. R.; Bradley, D. D. C.; Nelson, J. *Adv. Funct. Mater.* **2005**, *15*, 1171–1182.

(30) Hanprasopwattana, A.; Rieker, T.; Sault, A. G.; Datye, A. K. *Catal. Lett.* **1997**, *45*, 165–175.

(31) Laugel, N.; Hemmerlé, J.; Ladhari, N.; Arntz, Y.; Gonthier, E.; Haikel, Y.; Voegel, J.-C.; Schaaf, P.; Ball, V. *J. Colloid Interface Sci.* **2008**, *324*, 127–133.

(32) Benten, H.; Ogawa, M.; Ohkita, H.; Ito, S. *Adv. Funct. Mater.* **2008**, *18*, 1563–1572.

(33) Huang, P. C.; Reichert, K.-H. *Angew. Makromol. Chem.* **1989**, *165*, 1–7.

Part II

Chapter 4

Exciton Generation and Diffusion in Multilayered Organic Solar Cells Designed by Layer-by-Layer Assembly of Poly(*p*-phenylenevinylene)

4.1. Introduction

Bulk heterojunction polymer-based solar cells and planar heterojunction small molecule-based solar cells are representatives of organic thin-film solar cells.[1] The power conversion efficiency has been reported to be around 5–8%.[2–5] The former solar cells are typically fabricated by solution processes such as spincoating of a blend solution of a conjugated polymer and a fullerene derivative,[6] and therefore have attracted much attention because of the suitability for high-throughput production based on the printing and coating techniques.[7] On the other hand, the latter solar cells are typically fabricated by vacuum deposition of small molecules such as copper phthalocyanine and fullerene.[4,5,8] One of the most remarkable advantages for such devices is that layered structures are precisely designed and controlled on a scale of subnanometers by the vacuum deposition technique.[9] Such a precisely controlled device structure is beneficial not only for developing high-performance solar cells[4] but also for understanding a series of fundamental processes such as exciton generation, exciton diffusion, charge generation, and charge collection at the electrodes.[8,10] The photon absorption efficiency in well-ordered multilayered devices can be estimated by optical simulations considering optical interference effects.[8] The efficiency of exciton diffusion to a donor/acceptor interface can be evaluated from photoluminescence (PL) quenching experiments using the one-dimensional diffusion model.[8,11,12] A series of device analyses have been reported for small molecule thin-film solar cells fabricated by the vacuum deposition,[8] and provide a clear guideline for designing more efficient solar cells.

To integrate both advantages of the solution processing and the vacuum deposition technique, the author has developed multilayered organic thin-film solar cells fabricated by a combination of the spincoating and layer-by-layer (LbL) deposition techniques. This technique, which has been developed by Decher et al.,[13] is a simple and versatile method for fabricating ultrathin films,[14] and is therefore applied to various ultrathin-film-coated materials[15] such as core-shell nanoparticles,[16] two- or three-dimensional patterned structures[17] with a precisely controlled thickness on a scale of nanometers. Ultrathin films of poly(*p*-phenylenevinylene) (PPV) have been fabricated by the LbL deposition technique using a precursor of PPV[18] and then applied to organic thin-film solar cells.[19] The author has previously designed the configuration of the light-harvesting layer in multilayered organic thin-film solar cells.[11,20–23] As a result of such structural optimization, the best-performance device was obtained with a power conversion efficiency of 0.26% under AM1.5G solar simulated illumination. This efficiency is significantly higher than that reported for LbL-based organic solar cells.[24–26] In this chapter, the author discusses the relationship between the device efficiency and the device structure of LbL-based multilayered solar cells. The exciton generation in the LbL layer is estimated by the optical simulation. The exciton diffusion into a donor/acceptor interface is evaluated from the PL quenching experiments using the one-dimensional diffusion model. The author demonstrates that the device performance can be quantitatively analyzed on the basis of a layered structure.

4.2. Experimental Section

4.2.1. *Materials*

Poly(*p*-xylene tetrahydrothiophenium chloride) (pre-PPV: Aldrich, 0.25 wt% aqueous solution) was diluted to 1 mM with ultrapure water. The solution was adjusted to pH 8–9 with NaOH aqueous solution. The 1 mM pre-PPV aqueous solution was used as a cationic polyelectrolyte solution for the LbL deposition. Poly(sodium 4-styrenesulfonate) (PSS: Aldrich, M_w = 70,000 g mol^{-1}) was dissolved in ultrapure water to give 10 mM PSS aqueous solution, which was used as an anionic polyelectrolyte solution for the LbL deposition. Poly(3,4-ethylenedioxythiophene):poly(4-styrenesulfonate) (PEDOT:PSS: Aldrich, 1.3 wt% dispersion in water, conductive grade) was mixed with ethylene glycol (EG: Aldrich, anhydrous, 99.8%) (PEDOT:PSS/EG = 100/20 by weight). The mixed solution of PEDOT:PSS with EG was used for fabrication of a hole-transporting layer by spincoating. Polystyrene (PS: Alrdich, M_w = 280,000 g mol^{-1}) was purified by reprecipitation from a toluene solution into methanol three times. To 2 mL of *o*-dichlorobenzene (Aldrich) was added 12 mg of PS and 48 mg of C_{60} (Frontier Carbon Co. Ltd.). The blend solution of PS and C_{60} was used for fabrication of an electron-transporting layer by spincoating. Figure 4–1 shows the chemical structures of materials used in this chapter.

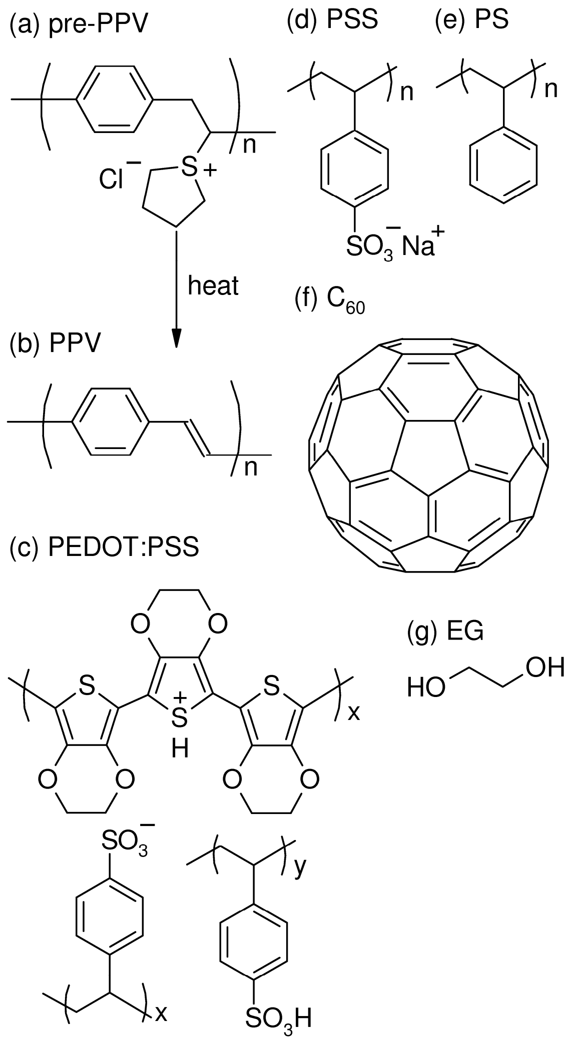

Figure 4–1. Chemical structures of materials used in this chapter.

4.2.2. *Device Fabrication*

Indium-tin-oxide (ITO) coated glass substrates (10 Ω per square) were washed by ultrasonication in toluene, acetone, and ethanol for 15 min, respectively, and then dried with a N_2 flow. These pre-washed substrates were further treated with a UV–O_3 cleaner for 1 h. First, a hole-transporting layer of PEDOT:PSS was prepared by spincoating from the aqueous solution of PEDOT:PSS mixed with EG, and was thermally annealed at 70 °C for 14 h in air and at 140 °C for 1 h under vacuum to give an insoluble film as reported previously.[21] The thickness of the PEDOT:PSS layer was ~80 nm. Second, a light-harvesting layer was prepared by the LbL deposition of pre-PPV and PSS. The PEDOT:PSS-coated substrate was immersed in the 1 mM pre-PPV aqueous solution for 5 min, rinsed in ultrapure water for 3 min, immersed in the 10 mM PSS aqueous solution for 5 min, and rinsed in ultrapure water for 3 min. This cycle gives one bilayer of pre-PPV and PSS, which is abbreviated as (pre-PPV/PSS)$_1$. Each LbL film was completely dried under a flow of air for 4–6 min after the immersion. Third, an electron-transporting layer was prepared on (n + 0.5) bilayers of pre-PPV/PSS, which is abbreviated as (pre-PPV/PSS)$_n$/pre-PPV, by spincoating from the *o*-chlorobenzene solution of C_{60} and PS. Subsequently, the (pre-PPV/PSS)$_n$/pre-PPV LbL layer was thermally converted to the (PPV/PSS)$_n$/PPV LbL layer by annealing at 100 °C for 2 h under vacuum. Finally, Al was thermally deposited as a counter electrode at 2.5×10^{-6} Torr on top of the triple-layered film through a metal mask to give an active area of 6 mm^2 (2 × 3 mm^2). The triple-layered device consists of a hole-transporting layer of the PEDOT:PSS film, a light-harvesting layer of the PPV/PSS LbL film, and an electron-transporting layer of the C_{60}:PS film. The device structure is abbreviated as ITO|PEDOT:PSS|(PPV/PSS)$_n$/PPV|C_{60}:PS|Al. The thickness of the (PPV/PSS)$_n$/PPV light-harvesting layer was varied between 3 nm and 19 nm depending on the number of the deposition cycles n. The detailed structural analysis of the device has been described in Ref 21. The thickness of the C_{60}:PS electron-transporting layer was varied between 20 nm and 50 nm by adjusting the spin rate.

4.2.3. *Sample Preparation for the Quenching Experiment*

Quartz substrates were washed by ultrasonication in toluene, acetone, and ethanol for 15 min, respectively, and then dried with a N_2 flow. These pre-washed substrates were further treated with a UV–O_3 cleaner for 1 h. An emission layer of (pre-PPV/PSS)$_n$/pre-PPV was prepared on a quartz substrate by the same fabrication procedures described above. Before the thermal conversion of pre-PPV into PPV, a quenching layer was prepared on the (pre-PPV/PSS)$_n$/pre-PPV layer mentioned above by spincoating from the *o*-chlorobenzene solution of C_{60} and PS. As a control, a PS layer was prepared on the (pre-PPV/PSS)$_n$/pre-PPV layer by spincoating from the *o*-chlorobenzene solution of PS. Finally, the (pre-PPV/PSS)$_n$/pre-PPV LbL layer was thermally converted to the (PPV/PSS)$_n$/PPV LbL layer by annealing at 100 °C for 2 h under vacuum. The schematic layered structures of the PPV/PSS LbL films are shown in Figure 4–2 and the detailed characterization of the layered structures including each layer thickness is described in the appendix section.

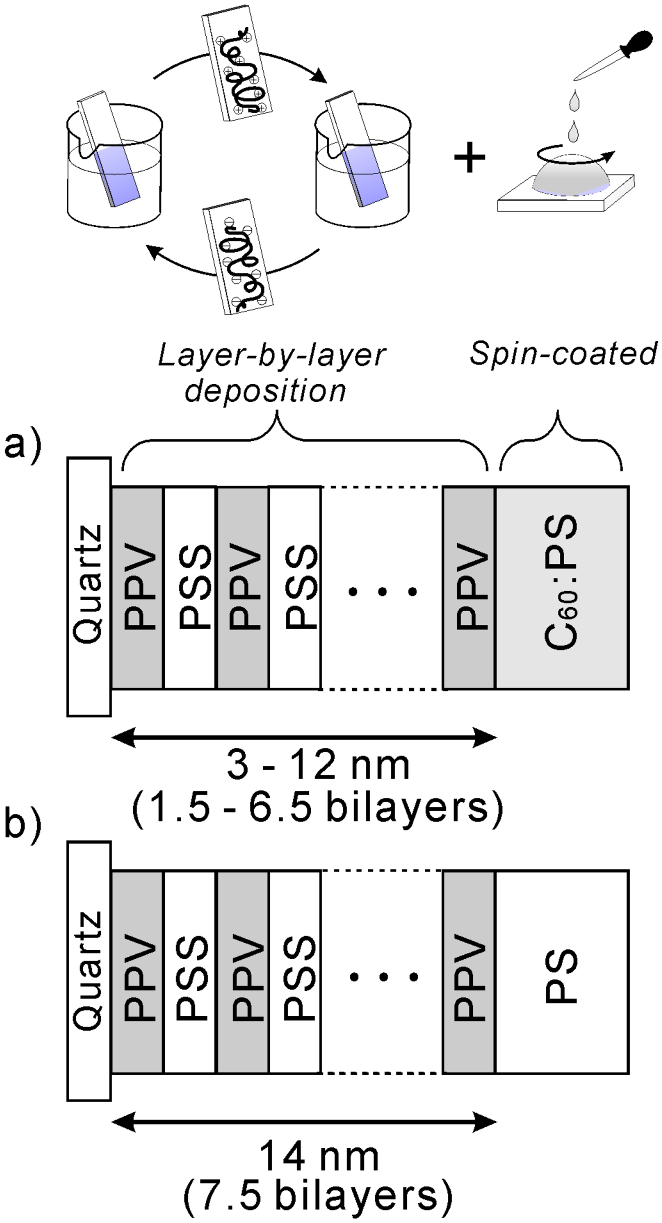

Figure 4–2. Schematic layered structures of the double-layered films employed for the quenching measurements. a) (PPV/PSS)$_n$/PPV|C_{60}:PS, b) (PPV/PSS)$_n$/PPV|PS. The monolayer thickness in (PPV/PSS)$_n$/PPV was 0.9 nm for PPV and 1.0 nm for PSS.

4.2.4. *Measurements*

The current density–voltage (*J–V*) characteristics of the triple-layered devices of ITO|PEDOT:PSS|(PPV/PSS)$_n$/PPV|C$_{60}$:PS|Al were measured with a DC voltage current source/monitor (Advantest, R6243) in the dark and under AM1.5G-simulated solar illumination at 100 mW cm^{-2}. The external quantum efficiency (EQE) was measured with a digital electrometer (Advantest, R8252) under monochromatic light illumination at 420 nm from a 500-W Xe lamp (Thermo Oriel, Model 66921) with optical cut-filters and a monochromator (Thermo Oriel, UV–visible Conerstone). Fluorescence spectra of the double-layered films of (PPV/PSS)$_n$/PPV|C$_{60}$:PS and (PPV/PSS)$_n$/PPV|PS on quartz substrates were measured with a fluorescence spectrometer (Hitachi, F-4500). The excitation wavelength was 420 nm. The fluorescence decay of the double-layered films was measured by the time-correlated single-photon-counting method as described elsewhere.[27,28] The excitation wavelength was 440 nm. All these measurements were performed in air at room temperature.

4.2.5. *Optical Simulation*

The photon absorption efficiency of the PPV/PSS LbL layer is evaluated by the transfer matrix method.[8,29] For simplicity, the author assumes that each layer j ($j = 1, 2, ..., m$) consists of homogenous and isotropic materials with a thickness L_j and a complex refractive index $\boldsymbol{n}_j = n_j + ik_j$. Furthermore, the interfaces are assumed to be optically flat even in the PPV/PSS LbL layer although there is a little interpenetration between neighboring LbL layers. The optical electric field amplitude $\boldsymbol{E}_j(x)$ is calculated as a function of position in the multilayer structure in the thin film where x is the position in layer j; $0 \leq x \leq L_j$. The detailed calculation of $\boldsymbol{E}_j(x)$ are described in the appendix section. Here, $|\boldsymbol{E}_j(x)|^2$ is normalized by $|\boldsymbol{E}_0|^2$ where $\boldsymbol{E}_0$ is the optical electric field amplitude of the incident plane wave. The time average of the energy dissipated per second at position x in layer j $Q_j(x)$ is then

$$Q_j(x) = \frac{1}{2} c \varepsilon_0 \alpha_j n_j \left| \boldsymbol{E}_j(x) \right|^2 \tag{4–1}$$

where c is the speed of light, ε_0 is the permittivity of free space, and α_j is the absorption coefficient of layer j. The exciton generation rate at position x in layer j is therefore given by $G_j(x) = (\lambda/hc)\,Q_j(x)$ where λ is the wavelength of the incident light, h is the Planck's constant. Consequently, the absorption efficiency of the PPV/PSS LbL layer is given by

$$\eta_{\mathrm{A}}^{\mathrm{LbL}} = \sum_j^{\mathrm{LbL}} \int_0^{L_j} G_j(x)\,\mathrm{d}x \tag{4–2}$$

In the same way, the absorption efficiency of the C_{60}:PS layer $\eta_{\mathrm{A}}{}^{\mathrm{C60}}$ is also evaluated. Table 4–1 summarizes the optical parameters[30–35] and thickness for each component employed for the calculation by the transfer matrix.

Table 4–1. Optical parameters and thickness of each component at 420 nm employed for the calculation by the transfer matrix.

Component	n	k	Thickness / nm	Reference
glass	1.53	0	1.0×10^6	(30)
ITO	1.94	0.01	200	(31)
PEDOT:PSS	1.42	0.02	80	(31)
PPV	2.10	1.10	3–19	(32)
PSS	1.51	0		(33)
C_{60}:PS	2.05	0.20	20–50	(34)
Al	0.59	4.30	50	(35)

4.3. Results

4.3.1. *Photocurrent Generation*

To examine the relationship between the photocurrent generation and the device structure, the author fabricated various triple-layered polymer solar cells of ITO|PEDOT:PSS|$(PPV/PSS)_n$/PPV|C_{60}:PS|Al with different layer thicknesses. The thickness of the PPV/PSS LbL layer was varied between 3 nm and 19 nm and the thickness of C_{60}:PS layer was varied between 20 nm and 50 nm. Figure 4–3a shows the dependence of short-circuit current density J_{SC} and EQE of the solar cell on the thickness of the PPV/PSS LbL film. Note that the thickness of the C_{60}:PS layer was fixed at 30 nm. With increasing thickness of the PPV/PSS LbL film, as shown by the open circles in the figure, J_{SC} increased steeply by a factor of two from 3 to 7 nm, reached the maximum at around 7 nm, and then gradually decreased above it. As shown in the figure, EQE at 420 nm also showed the same tendency as J_{SC}. This trend is consistent with the previous report.[21] The increase in J_{SC} below 7 nm is simply ascribed to the increase in the light-harvesting PPV/PSS LbL layer, which increases the photon absorption efficiency η_A leading to the exciton generation. To explain the gradual decrease in J_{SC} above 7 nm, however, the author should consider other limiting factors such as the efficiency of exciton diffusion to a donor/acceptor interface η_{ED} as discuss later. On the other hand, Figure 4–3b shows the dependence of J_{SC} of the solar cell on the thickness of the C_{60}:PS film. Note that the thickness of the PPV/PSS LbL layer was fixed at 7 nm. As shown by the open circles in the figure, J_{SC} increased with the increase in the thickness of the C_{60}:PS film, decreased above 30 nm, and reduced by half at 50 nm even though the thickness of the light-harvesting PPV/PSS LbL layer was kept constant. Thus, as described below, the optical interference effect should be taken into account in the photon absorption efficiency η_A in the device with reflective metal mirror as an electrode.

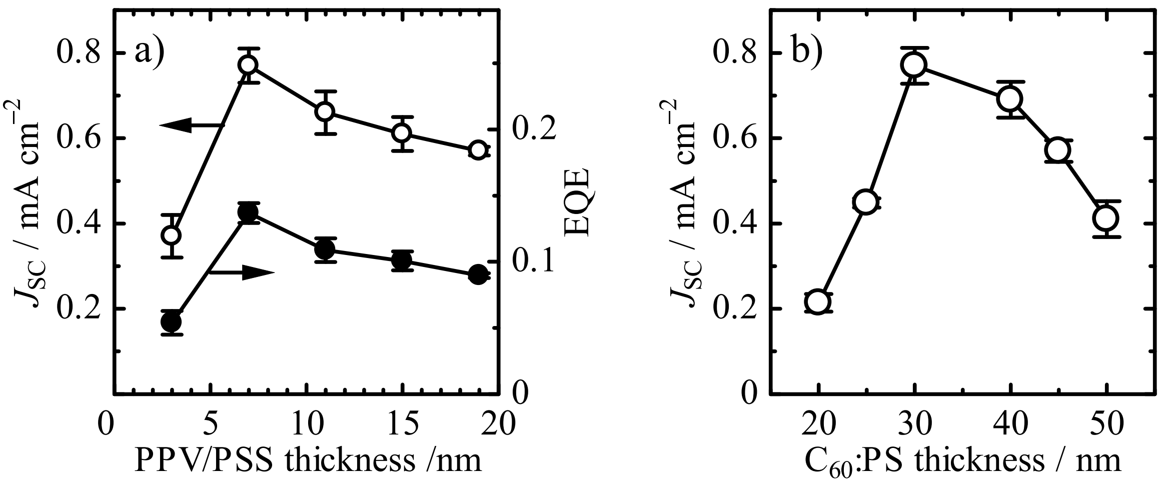

Figure 4–3. a) Dependence of J_{SC} (open circles) and EQE at 420 nm (closed circles) on the thickness of the (PPV/PSS)$_n$/PPV layer measured for triple-layered devices of ITO|PEDOT:PSS|(PPV/PSS)$_n$/PPV(3–19 nm)|C_{60}:PS(30 nm)|Al, under AM1.5G solar simulated illumination at 100 mW cm^{-1}. b) Dependence of J_{SC} on the thickness of the C_{60}:PS layer measured for triple-layered devices of ITO|PEDOT:PSS|(PPV/PSS)$_n$/PPV(7 nm)|C_{60}:PS(20–50 nm)|Al, under AM1.5G solar simulated illumination at 100 mW cm^{-1}. The experimental error in EQE was as small as 5 % and the error bars were within the closed circles.

4.3.2. *Optical Simulation*

To evaluate the photon absorption efficiency η_A, the author calculates the internal optical electric field $\boldsymbol{E}(x)$ and the exciton generation rate $G(x)$ as a function of the position x in the multilayered organic solar cells by the transfer matrix method. Figure 4–4a shows the optical intensity $|\boldsymbol{E}(x)|^2$ in multilayered organic solar cells with the PPV/PSS LbL layer differing in thickness: the device structure is ITO(200 nm)|PEDOT:PSS(80 nm)|(PPV/PSS)$_n$/PPV(3–19 nm)|C_{60}:PS(30 nm)|Al. As the thickness of the PPV/PSS LbL layer increases, the peak value of $|\boldsymbol{E}(x)|^2$ decreases monotonically but the peak position is almost unchanged. The decrease in $|\boldsymbol{E}(x)|^2$ is mainly due to the absorption of the PPV/PSS LbL layer although there should be optical interference effects as is discussed later. As a result, as shown in Figure 4–4b, $G(x)$ in the PPV/PSS LbL layer also decreases monotonically with the increase in the thickness of the PPV/PSS LbL layer. Note that the values of $G(x)$ are much larger than that in the C_{60}:PS layer, suggesting that the PPV/PSS LbL layer has a crucial role in the light harvesting of the device.

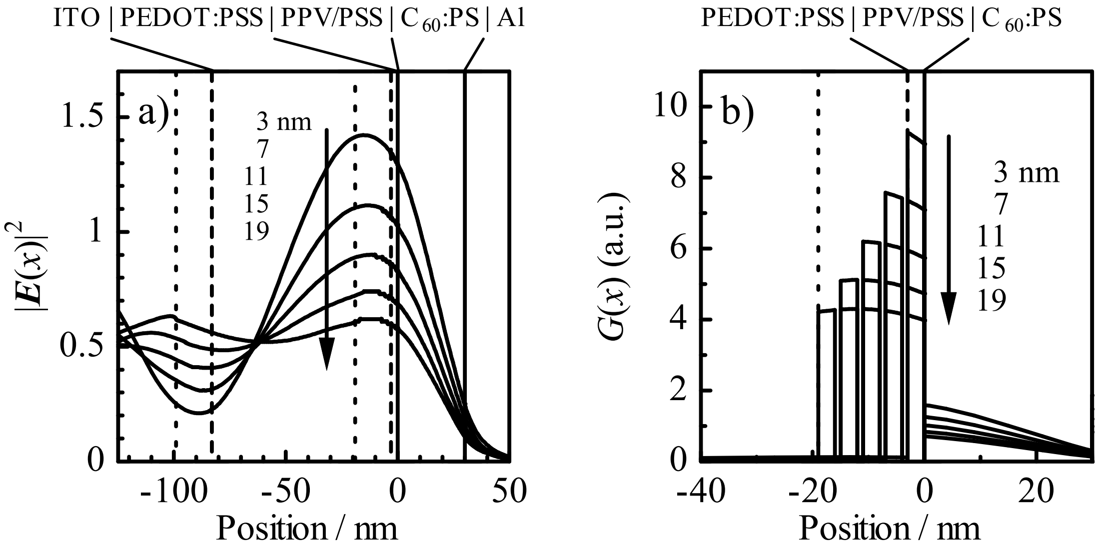

Figure 4–4. a) Calculated distribution of the optical intensity $|\boldsymbol{E}(x)|^2$, which is normalized by the optical intensity of the incident plane wave. b) Calculated distribution of the exciton generation rate $G(x)$. The device structure employed for the calculation is ITO(200 nm)|PEDOT:PSS(80 nm)|(PPV/PSS)$_n$/PPV(3–19 nm)|C_{60}:PS(30 nm)|Al.

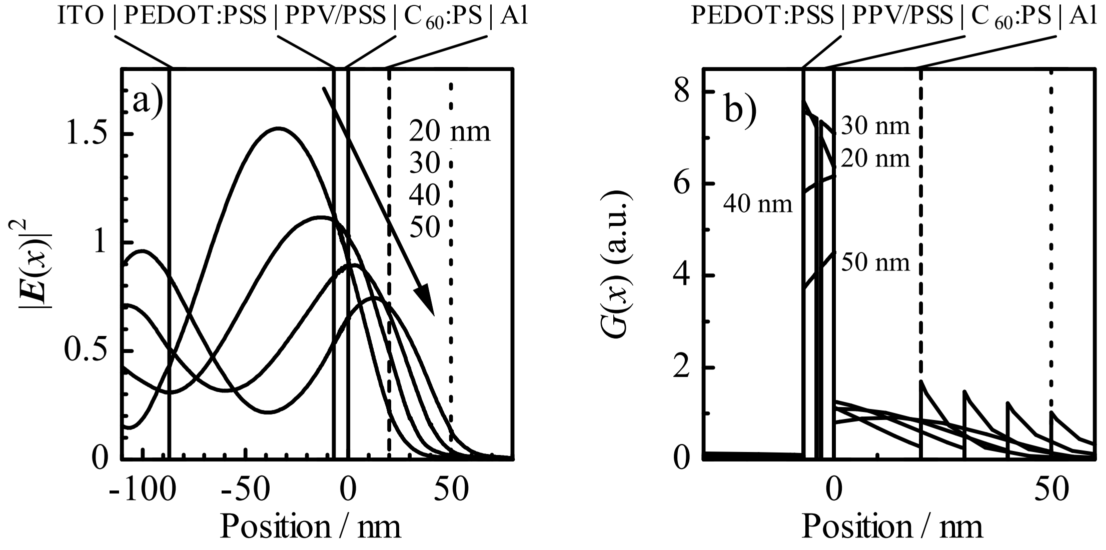

Figure 4–5. a) Calculated distribution of the optical intensity $|\boldsymbol{E}(x)|^2$, which is normalized by the optical intensity of the incident plane wave. b) Calculated distribution of the exciton generation rate $G(x)$. The device structure employed for the calculation is ITO(200 nm)|PEDOT:PSS(80 nm)|(PPV/PSS)$_n$/PPV(7 nm)|C_{60}:PS(20–50 nm)|Al.

Figure 4–5a shows the optical intensity $|\boldsymbol{E}(x)|^2$ in multilayered organic solar cells with a C_{60}:PS layer differing in thickness: the device structure is ITO(200 nm)|PEDOT:PSS(80 nm)|(PPV/PSS)$_n$/PPV(7 nm)|C_{60}:PS(20–50 nm)|Al. As is the case with the PPV/PSS LbL layer, the peak value of $|\boldsymbol{E}(x)|^2$ in the PPV/PSS LbL layer decreases monotonically with the increase in the thickness of the C_{60}:PS layer. This decrease in $|\boldsymbol{E}(x)|^2$ is mainly due to the absorption of the C_{60}:PS layer. In contrast to Figure 4–4a, the peak position is significantly shifted from the PEDOT:PSS layer through the PPV/PSS LbL layer to the C_{60}:PS layer, suggesting that the C_{60}:PS layer serves as an optical spacer as is discussed later. As a result, as shown in Figure 4–5b, the dependence of $G(x)$ on the thickness of the C_{60}:PS layer is a bit more complex. The average values of $G(x)$ in the PPV/PSS LbL layer increase slightly from

20 to 30 nm and then decrease above 30 nm with the increase in the thickness of the C_{60}:PS LbL layer.

On the basis of these calculations, the author evaluates the photon absorption efficiency in the PPV/PSS LbL layer $\eta_A{}^{LbL}$ at 420 nm. As the thickness of the PPV/PSS LbL layer increases, as shown by the open squares in Figure 4–6a, $\eta_A{}^{LbL}$ monotonically increases up to around 20 nm and then is almost saturated above 20 nm. The open circles represent the absorption of the PPV/PSS LbL layer simply calculated from the absorbance of the film. The closed circles represent the absorption of the PPV/PSS LbL layer calculated from twice the absorbance of the film considering the reflection at the Al electrode. Note that the absorption of other layers such as ITO, PEDOT:PSS, and C_{60}:PS layers is also taken into account in the calculation. In other words, this is the maximum absorption without consideration of optical interference effects. Thus, the difference between the open squares $\eta_A{}^{LbL}$ and the closed circles clearly demonstrates that the optical interference effects have a great impact on the photon absorption efficiency in multilayered devices. The author notes that the thickness dependence of $\eta_A{}^{LbL}$ is not consistent with that of J_{SC} shown in Figure 4–3a. This disagreement suggests that there are other limiting factors for the charge generation as is discussed later. As the thickness of the C_{60}:PS LbL layer increases, on the other hand, $\eta_A{}^{LbL}$ slightly increases from 20 to 30 nm and then decreases above 30 nm while $\eta_A{}^{C60}$ increases monotonically as shown in Figure 4–6b. The thickness dependence of J_{SC} shown in Figure 4–3b is in good agreement with that of $\eta_A{}^{LbL}$ rather than $\eta_A{}^{C60}$, suggesting that the contribution of the C_{60}:PS layer to the photocurrent generation is negligibly minor and the PPV/PSS LbL layer has a major role in the light harvesting. Therefore, the author focuses the attention on the charge generation from excitons generated in the PPV/PSS LbL layer in this chapter.

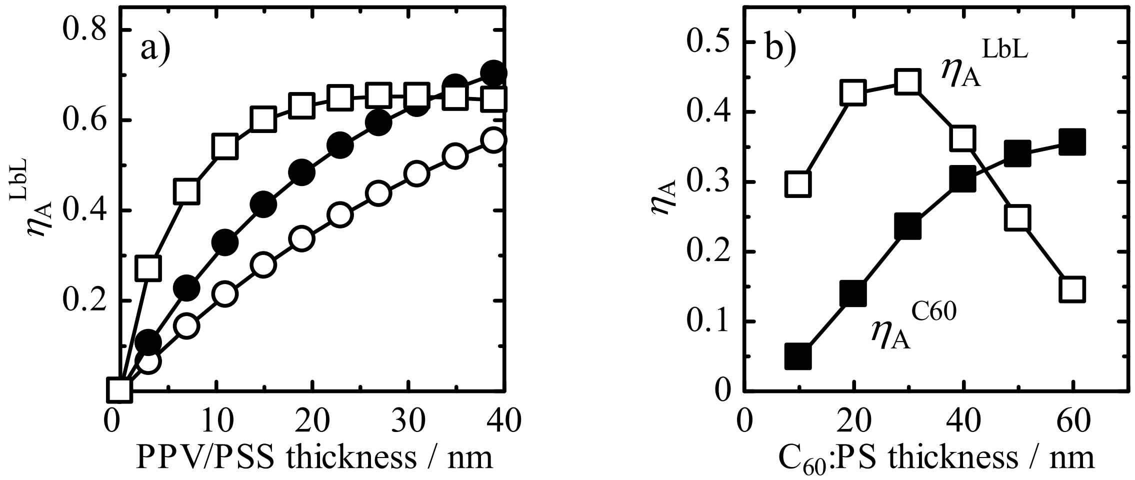

Figure 4–6. Photon absorption efficiency η_A^{LbL} in the PPV/PSS LbL layer at 420 nm (open squares) plotted against the thickness of a) the PPV/PSS LbL layer and b) the C_{60}:PS layer. The device structures are as follows: a) ITO(200 nm)|PEDOT:PSS(80 nm)|(PPV/PSS)$_n$/PPV(0–39 nm)|C_{60}:PS(30 nm)|Al and b) ITO(200 nm)|PEDOT:PSS(80 nm)|(PPV/PSS)$_n$/PPV(7 nm)|C_{60}:PS(10–60 nm)|Al. The open circles represent the absorption of the PPV/PSS LbL layer calculated from the absorbance of the film. The closed circles represent the absorption of the PPV/PSS LbL layer calculated from twice the absorbance of the film considering the reflection at the Al electrode. The closed squares represent the photon absorption efficiency η_A^{C60} in the C_{60}:PS layer at 420 nm. Note that the absorption of other layers such as ITO, PEDOT:PSS, and C_{60}:PS layers is also taken into account in the calculation.

4.3.3. *Exciton Quenching*

As mentioned before, the author cannot explain the dependence of J_{SC} on the thickness of the PPV/PSS LbL layer in terms of the photon absorption efficiency of the LbL layer η_A^{LbL} alone. This is partly because some excitons generated in the LbL layer cannot reach a donor/acceptor interface. Here, the author therefore evaluates the exciton diffusion efficiency η_{ED}, which is the probability that the photogenerated exciton diffuses to a donor/acceptor interface before deactivating to the ground state, from exciton quenching experiments. First the author measured the PL spectra of double-layered films with different layered structures as shown in Figures 4–2a and 4–2b to evaluate the quenching efficiency qualitatively: $(PPV/PSS)_n/PPV|C_{60}:PS$ films and $(PPV/PSS)_n/PPV|PS$ reference films. The PL intensity is normalized by that of the reference film with the same PPV/PSS LbL film in thickness. The quenching efficiency Φ_q is estimated by $1 - I/I_0$ where I is the PL intensity of $(PPV/PSS)_n/PPV|C_{60}:PS$ films and I_0 is that of the reference films. For the thinnest PPV/PSS LbL layer, Φ_q was as high as 0.95 suggesting that almost all excitons are efficiently quenched at the quenching wall of the $C_{60}:PS$ film. The quenching mechanism will be discussed later. As the thickness of the PPV/PSS LbL layer increased from 3 to 12 nm, the PL intensity increased as shown in Figure 4–7 and hence Φ_q decreased, suggesting that the exciton quenching occurs only at a donor/acceptor interface and therefore some excitons cannot reach the interface as the thickness of the PPV/PSS LbL layer increases. Thus, the author can discuss the exciton diffusion by analyzing the dependence of Φ_q on the thickness of the PPV/PSS LbL layer as describe below.

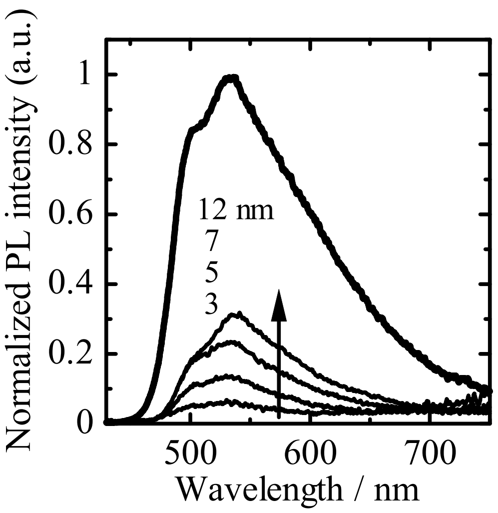

Figure 4–7. PL spectra of double-layered films with a layered structures of (PPV/PSS)$_n$/PPV (3–12 nm)|C$_{60}$:PS (solid lines) and the reference film with a layered structure of (PPV/PSS)$_7$/PPV (14 nm)|PS (thick solid line), as shown in Figures 4–2a and 4–2b, respectively. The excitation wavelength was 420 nm. Each PL intensity of (PPV/PSS)$_n$/PPV|C$_{60}$:PS was normalized by that of the reference film with the same thickness of PPV/PSS LbL film.

To discuss the quenching efficiency quantitatively, the author next measured the exciton lifetime by the time-correlated single-photon-counting method. This approach is more reliable than the PL intensity measurement because it is less sensitive to slight variations in the experimental conditions.[36] Figure 4–8 shows the PL decay of double-layered films with different layered structures. The solid lines represent the PL decay of double-layered films with a layered structure of (PPV/PSS)$_n$/PPV(3–12 nm)|C$_{60}$:PS. The thick solid line represents the PL decay of a double-layered reference film with a layered structure of (PPV/PSS)$_n$/PPV(14 nm)|PS. The PL decays are well fitted by eq. 4–3,

$$I(t) = I(0)\sum_i A_i \exp\left(-\frac{t}{\tau_i}\right) \tag{4–3}$$

where $I(t)$ and $I(0)$ are the PL intensity at time t and 0, respectively, A_i is the fraction of i th component, and τ_i is the decay constant. The average PL lifetime $<\tau>$ is calculated by eq. 4–4.[12]

$$\langle\tau\rangle = \frac{\sum_i A_i \tau_i^2}{\sum_i A_i \tau_i} \tag{4–4}$$

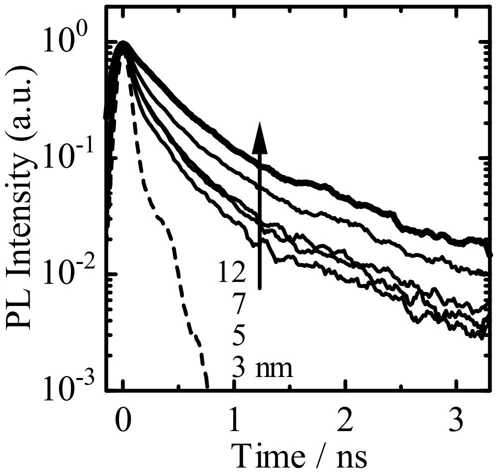

Figure 4–8. Fluorescence decay curves of double-layered films with a layered structures of $(PPV/PSS)_n/PPV$ (3–12 nm)|C_{60}:PS (solid lines) and the reference film with a layered structure of $(PPV/PSS)_7/PPV$(14 nm)|PS (thick solid line), as shown in Figures 4–2a and 4–2b, respectively. The excitation wavelength was 440 nm. The broken line represents the instrument response function (FWHW ~60 ps).

The exciton lifetime in the PPV/PSS reference film is evaluated to be $<\tau_0> = 0.67 \pm 0.02$ ns, which is slightly longer than previously reported values.[37–39] On the other hand, the exciton lifetime in the PPV/PSS LbL films with the C_{60}:PS quenching layer was dependent on the thickness of the PPV/PSS LbL layer; it increased from 0.40 ns at 5 nm to 0.63 ns at 12 nm with an experimental error of 2% at most. This tendency is qualitatively consistent with the

PL quenching efficiency mentioned before. Furthermore, the author can evaluate the quenching efficiency Φ_q by integrating eq. 4–3. Table 4–2 summarizes the averaged exciton lifetime <τ>, other fitting parameters, and Φ_q. On the basis of these quenching experimental results, the author will discuss later the diffusion constant of excitons in the PPV/PSS LbL layer.

Table 4–2. Fitting parameters in eq 4–3, <τ>, and Φ_q.

L / nm	A_1 [a]	τ_1 [a] / ns	A_2 [a]	τ_2 [a] / ns	A_3 [a]	τ_3 [a] / ns	<τ> / ns	Φ_q [c]
3	0.86	0.02	0.12	0.21	0.02	1.10	0.40 ± 0.01	0.83
5	0.75	0.02	0.22	0.17	0.03	0.91	0.40 ± 0.01	0.78
7	0.75	0.05	0.21	0.24	0.04	1.11	0.45 ± 0.01	0.66
12	0.69	0.07	0.25	0.31	0.06	1.32	0.63 ± 0.01	0.46
14[b]	0.84	0.23	0.16	1.16	—	—	0.67 ± 0.02	—

[a] The experimental error was within 2%.

[b] Fitted with a sum of two exponential functions.

[c] Evaluated by $1 - I/I_0$ where I and I_0 are calculated by the integration of eq. 4–3 using fitting parameters.

4.4. Discussion

4.4.1. *Exciton Generation*

The exciton generation is proportional to the optical intensity in the light-harvesting layer. Thus, the author first considers how the optical intensity depends on the layered structure of the device. As shown in Figures 4–4 and 4–5, the spatial distribution of the optical intensity $|\boldsymbol{E}(x)|^2$ in the multilayered device is significantly dependent on the thickness of the C_{60}:PS layer rather than that of the PPV/PSS LbL layer. This is partly due to the relatively large refractive index of the C_{60}:PS layer, which extends the optical length effectively and hence shifts the peak position close to the electrode. This effect has been reported as the optical spacer effect,[40,41] which can enhance light absorption as a result of redistribution of the optical electric field for thin films but is less pronounced for thicker films.[42] In the devices, the optical intensity $|\boldsymbol{E}(x)|^2$ in the LbL layer is maximized with ~30 nm of the C_{60}:PS layer as shown in Figure 4–5a. Consequently, the photon absorption efficiency leading to the exciton generation in the LbL layer η_A^{LbL} is also maximized with ~30 nm of the C_{60}:PS layer as shown in Figure 4–6b. This trend is consistent with the dependence of J_{SC} on the thickness of the C_{60}:PS layer. If excitons generated in the C_{60}:PS layer mainly contributed to the photocurrent generation, the dependence of J_{SC} on the thickness of the C_{60}:PS layer would follow that of η_A^{C60} considering the C_{60} exciton diffusion length as long as 40 nm.[8] As shown in Figures 4–3b and 4–6b, this is not the case. Thus, the author concludes that excitons generated in the LbL layer mainly contribute to the photocurrent generation. The negligibly minor contribution of C_{60} excitons to the photocurrent generation is partly due to their rapid intersystem crossing to triplet state as previously discussed.[21] More importantly, it is noteworthy that the optical intensity in the light-harvesting layer can be maximized by optimization of the thickness of the C_{60}:PS layer.

On the other hand, as mentioned before, the increase in the thickness of the PPV/PSS LbL layer does not affect the spatial distribution of the optical intensity $|\boldsymbol{E}(x)|^2$ but simply decreases the intensity mainly because of the absorption in the layer. As a result, as shown in Figure 4–6a, η_A^{LbL} increases monotonically with the increase in the thickness of the PPV/PSS LbL layer and then is gradually saturated above 20 nm. Assuming that the reflection at the Al electrode is 100%, the optical length in the device would be twice and therefore the absorption could be estimated from twice the absorbance of the film. As shown in Figure 4–6a, η_A^{LbL} is larger for thinner LbL films (<30 nm) than the absorption calculated from twice the absorbance of the film, but smaller for thicker LbL films (>30 nm). These results show that the photon absorption efficiency is enhanced for thinner LbL films (<30 nm) but is rather suppressed for thicker LbL films (>30 nm) by the optical interference effect. Consequently, no increase in η_A^{LbL} is expected above 20 nm even though the thickness of the LbL layer increases. As shown in Figure 4–3a, such saturation is also seen in the dependence of J_{SC} on the thickness of the LbL layer. Nonetheless, the optimized thickness of the LbL layer is substantially different between η_A^{LbL} and J_{SC}. This discrepancy suggests that not all of excitons generated in the LbL layer can reach a donor/acceptor interface or contribute to the photocurrent generation. Thus, the author will discuss the exciton diffusion efficiency η_{ED} in the next section.

4.4.2. *Exciton Diffusion*

The author discusses the exciton diffusion in the PPV/PSS LbL film using the one-dimensional diffusion model in the direction normal to the substrate.[11] Figure 4–9 shows a schematic illustration of concentration profiles of the exciton in the PPV/PSS LbL film with a thickness of L where x axis is the direction normal to the substrate, the interface between the inert substrate and the PPV/PSS LbL film is located at $x = 0$, and the quenching surface of the C_{60}:PS film is located at $x = L$.

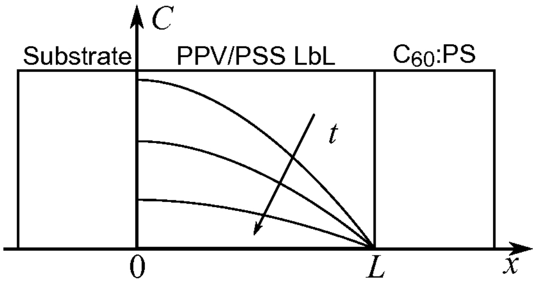

Figure 4–9. Schematic illustration of the time dependence of the concentration profiles $C(x,t)$ of PPV excitons in the PPV/PSS LbL film with a thickness of L nm where x axis is the direction normal to the substrate, the interface between the inert substrate and the PPV/PSS LbL film is located at $x = 0$, and the quenching surface of the C_{60}:PS film is located at $x = L$.

In this model, the concentration of the exciton $C(x,t)$ obeys the Fick's law and can be expressed with a diffusion constant D by

$$\frac{\partial C(x,t)}{\partial t} = D\frac{\partial^2 C(x,t)}{\partial x^2} \tag{4–5}$$

As the initial condition, $C(x,0)$ is assumed to be constant throughout the film. This assumption is reasonable as shown in Figure 4–4a, because the film is thin enough to be excited homogeneously.

$$C(x,0) = C_0 \tag{4–6}$$

As boundary conditions, it is assumed that all excitons arriving at $x = L$ are quenched by the C_{60}:PS layer. This is also reasonable because the quenching efficiency Φ_q is close to unity for the thinnest LbL layer as mentioned before. Thus, one of the boundary conditions is given by

$$C(L,t) = 0 \tag{4–7}$$

It is also assumed that all excitons arriving at $x = 0$ are just reflected to the opposite direction. Thus, the other boundary condition is given by

$$\left[\frac{\partial C(x,t)}{\partial x}\right]_{x=0} = 0 \tag{4–8}$$

With these boundary conditions eq. 4–5 can be analytically solved, and hence $C(x,t)$ is given by

$$C(x,t) = C_0 - C_0 \sum_{n=0}^{\infty} (-1)^n \times \left[\operatorname{erfc}\frac{(2n+1)L - x}{2\sqrt{Dt}} + \operatorname{erfc}\frac{(2n+1)L + x}{2\sqrt{Dt}} \right] \tag{4–9}$$

Consequently, the author can calculate the quenching efficiency $\Phi_q(L,D)$ as a function of L and D.

$$\Phi_q(L,D) = 1 - \frac{I}{I_0} = 1 - \frac{\int_0^{\infty} I_0(t) \int_0^L C(x,t)\mathrm{d}x\mathrm{d}t}{\int_0^{\infty} I_0(t) \int_0^L C_0 \mathrm{d}x\mathrm{d}t} \tag{4–10}$$

Figure 4–10 shows the quenching efficiency Φ_q evaluated by the PL decay (open circles) and the quenching efficiency $\Phi_q(L,D)$ predicted by eq. 4–10 with several diffusion constants over three orders of magnitude (solid lines). As shown in the figure, the experimental quenching efficiencies Φ_q are close to one of predicted lines $\Phi_q(L,D = 10^{-3}$ cm^2 s^{-1}). More precisely, they are well reproduced with an exciton diffusion constant of $D = 8 \times 10^{-4}$ cm^2 s^{-1}. Slight deviations seen for thinner PPV/PPS layers (L <5 nm) are probably due to a static quenching, which is likely to be missed in the time-correlated single-photon-counting method. Indeed, the predicted $\Phi_q(L,D)$ is consistent with the PL quenching efficiency Φ_q as high as 0.95 observed for the thinnest PPV/PSS LbL layer. As mentioned before, the exciton lifetime is $<\tau_0> = 0.67$ ns. Therefore, the exciton diffusion length is estimated to be $(2D<\tau_0>)^{1/2} = 10$ nm, which is slightly longer than previously reported values: The exciton diffusion length has been reported to be 5–8 nm for PPV and PPV derivatives.[12,36,38,43,44] This is partly because the exciton lifetime in the PPV/PSS LbL film is longer than that in other reports for PPV and PPV derivatives (0.2–0.5 ns). The relatively longer exciton lifetime is consistent with the improved PL efficiency as reported previously.[20] The author ascribed the improvement to the decrease in trap-site concentration due to the low temperature conversion of PPV. Therefore, the author concludes that the long exciton diffusion is characteristic of PPV/PPS LbL films converted at a low temperature, which is beneficial for polymer-based solar cells.[21]

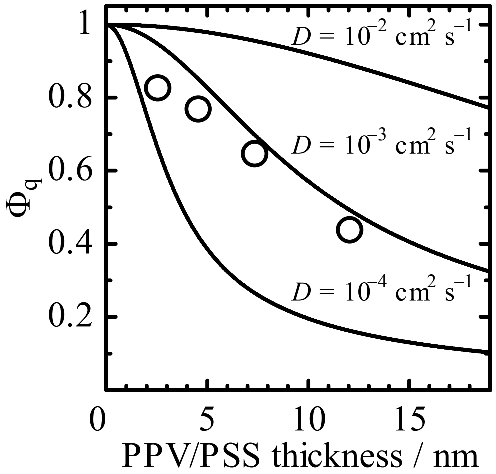

Figure 4–10. Dependence of Φ_q on the thickness of PPV/PSS LbL film. The open circles represent Φ_q evaluated from the PL decays. The solid lines represent $\Phi_q(L,D)$ with different diffusion constants of $D = 10^{-2}$, 10^{-3}, and 10^{-4} cm^2 s^{-1}. The experimental error was as small as 2% and the error bars were within the circles.

4.4.3. *Photon Conversion Efficiency*

Finally, the author discusses the photocurrent generation in terms of EQE, which can be defined by eq. 4–11 as the product of the efficiencies of four sequential steps: 1) the efficiency of photon absorption leading to the exciton generation η_{A}, 2) the efficiency of exciton diffusion to a donor/acceptor interface η_{ED}, 3) the efficiency of exciton dissociation by charge transfer at a donor/acceptor interface η_{CT}, 4) the efficiency of charge collection of charge separated carriers to the electrodes η_{CC}.

$$\mathrm{EQE} = \eta_{\mathrm{A}} \times \eta_{\mathrm{ED}} \times \eta_{\mathrm{CT}} \times \eta_{\mathrm{CC}} \qquad (4\text{–}11)$$

As described before, η_{A} was calculated by the transfer matrix method. The author can evaluate η_{ED} as $\Phi_{\mathrm{q}} = \eta_{\mathrm{ED}} \times \eta_{\mathrm{q}} \sim \eta_{\mathrm{ED}}$, because the quenching efficiency at the interface η_{q} is almost unity as mentioned before. Thus, η_{CT} can be assumed to be unity if the quenching mechanism is due to the charge transfer at a donor/acceptor interface. Another possible quenching mechanism is the energy transfer from PPV exciton to C_{60} as reported previously.[21] The author roughly estimates the energy transfer rate based on the Förster theory assuming point dipoles to be $\sim 10^{12}\ \mathrm{s}^{-1}$ for a PPV–C_{60} separation distance of 1 nm. This is two orders of magnitude less than the charge transfer rate reported for PPV/PCBM blends.[45] Thus, the author concludes that the quenching is mainly due to the charge transfer at the donor/acceptor interface. Consequently, the author can set $\eta_{\mathrm{CT}} = 1$ for the multilayered organic solar cells. Therefore, η_{CC} can be estimated by eq. 4–11 with η_{A}, η_{ED}, η_{CT}, and the experimental EQE values as shown in Figure 4–3a. Figure 4–11 summarizes the dependence of η_{A}, η_{ED}, η_{CC}, and EQE on the thickness of the PPV/PSS LbL film. As shown in the figure, η_{CC} is almost constant at around 0.5 above 7 nm in thickness. This indicates that half of the charges generated at the donor/acceptor interface can be collected at the electrodes under the short-circuit condition, which is consistent with previous report.[21] Possible loss mechanisms for

η_{CC} are a rapid back recombination and an efficient bimolecular recombination in the film. On the basis of these efficiencies in each primary process, the author concludes that EQE of multilayered solar cells is optimized as a result of a balance between η_A and η_{ED}, which can be tuned by the precise thickness control of the LbL layer on a scale of nanometers.

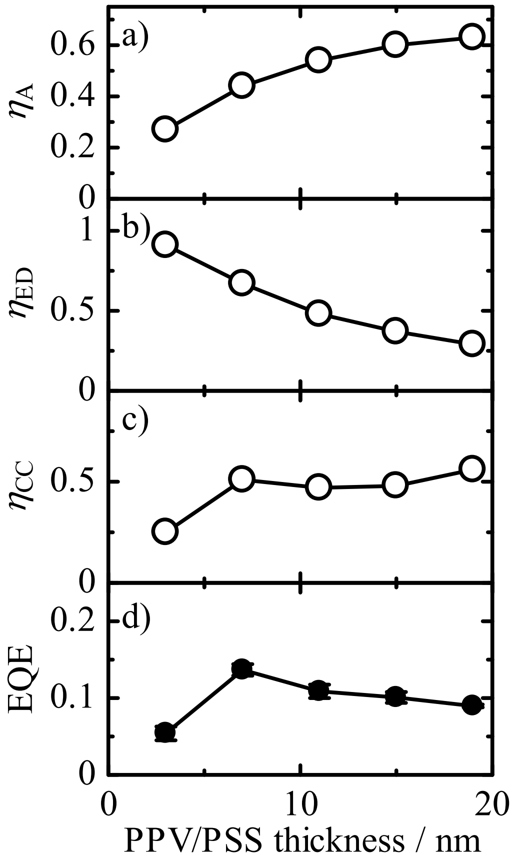

Figure 4–11. Dependence of each efficiency on the thickness of the PPV/PSS LbL film: a) η_A is estimated by the transfer matrix method, b) η_{ED} is evaluated from the PL quenching experiment, c) η_{CC} is estimated from η_A, η_{ED}, and EQE, and d) EQE at 420 nm is the same experimental data as shown in Figure 4–3a. The device structure is as follows: ITO(200 nm)|PEDOT:PSS(80 nm)|(PPV/PSS)$_n$/PPV(3–19 nm)|C_{60}:PS(30 nm)|Al. The experimental error of data points in each efficiency was as small as 5% and the error bars were within circles.

As described above, the device performance can be quantitatively explained by efficiencies in fundamental processes evaluated on the basis of the layered structure of the device. This is a great advantage for designing multilayered organic solar cells, as already reported for small molecule-based organic solar cells fabricated by dry processes such as vacuum deposition. In this chapter, the author fabricated multilayered solar cells only by solution processes such as spincoating and LbL deposition techniques. This suggests that even solution-processed multilayered solar cells can be designed with a layered structure precisely controlled on a scale of nanometers by the LbL deposition technique, therefore, upon which the device performance can be optimized, as is the case with dry-processed small molecule-based organic solar cells.

4.5. Conclusions

The author fabricated all solution-processed organic thin-film solar cells consisting of a hole-transporting PEDOT:PSS layer, a light-harvesting PPV/PSS LbL layer, and an electron-transporting C_{60}:PS layer. The thickness of the PPV/PSS LbL layer was precisely varied between 3 nm and 19 nm on a scale of nanometers by the LbL deposition technique. The thickness of the C_{60}:PS layer was also varied between 20 nm and 50 nm by adjusting the spin rate. First, the photon absorption efficiency leading to exciton generation η_A in the light-harvesting LbL layer was estimated for various device structures by the transfer matrix method. The η_A value was more sensitively dependent on the thickness of the C_{60}:PS layer than that of the PPV/PSS LbL layer. Thus, the author concludes that the C_{60}:PS layer serves as an effective optical spacer to enhance the optical intensity in the light-harvesting layer. Furthermore, η_A was enhanced for thinner LbL films (<30 nm) but rather suppressed for thicker LbL films (>30 nm) because of the optical interference effect. Second, the efficiency of exciton diffusion into a donor/acceptor interface η_{ED} was evaluated from the PL quenching experiments. The exciton lifetime was evaluated to be 0.67 ± 0.02 ns by the PL decay measurement, which is slightly longer than previously reported values. Using the one-dimensional diffusion model, the author estimated the exciton diffusion constant to be 8×10^{-4} cm^2 s^{-1}, and the exciton diffusion length to be 10 nm, which is comparable to the optimized thickness of the PPV/PSS LbL layer. Third, the efficiency of exciton dissociation by charge transfer at a donor/acceptor interface was assumed to be $\eta_{\mathrm{CT}} \sim 1$ because the PL quenching was as high as 0.95 for the thinnest LbL film. Finally, the efficiency of charge collection to the electrodes η_{CC} was estimated to be ~0.5 for the PPV/PSS LbL layer with a thickness of >7 nm from η_{A}, η_{ED}, η_{CT}, η_{CC}, and experimentally obtained EQE values. These results demonstrate that the device performance can be quantitatively explained in terms of the device structure. Therefore, the author can rationally improve the device performance by optimizing the device structure on the basis of these device analyses, which is a great advantage of multilayered organic thin-film solar cells as reported for small molecule-based solar cells so far.

4.6. Appendix

4.6.1. ***Sample Preparation for the Structural Analysis***

Quartz substrates were washed by ultrasonication in toluene, acetone, and ethanol for 15 min, respectively, and then dried with a N_2 flow. These pre-washed substrates were further treated with a UV–O_3 cleaner for 1 h. A layer-by-layer (LbL) deposited film of pre-PPV and PSS was prepared as follows.[21] The substrate was immersed in the 1 mM pre-PPV aqueous solution for 5 min, rinsed in ultrapure water for 3 min, immersed in the 10 mM PSS aqueous solution for 5 min, and rinsed in ultrapure water for 3 min. This cycle gives one bilayer of pre-PPV and PSS, which is abbreviated as (pre-PPV/PSS)$_1$. Each LbL film was completely dried under a flow of air for 4–6 min after each immersion. The (n + 0.5) bilayers of pre-PPV/PSS is abbreviated as (pre-PPV/PSS)$_n$/pre-PPV. Finally, the (pre-PPV/PSS)$_n$/pre-PPV LbL layer was thermally converted to the (PPV/PSS)$_n$/PPV LbL layer by annealing at 100 °C for 2 h under vacuum.

4.6.2. *Characterization of Layer-by-Layer Deposited Films*

To examine the monolayer thickness of each layer in an LbL film, the author measured absorption spectra of the film with a spectrophotometer (Hitachi, U-3500) and line profiles of the LbL film partially scratched out with an atomic force microscope (AFM, Shimadzu, SPM-9500J). Figure 4–A1 shows the absorption spectra of (pre-PPV/PSS)$_n$ (n = 2, 4, 6, 8) layers on quartz substrates. The broken lines and the solid lines denote the absorption spectra of LbL films before and after the thermal conversion of pre-PPV, respectively. All of the PPV/PSS LbL films after annealing exhibited an absorption band at around 400 nm, which was attributed to π–π* transition of the main chain conjugation of PPV,[20] indicating the thermal conversion of pre-PPV into PPV. As shown in the inset of Figure 4–A1, the absorption at 400 nm increased in proportion to the number of PPV/PSS bilayers n. From the slope, the monolayer thickness of the PPV layer in LbL films was evaluated to be 0.9 nm on the basis of the absorption coefficient of a PPV spincoated film: α = 330,000 cm^{-1} at 400 nm. Figure 4–A2 shows an AFM image of the PPV/PSS LbL film with 8 bilayers. The bright area on the left side is the surface of the LbL film and the dark area on the right side is the surface of the substrate. The thickness of the film was evaluated to be 15 nm from the difference in height between these two levels. Figure 4–A3 shows plots of the thickness of PPV/PSS LbL films against the number of bilayers. From the slope, the bilayer thickness of a PPV/PSS LbL bilayer was evaluated to be 1.9 nm. Therefore, the monolayer thickness of the PSS layer in the LbL films was calculated to be 1.0 nm. Furthermore, this value was good agreement with the thickness calculated on the basis of the absorption coefficient of a PSS spincoated film: $\alpha = 170{,}000\ \mathrm{cm}^{-1}$ at 225 nm. Consequently, the monolayer thickness was 0.9 nm for PPV and 1.0 nm for PSS.

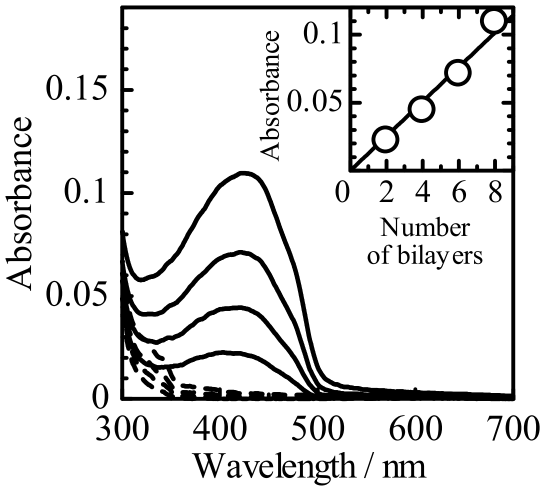

Figure 4–A1. Absorption spectra of (pre-PPV/PSS)$_n$ (n = 2, 4, 6, 8) layers on quartz substrates before (broken lines) and after (solid lines) the thermal annealing. The inset shows plots of the absorbance of the film at 400 nm against the number of bilayers.

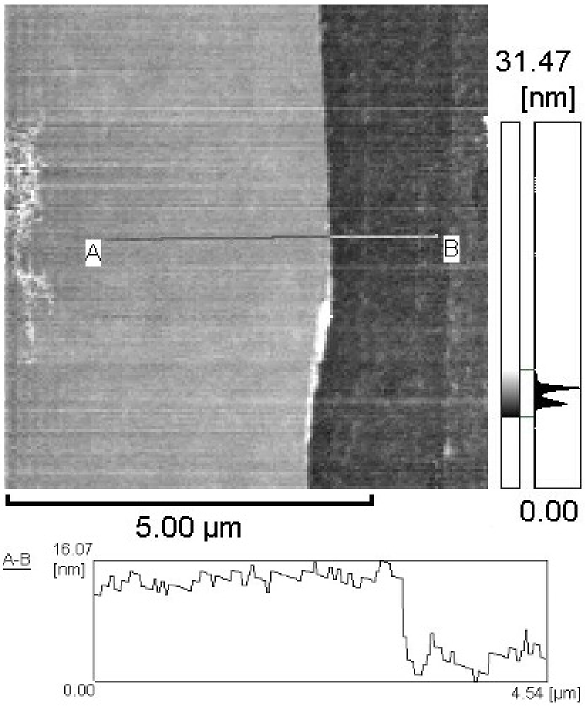

Figure 4–A2. AFM image of a PPV/PSS LbL film with 8 bilayers on a quartz substrate. The right dark area of the film was the surface of quartz substrate where the LbL film was scratched out.

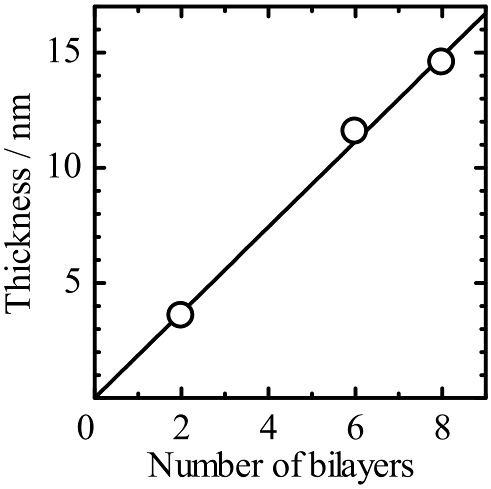

Figure 4–A3. Plots of the thickness of PPV/PSS LbL films against the number of bilayers.

4.6.3. *Calculation of Optical Electric Field Amplitude*

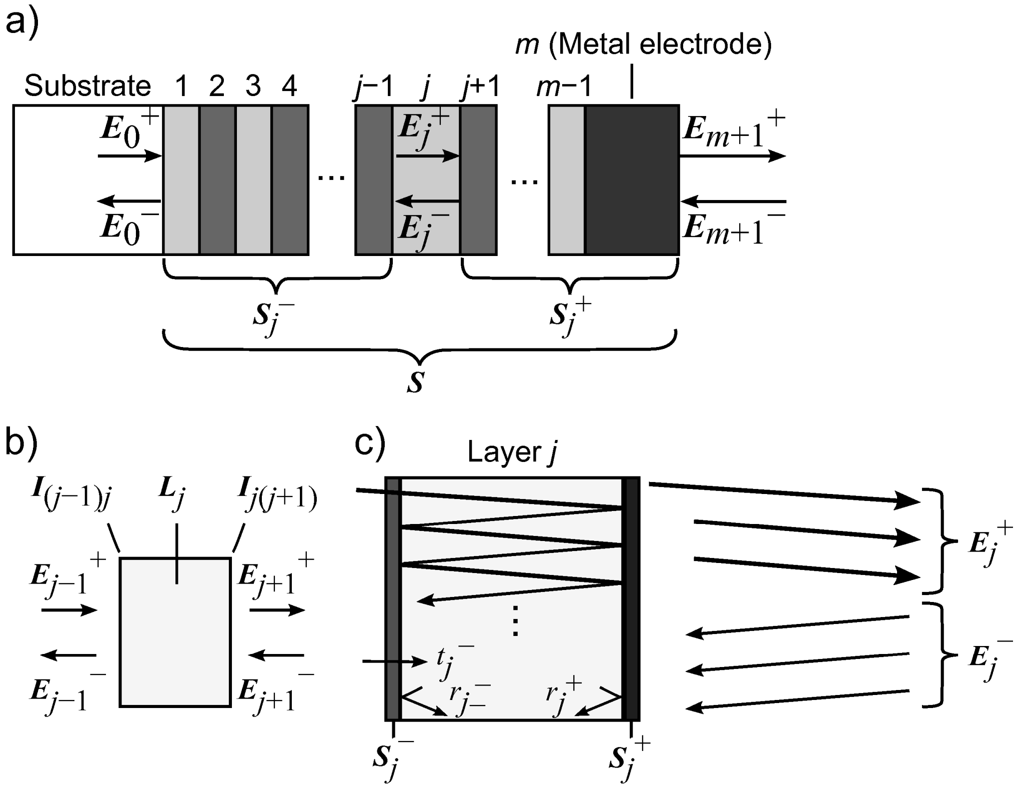

Figure 4–A4. Illustrations of optical simulation in multilayered devices: a) a general multilayered structure having *m* layers (including metal electrode), b) a layer *j* and the optical electric field amplitude for positive (E_{j-1}^+ and E_{j+1}^+) or negative direction (E_{j-1}^- and E_{j+1}^-) (which are related to each other by the layer matrix L_j and the interface matrices $I_{(j-1)j}$ and $I_{j(j+1)}$), c) The multiple reflection in the layer *j* between the partial systems, where t_j^- and r_{j-}^- denote the transmission and reflection coefficients of the partial system S_j^-, and r_j^+ denotes the reflection coefficient of the partial system S_j^+.

Figure 4–A4a shows the geometry of the multilayer stack employed in the optical electric field calculation. The optical electric field at any position can be resolved into two components, one of which is a component propagating in the positive *x* direction, and another of which is that in the negative *x* direction, which at a position *x* in layer *j* are denoted $E_j^+(x)$

and $\boldsymbol{E}_j^-(x)$, respectively. A layer j (j = 1, 2, ..., m) has a thickness d_j and a refractive index $N_j = n_j + i\,k_j$. The interface matrix $\boldsymbol{I}_{jk}$ is given by

$$\boldsymbol{I}_{jk} = \frac{1}{t_{jk}}\begin{bmatrix} 1 & r_{jk} \\ r_{jk} & 1 \end{bmatrix} \tag{4–A1}$$

where r_{jk} and t_{jk} are Fresnel complex reflection and transmission coefficients, respectively. For normal incidence, the Fresnel complex reflection and transmission coefficients can be given in the simplified form

$$r_{jk} = \frac{N_j - N_k}{N_j + N_k} \tag{4–A2}$$

$$t_{jk} = \frac{2N_j}{N_j + N_k} \tag{4–A3}$$

The propagation through a layer j causes absorption and a phase shift, as described by the layer matrix $\boldsymbol{L}_j$

$$\boldsymbol{L}_j = \begin{bmatrix} e^{-i\xi_j d_j} & 0 \\ 0 & e^{i\xi_j d_j} \end{bmatrix} \tag{4–A4}$$

where

$$\xi_j = \frac{2\pi}{\lambda} N_j \tag{4–A5}$$

and $\xi_j d_j$ is the phase thickness corresponding to the phase change. Note that the optical electric field for positive or negative direction in layer j as shown in Figure 4–A4b is given by

$$\begin{bmatrix} \boldsymbol{E}_{j-1}^{+} \\ \boldsymbol{E}_{j-1}^{-} \end{bmatrix} = \boldsymbol{I}_{(j-1)j}\boldsymbol{L}_j\boldsymbol{I}_{j(j+1)}\begin{bmatrix} \boldsymbol{E}_{j+1}^{+} \\ \boldsymbol{E}_{j+1}^{-} \end{bmatrix} \tag{4–A6}$$

By using the matrices of eq. 4–A1 and 4–A4, the total system transfer matrix $\boldsymbol{S}$ can be written by

$$\boldsymbol{S} = \begin{bmatrix} S_{11} & S_{12} \\ S_{21} & S_{22} \end{bmatrix} = \left(\prod_{p=1}^{m} \boldsymbol{I}_{(p-1)p} \boldsymbol{L}_p \right) \boldsymbol{I}_{m(m+1)} \tag{4–A7}$$

Note that $\boldsymbol{S}$ relates the electric field in the two outermost layers $j = 0$ and $j = m + 1$,

$$\begin{bmatrix} \boldsymbol{E}_0^+ \\ \boldsymbol{E}_0^- \end{bmatrix} = \boldsymbol{S} \begin{bmatrix} \boldsymbol{E}_{m+1}^+ \\ \boldsymbol{E}_{m+1}^- \end{bmatrix} \tag{4–A8}$$

When light is incident only from the substrate side in the positive x direction, there is no wave propagating in the negative x direction inside metal electrode side, which means that $\boldsymbol{E}_{m+1}^- = 0$. The reflection and transmission coefficients of the total layered system can be expressed by the matrix elements of $\boldsymbol{S}$,

$$r = \frac{\boldsymbol{E}_0^-}{\boldsymbol{E}_0^+} = \frac{S_{21}}{S_{11}} \tag{4–A9}$$

$$t = \frac{\boldsymbol{E}_{m+1}^+}{\boldsymbol{E}_0^+} = \frac{1}{S_{11}} \tag{4–A10}$$

To calculate the electric field in layer j, the layered system can be divided into two subsets, separated by layer j, which means that the total system transfer matrix can be written by

$$\boldsymbol{S} = \boldsymbol{S}_j^- \boldsymbol{L}_j \boldsymbol{S}_j^+ \tag{4–A11}$$

where $\boldsymbol{S}_j^-$ and $\boldsymbol{S}_j^+$ are the partial systems as follows:

$$\boldsymbol{S}_j^- = \begin{bmatrix} S_{j11}^- & S_{j12}^- \\ S_{j21}^- & S_{j22}^- \end{bmatrix} = \left(\prod_{p=1}^{j-1} \boldsymbol{I}_{(p-1)p} \boldsymbol{L}_p \right) \boldsymbol{I}_{(j-1)j} \tag{4–A12}$$

and

$$\boldsymbol{S}_j^+ = \begin{bmatrix} S_{j11}^+ & S_{j12}^+ \\ S_{j21}^+ & S_{j22}^+ \end{bmatrix} = \left(\prod_{p=j+1}^{m} \boldsymbol{I}_{(p-1)p} \boldsymbol{L}_p \right) \boldsymbol{I}_{m(m+1)} \tag{4–A13}$$

Note that both partial system transfer matrices relate the electric field at the substrate side and the metal electrode side by

$$\begin{bmatrix} \boldsymbol{E}_0^+ \\ \boldsymbol{E}_0^- \end{bmatrix} = \boldsymbol{S}_j^- \begin{bmatrix} \boldsymbol{E}_j'^+ \\ \boldsymbol{E}_j'^- \end{bmatrix} \tag{4–A14}$$

$$\begin{bmatrix} \boldsymbol{E}_j''^+ \\ \boldsymbol{E}_j''^- \end{bmatrix} = \boldsymbol{S}_j^+ \begin{bmatrix} \boldsymbol{E}_{m+1}^+ \\ \boldsymbol{E}_{m+1}^- \end{bmatrix} \tag{4–A15}$$

where $\boldsymbol{E}_j'^+$ and $\boldsymbol{E}_j'^-$ refer to the left boundary $(j-1)j$ of layer j, $\boldsymbol{E}_j''^+$ and $\boldsymbol{E}_j''^-$ refer to the right boundary $j(j+1)$ of layer j. Also in terms of the partial systems, the reflection and transmission coefficients can be expressed by the matrix elements of $\boldsymbol{S}_j^-$ or $\boldsymbol{S}_j^+$,

$$r_j^- = \frac{S_{j21}^-}{S_{j11}^-} \tag{4–A16}$$

$$t_j^- = \frac{1}{S_{j11}^-} \tag{4–A17}$$

$$r_j^+ = \frac{S_{j21}^+}{S_{j11}^+} \tag{4–A18}$$

$$t_j^+ = \frac{1}{S_{j11}^+} \tag{4–A19}$$

Furthermore, reflection coefficient from right side of the left partial system r_{j-}^- is expressed in a similar way,

$$r_{j-}^- = -\frac{S_{j12}^-}{S_{j11}^-} \tag{4–A20}$$

As shown in Figure 4–A4c, the electric field propagating in positive x direction in layer j at the left interface $(j-1)j$, $\boldsymbol{E}_j^+$ is derived using t_j^-, r_j^+, and r_{j-}^- as,

$$\begin{aligned} \boldsymbol{E}_j^+ &= \left[t_j^- + t_j^- r_j^+ r_{j-}^- e^{i2\xi_j d_j} + t_j^- \left(r_j^+ r_{j-}^- e^{i2\xi_j d_j} \right)^2 + \dots \right] \boldsymbol{E}_0^+ \\ &= \frac{t_j^-}{1 - r_j^+ r_{j-}^- e^{i2\xi_j d_j}} \boldsymbol{E}_0^+ = T_j^+ \boldsymbol{E}_0^+ \end{aligned} \tag{4–A21}$$

where T_j^+ is the ratio of $\boldsymbol{E}_j^+$ to the incident plane wave. Similarly, the electric field propagating in negative *x* direction in layer *j* at the left interface $(j-1)j$, $\boldsymbol{E}_j^-$ is derived as,

$$\begin{aligned} \boldsymbol{E}_j^- &= \left[t_j^- r_j^+ e^{i2\xi_j d_j} + t_j^- r_{j-}^- \left(r_j^+ e^{i2\xi_j d_j} \right)^2 + t_j^- r_{j-}^{-\,2} \left(r_j^+ e^{i2\xi_j d_j} \right)^3 + \dots \right] \boldsymbol{E}_0^+ \\ &= \frac{t_j^- r_j^+ e^{i2\xi_j d_j}}{1 - r_{j-}^- r_j^+ e^{i2\xi_j d_j}} \boldsymbol{E}_0^+ = r_j^+ e^{i2\xi_j d_j} T_j^+ \boldsymbol{E}_0^+ = T_j^- \boldsymbol{E}_0^+ \end{aligned} \tag{4–A22}$$

where T_j^- is the ratio of $\boldsymbol{E}_j^-$ to the incident plane wave. The total electric field in an arbitrary position in layer *j* is given in terms of the incident wave by

$$\begin{aligned} \boldsymbol{E}_j(x) &= \boldsymbol{E}_j^+(x) + \boldsymbol{E}_j^-(x) \\ &= \left[T_j^+ e^{i\xi_j x} + T_j^- e^{-i\xi_j x} \right] \boldsymbol{E}_0^+ \\ &= T_j^+ \left[e^{i\xi_j x} + S_{j21}^+ / S_{j11}^+ e^{i\xi_j (2d_j - x)} \right] \boldsymbol{E}_0^+ \\ &= \frac{S_{j11}^+ \cdot e^{-i\xi_j (d_j - x)} + S_{j21}^+ \cdot e^{i\xi_j (d_j - x)}}{S_{j11}^- S_{j11}^+ \cdot e^{-i\xi_j d_j} + S_{j12}^- S_{j21}^+ \cdot e^{i\xi_j d_j}} \boldsymbol{E}_0^+ \end{aligned} \tag{4–A23}$$

for $0 \le x \le d_j$. The time-averaged absorbed power of layer *j*, $Q_j(x)$, as a function of position *x* is given by

$$Q_j(x) = \frac{1}{2} c \varepsilon_0 \alpha_j n_j \left| \boldsymbol{E}_j(x) \right|^2 \tag{4–A24}$$

where ε_0 is the permittivity of free space and α_j is the absorption coefficient of layer *j*. Note that α_j is related to the extinction coefficient of layer *j*, k_j, as follows: $\alpha_j = 4\pi k_j/\lambda$. The number of time-averaged absorbed photons is obtained to be the product of $Q_j(x)$ and λ/hc. As a result, the efficiency of absorption of photons η_{A} is calculated by the ratio of the number of time-averaged absorbed photons to the number of the time-averaged incident photons.

References and Notes

(1) Kippelen, B.; Brédas, J.-L. *Energy Environ. Sci.* **2009**, *2*, 251–261.

(2) Solarmer Energy, Inc. Homepage. http://www.solarmer.com/ (accessed May 5, 2010).

(3) heliatek GmbH Homepage. http://www.heliatek.com/ (accessed May 5, 2010).

(4) Xue, J.; Uchida, S.; Rand, B. P.; Forrest, S. R. *Appl. Phys. Lett.* **2004**, 85, 5757–5759.

(5) Sakai, K.; Hiramoto, M. *Mol. Cryst. Liq. Cryst.* **2008**, *491*, 284–289.

(6) Dennler, G.; Scharber, M. C.; Brabec, C. J. *Adv. Mater.* **2009**, *21*, 1323–1338.

(7) Brabec, C. J.; Durrant J. R. *MRS Bull.* **2008**, *33*, 670–675.

(8) Peumans, P.; Yakimov, A.; Forrest, S. R. *J. Appl. Phys.* **2003**, *93*, 3693–3723.

(9) Forrest, S. R. *Chem. Rev.* **1997**, *97*, 1793–1896.

(10) Yang, F.; Forrest, S. R. *ACS Nano* **2008**, *2*, 1022–1032.

(11) Fushimi, T.; Oda, A.; Ohkita, H.; Ito, S. *J. Phys. Chem. B* **2004**, *108*, 18897–18902.

(12) Markov, D. E.; Hummelen, J. C.; Blom, P. W. M. *Phys. Rev. B* **2005**, *72*, 045216.

(13) Decher, G.; Hong J. D. *Makromol. Chem. Macromol. Symp.* **1991**, *46*, 321–327.

(14) Decher, G. *Science* **1997**, *277*, 1232–1237.

(15) Ariga, K.; Hill, J. P.; Ji, Q. *Phys. Chem. Chem. Phys.* **2007**, *9*, 2319–2340.

(16) Caruso, F. *Adv. Mater.* **2001**, *13*, 11–22.

(17) Hammond, P. T. *Adv. Mater.* **2004**, *16*, 1271–1293.

(18) Ferreira, M.; Cheung, J. H.; Rubner, M. F. *Thin Solid Films* **1994**, *244*, 806–809.

(19) Mattoussi, H.; Rubner, M. F.; Zhou, F.; Kumar, J.; Tripathy, S. K.; Chiang, L. Y. *Appl. Phys. Lett.* **2000**, *77*, 1540–1542.

(20) Ogawa, M.; Kudo, N.; Ohkita, H.; Ito S.; Benten, H. *Appl. Phys. Lett.* **2007**, *90*, 223107.

(21) Benten, H.; Ogawa, M.; Ohkita, H.; Ito, S. *Adv. Funct. Mater.* **2008**, *18*, 1563–1572.

(22) Benten, H.; Kudo, N.; Ohkita, H.; Ito, S. *Thin Solid Films* **2009,** *517*, 2016–2022.

(23) Ogawa, M.; Tamanoi, M.; Ohkita, H.; Benten, H.; Ito S. *Sol. Energy Mater. Sol. Cells* **2009**, *93*, 369–374.

(24) Mwaura, J. K.; Pinto, M. R.; Witker, D.; Ananthakrishnan, N.; Schanze, K. S.; Reynolds, J. R. *Langmuir* **2005**, *21*, 10119–10126.

(25) Durstock, M. F.; Spry, R. J.; Baur, J. W.; Taylor, B. E.; Chiang, L. Y. *J. Appl. Phys.* **2003**, *94*, 3253–3259.

(26) Li, H.; Li, Y.; Zhai, J.; Cui, G.; Liu, H.; Xiao, S.; Liu, Y.; Lu, F.; Jiang, L.; Zhu, D. *Chem. Eur. J.* **2003**, *9*, 6031–6038.

(27) Benten, H.; Guo, J.; Ohkita, H.; Ito, S.; Yamamoto, M.; Sakumoto, N.; Hori, K.; Tohda, Y.; Tani, K. *J. Phys. Chem. B* **2007**, *111*, 10905–10914.

(28) Ohkita, H.; Benten, H.; Anada, A.; Noguchi, H.; Kido, N.; Ito, S.; Yamamoto, M *Phys. Chem. Chem. Phys.* **2004**, 6, 3977–3984.

(29) Pettersson, L. A. A.; Roman, L. S.; Inganäs, O. *J. Appl. Phys.* **1999**, *86*, 487–496.

(30) *Handbook of Chemistry and Physics 68th ed.*; Weast, R. C.; Astle M. J.; Beyer, W. H., Eds.; The Chemical Rubber Co.: Cranwood Parkway, 1987; p E−372.

(31) Dennler, G.; Forberich, K.; Scharber, M. C.; Brabec, C. J.; Tomiš, I.; Hingerl, K.; Fromherz, T. *J. Appl. Phys.* **2007**, *102*, 054516.

(32) Kumar, S.; Biswas, A. K.; Shukla, V. K.; Awasthi, A.; Anand, R. S.; Narain, J. *Synth. Met.* **2003**, *139*, 751–753.

(33) Liu, L.; Li, P.; Asher, S. A. *J. Am. Chem. Soc.* **1999**, *121*, 4040–4046.

(34) These values were calculated by averaging as volume fraction between C_{60} and PS.

(35) Lehmuskero, A.; Kuittinen, M.; Vahimaa, P. *Opt. Express* **2007**, *15*, 10744–10752.

(36) Markov, D. E.; Amsterdam, E.; Blom, P. W. M.; Sieval, A. B.; Hummelen, J. C. *J.*

Phys. *Chem*. *A* **2005**, *109*, 5266–5274.

(37) Samuel, I. D. W.; Crystall, B.; Rumbles, G.; Burn, P. L.; Holmes, A. B.; Friend, R. H. *Chem*. *Phys*. *Lett*. **1993**, *213*, 472–478.

(38) Lewis, A. J.; Ruseckas, A.; Gaudin, O. P. M.; Webster, G. R.; Burn, P. L.; Samuel, I. D. W. *Org*. *Electron*. **2006**, *7*, 452–456.

(39) Smilowitz, L.; Hays, A.; Heeger, A. J.; Wang, G.; Bowers, J. E. *J. Chem*. *Phys*. **1993**, *98*, 6504–6509.

(40) Hänsel, H.; Zettl, H.; Krausch, G.; Kisselev, R.; Thelakkat, M.; Schmidt, H.-W. *Adv*. *Mater*. **2003**, *15*, 2056–2060.

(41) Kim, J. Y.; Kim, S. H.; Lee, H.-H.; Lee, K.; Ma, W.; Gong, X.; Heeger, A. J. *Adv*. *Mater*. **2006**, *18*, 572–576.

(42) Gilot, J.; Barbu, I.; Wienk, M. M.; Janssen, R. A. J. *Appl*. *Phys*. *Lett*. **2007**, *91*, 113520.

(43) Halls, J. J. M.; Pichler, K.; Friend, R. H.; Moratti, S. C.; Holmes, A. B. *Appl*. *Phys*. *Lett*. **1996**, *68*, 3120–3122.

(44) Markov, D. E.; Tanase, C.; Blom, P. W. M.; Wildeman, J. *Phys*. *Rev*. *B: Condens*. *Matter* **2005**, *72*, 045217.

(45) Brabec, C. J.; Zerza, G.; Cerullo, G.; Silvestri, S. D.; Luzzati, S.; Hummelen, J. C.; Sariciftci, S. *Chem*. *Phys*. *Lett*. **2001**, *340*, 232–236.

Chapter 5

Solution-Processed Multilayered Polymer Solar Cells Designed by Layer-by-Layer Assembly of Poly(*p*-phenylenevinylene)s with Dimethylsulfoxide

5.1. Introduction

Organic solar cells have been intensively studied because of their light-weight, flexibility, large-area and cost-effective production.[1–3] In organic solar cells, a coulombically bound electron and hole pair (exciton) is generated first after the photon absorption and can dissociate into free charged carriers only at the interface of donor and acceptor materials. Furthermore, the hopping length of each carrier such as exciton, hole, and electron, which plays an important role in the photon-to-current energy conversion, is limited on a scale of nanometers. Therefore, it is crucial to design the photon active layer with nanometer precision.

Ito and co-workers have designed and fabricated solution-processed multilayered polymer solar cells by combining the spincoating and layer-by-layer (LbL) deposition techniques.[4–7] The LbL deposition technique is a simple and versatile method for fabricating multilayered ultrathin films with various functional materials. Recently Ito and co-workers developed a triple-layered polymer solar cells with poly(*p*-phenylenevinylene) (PPV) conjugated polymer in the light-harvesting LbL layer whose thickness and interfacial nanostructures were carefully controlled with nanometer precision. The solar cell exhibited an internal quantum efficiency as high as 50%, which is indicative of efficient photon-to-current conversion, and hence a power conversion efficiency of 0.26%.[5] Ito and co-workers furthermore improved the LbL-based photovoltaic cell by introducing an anionic PPV derivative (MPS-PPV) instead of an inert anionic polymer and obtained a slightly higher power conversion efficiency (0.28%).[6] On the other hand, the optical properties of MPS-PPV have been reported to be improved by addition of surfactants,[8] polyelectrolytes,[9] dendrimers,[10,11] salts,[12] and organic solvents such as dimethylsulfoxide (DMSO)[12] to the original aqueous solution. Herein, the author demonstrates that the light-harvesting efficiency of multilayered polymer solar cells with PPV/MPS-PPV LbL layers can be improved by using a water/DMSO mixed solution of MPS-PPV as an LbL deposition solution.

5.2. Experimental Section

5.2.1. *Materials*

Figure 5–1 shows the PPV derivatives used in this chapter. For the fabrication of LbL films, cationic and anionic polyelectrolyte solutions were prepared as follows: a cationic PPV precursor, poly(*p*-xylene tetrahydro- thiophenium chloride) (pre-PPV, Aldrich, 0.25 wt%), aqueous solution was diluted to 1 mM at pH 8–9 with water and an anionic PPV derivative, poly[5-methoxy-2-(3-sulfopropoxy)-1,4-phenylenevinylene] (MPS-PPV, Aldrich, 0.25 wt%), aqueous solution was diluted to give a 2 mM aqueous solution (pH 7) or a 2 mM water/DMSO (1 : 1 by volume) mixed solution (pH 9). The MPS-PPV solution was ultrasonicated for 2 min and filtrated through a 0.45-μm membrane filter. For the fabrication of spincoated films, an aqueous solution of poly(3,4-ethylenedioxythiophene) : poly(4-styrenesulfonate) (PEDOT:PSS, Aldrich, 1.3 wt% dispersion in H_2O, conductive grade) mixed with ethylene glycol and a blend solution of *o*-dichlorobenzene with C_{60} (Frontier

Carbon Co. Ltd.) and polystyrene (PS, Aldrich, $M_W = 280{,}000$) (4 : 1 by weight) were used for a hole- transporting and an electron-transporting layer, respectively.

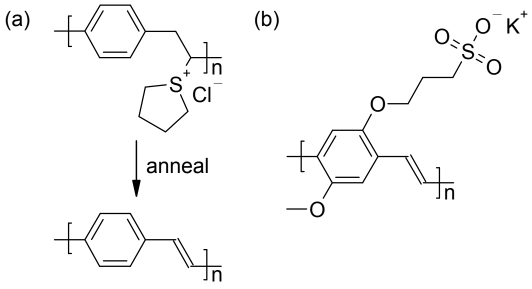

Figure 5–1. Chemical structures of PPV derivatives employed in this chapter: (a) thermal conversion of pre-PPV to PPV, (b) MPS-PPV.

5.2.2. *Device Fabrication*

Indium-tin-oxide (ITO)-coated glass substrates (10 Ω per square) were cleaned by ultrasonication in toluene, acetone, and ethanol for 15 min, respectively, and followed by surface treatment with a UV–O_3 cleaner for 60 min. First, a hole-transporting layer was prepared on the pre-cleaned ITO substrate by spincoating from a PEDOT:PSS solution, followed by thermal annealing at 70 °C for 12 h to give an insoluble film as reported previously.[7] Second, a light-harvesting layer was prepared by the LbL deposition of pre-PPV and MPS-PPV as follows. The PEDOT:PSS-coated ITO substrates were immersed in pre-PPV solution for 5 min, and rinsed with pure water for 3 min. Subsequently, they were immersed in MPS-PPV solution for 5 min and rinsed with pure water for 3 min. This cycle gives one-bilayer of pre-PPV/MPS-PPV LbL film. The LbL films were completely dried under a flow of air for 4–6 min after each immersion. Third, an electron- transporting layer was prepared on the LbL film by spincoating from an *o*-dichlorobenzene solution of C_{60} and

PS, followed by annealing at 100 °C for 2 h under vacuum to convert pre-PPV to PPV. Finally, Al was thermally deposited as a metal electrode on the top of the multilayered film through a metal mask to give an active area of 10 mm^2 (2 mm × 5 mm). The layered structure of the multilayered solar cell is as follows: ITO|PEDOT:PSS|(PPV/MPS-PPV)$_n$|C_{60}:PS|Al.

5.2.3. *Measurements*

For the absorption and fluorescence measurements, LbL films were fabricated on quartz substrates. The UV–visible absorption spectra and emission spectra of PPV solutions and LbL films were measured with a spectrophotometer (Hitachi, U-3500) and a fluorescence spectrometer (Hitachi, F-4500), respectively. The thickness and the surface morphology of the films were measured by atomic force microscopy (AFM, Shimadzu, SPM-9500J) in the contact mode. The *J–V* characteristics of the photovoltaic devices were measured with a DC voltage current source/monitor (Advantest, R6243). The photocurrent was measured under simulated AM1.5G solar illumination at 100 mW cm^{-2}. The external quantum efficiency (EQE) spectra were measured with a digital electrometer (Advantest, R8252) under monochromatic light. This monochromatic light was obtained by passing white light from a 500-W Xe lamp (Thermo Oriel, Model 66921) through a monochromator (Thermo Oriel, UV–visible Conerstone) with optical cut-filters. All these measurements were performed in air at room temperature.

5.3. Results and Discussion

First, the author examined the optical properties of MPS-PPV in water and in a mixed solvent of water and DMSO. Figure 5–2 shows molar absorption coefficient and emission spectra of MPS-PPV in water (broken line) and in the mixed solvent (solid line). The absorption spectra were similar although the molar absorption coefficient was slightly larger in the mixed solvent. On the other hand, the emission intensity increased by a factor of six in the mixed solvent relative to that in water. These results are consistent with a previous report.[12] This is probably because DMSO is a better solvent for the polymer backbone and hence may reduce the interaction between the main chain. Therefore, MPS-PPV chains are likely to expand more in the mixed solvent.

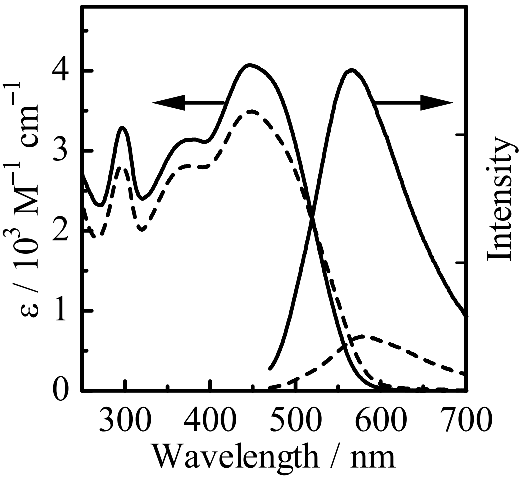

Figure 5–2. Molar absorption coefficient and emission spectra of MPS-PPV in water (broken lines) and in the mixed solvent of water and DMSO (solid lines).

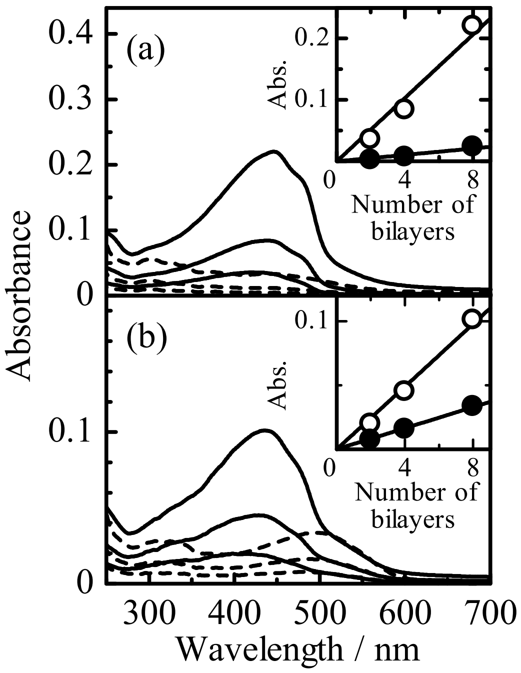

Figure 5–3. Absorption spectra of PPV/MPS-PPV LbL films before (broken lines) and after (solid lines) annealing. The MPS-PPV layers were fabricated from a) the aqueous solution and b) the water/DMSO mixed solution. The insets of each figure show the absorption at 440 nm after annealing (open circles), at 500 nm before annealing (closed circles) of the PPV/MPS-PPV LbL films plotted against the number of bilayers.

Next, the author focuses his attention on optical properties of LbL films with MPS-PPV. Figure 5–3a shows absorption spectra of pre-PPV/MPS-PPV films fabricated with the aqueous solution of MPS-PPV before and after annealing. Before the thermal annealing, the small absorption in the visible region was ascribed to MPS-PPV because pre-PPV has no absorption in that region. After the thermal annealing, a large absorption band was observed at around 400–500 nm, which is ascribed to π–π* transitions of thermally converted PPV. As reported previously,[6] the small absorption of MPS-PPV may be due to a broad distribution of effective conjugation lengths. In contrast, as shown in Figure 5–3b, a distinct absorption band was observed at around 500 nm even before the thermal annealing. This band was safely ascribed to MPS-PPV because there was no absorption due to pre-PPV. This is probably because MPS-PPV chains that are more expanded in the water/DMSO mixed solution are likely to be adsorbed on the film surface in more extended conformations at the LbL deposition, which result in a longer absorption band. On the other hand, as shown in the insets of each figure, the absorbance at 440 and 500 nm increased proportional to the number of bilayers, indicating that the constant amount of pre-PPV and MPS-PPV is deposited at each LbL step.

To compare the film morphology, the author measured AFM images of the PPV/MPS-PPV LbL films. For the reference LbL film with MPS-PPV fabricated from the aqueous solution, as shown in Figure 5–4a, the film surface was pinhole-free, uniform, and as smooth as the substrate surface, which is consistent with the previous report.[6] On the other hand, as shown in Figure 5–4b, the LbL film with MPS-PPV fabricated from the water/DMSO mixed solution was pinhole-free but not uniform: there were a lot of small bumps on the surface. A typical size of the bumps is ~10 nm in height and ~200 nm in diameter. From these results, the increase in the surface area due to the bumps is roughly estimated to be less than 1%, and therefore negligible to the increase in the interface. Such bumps may be formed during immersion in an aqueous solution of pre-PPV, because water is a poorer solvent for the polymer backbone and may induce partial shrinking of extended MPS-PPV chains on the film surface. From the step as shown in the figure, each film thickness was measured and consequently the bilayer thickness was evaluated to be 3–4 nm for either LbL film.

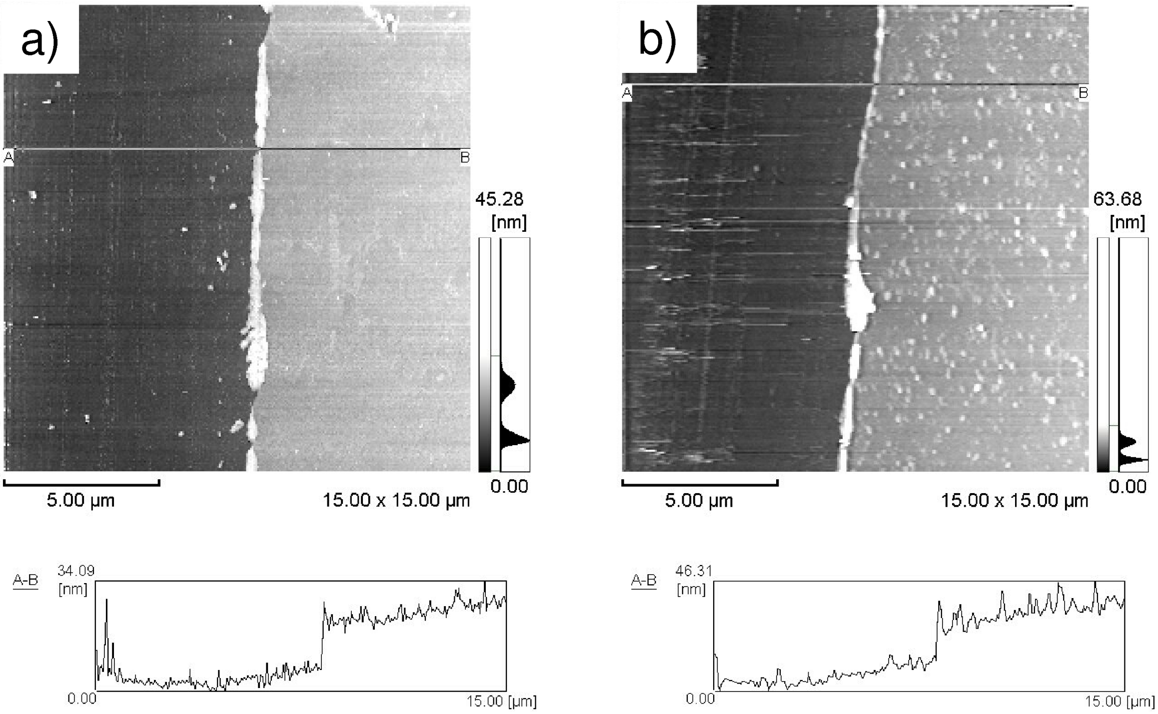

Figure 5–4. AFM images of PPV/MPS-PPV LbL films with a) 6 bilayers and b) 8 bilayers. The MPS-PPV layers were fabricated from a) the aqueous solution, b) the water/DMSO mixed solution. The left side of each film was the surface of quartz substrate where the LbL film was scratched out..

The author now moves onto the device performance of multilayered polymer solar cells with PPV/MPS-PPV LbL layers. Figure 5–5 shows *J*–*V* characteristics of the LbL-based solar cells with MPS-PPV fabricated from the water/DMSO mixed solution (solid line) and the reference cell from the aqueous solution (broken line). The thickness of the light-harvesting LbL layer was ~10 nm, which is optimized for the power conversion efficiencies. For LbL-based solar cells with MPS-PPV fabricated from the water/DMSO mixed solution, the short-circuit current density (J_{SC}) was improved by >10% but the open-circuit voltage (V_{OC}) and the fill factor decreased and consequently the resulting power conversion efficiency was comparable relative to the reference cell. The decrease in V_{OC} suggests that the shunt resistance decreased because of the rougher surface of the PPV/MPS-PPV layer as shown in Figure 5–4b. On the other hand, the increase in J_{SC} suggests that the light-harvesting efficiency of PPV/MPS-PPV LbL layers is improved by the fabrication of the MPS-PPV layer from the water/DMSO mixed solution. This improvement is so large (>10%) that it cannot be explained by the increase in the interface area due to the bumps on the surface (<1%) as mentioned before. Therefore, it is rather ascribable to the absorption enhancement in the visible region at around 500 nm as shown in Figure 5–3. To confirm this the author compared the EQE spectra of multilayered polymer solar cells with PPV/MPS-PPV LbL layers. As shown in Figure 5–6, a slight difference in the normalized EQE spectra was observed at around 500 nm: it was slightly larger in the cell fabricated from the water/DMSO mixed solution than in the reference cell. The slight increase in the absorption can account for an increase of ~10% in J_{SC}. The inset of the figure shows the spectral difference, which is consistent with the absorption of MPS-PPV layer as shown in Figure 5–3b. Therefore, the author concludes that the fabrication of MPS-PPV layer from the water/DMSO mixed solution can enhance the absorption in the visible region and hence the light-harvesting efficiency of multilayered polymer solar cells.

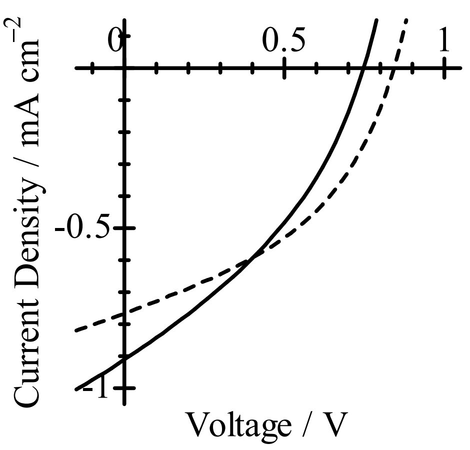

Figure 5–5. *J–V* characteristics of multilayered polymer solar cells with MPS-PPV fabricated from the aqueous solution (broken line) or the water/DMSO mixed solution (solid lines) of MPS-PPV.

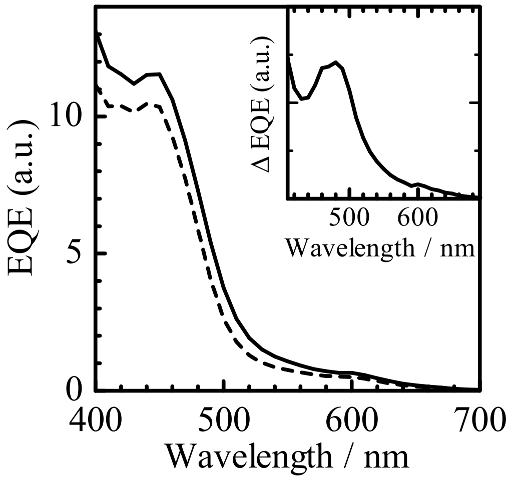

Figure 5–6. Normalized EQE spectra of multilayered polymer solar cells with MPS-PPV fabricated from the aqueous solution (broken line) or the water/DMSO mixed solution (solid lines). The inset shows the spectral difference between the two normalized EQE spectra.

5.4. Conclusions

The author has shown that optical properties of LbL films with MPS-PPV conjugated polymer can be tuned by changing the LbL deposition solution. By using the water/DMSO mixed solution of MPS-PPV for the LbL deposition, the absorption at around 500 nm became more remarkable compared with the reference LbL film with MPS-PPV fabricated from the aqueous solution. As a result, J_{SC} of multilayered polymer solar cells was improved by >10% relative to the reference cell fabricated from the aqueous solution. The increase in the EQE spectra at around 500 nm is consistent with the absorption enhancement and can account for the improvement in J_{SC}. Therefore, the author concludes that the light-harvesting efficiency of LbL-based multilayered solar cells can be improved by careful tuning of optical properties of LbL films.

References

(1) Günes, S.; Neugebauer, H.; Sariciftci, N. S. *Chem. Rev.* **2007**, *107*, 1324–1338.

(2) Thompson, B. C.; Fréchet, M. J. *Angew. Chem. Int. Ed.* **2008**, *47*, 58–77.

(3) Jørgensen, M.; Norrman, K.; Krebs, F. C. *Sol. Energy Mater. Sol. Cells* **2008**, *92*, 686–714.

(4) Benten, H.; Kudo, N.; Ohkita, H.; Ito, S. *Thin Solid Films* **2009**, *517*, 2016–2022.

(5) Benten, H.; Ogawa, M.; Ohkita, H.; Ito, S. *Adv. Funct. Mater.* **2008**, *18*, 1563–1572.

(6) Ogawa, M.; Tamanoi, M.; Ohkita, H.; Benten, H.; Ito, S. *Sol. Energy Mater. Sol. Cells* **2009**, *93*, 369–374.

(7) Ogawa, M.; Kudo, N.; Ohkita, H.; Ito, S.; Benten, H. *Appl. Phys. Lett.* **2007**, *90*, 223107.

(8) Dalvi-Malhorta, J.; Chen, L. *J. Phys. Chem. B* **2005**, *109*, 3873–3878.

(9) Abe, S.; Chen, L. *J. Polym. Sci., Part B: Polym. Phys.* **2003**, *41*, 1676–1679.

(10) Johal, M. S.; Howland, M.; Robinson, J. M.; Casson, J. L.; Wang, H. L. *Chem. Phys. Lett.* **2004**, *383*, 276–281.

(11) Montaño, G. A.; Dattelbaum, A. M.; Wang, H. L.; Shreve, A. P. *Chem. Commun.* **2004**, 2490–2491.

(12) Smith, A. D.; Shen, C. K.; Roberts, S. T.; Helgeson, R.; Schwartz, B. J. *Res. Chem. Intermed.* **2007**, *33*, 125–142.

Chapter 6

Hybrid Solar Cells of Layer-by-Layer Thin Film with Polymer/Fullerene Bulk Heterojunction

6.1. Introduction

Organic solar cells have attracted much attention because of their potential for lightweight and flexible devices and large-area and cost-effective production. The design of exciton dissociation interface between donor and acceptor materials is the key to the improvement in the device performance of organic solar cells. The intermixing of a conjugated polymer and fullerene in blend films has brought about a significant enhancement of the dissociation interface, leading to high power conversion efficiencies up to 6–7% more recently.[1,2] However, it is still difficult to artificially control the interfacial structures based on phase separation in such bulk heterojunction solar cells. Recently, solution-processed polymer solar cells by a combination of spincoating and layer-by-layer (LbL) deposition techniques was reported.[3,4] The LbL technique is not only simple and versatile, but also useful for fabricating multilayered ultrathin films with nanometer-scale precision;[5–8] thereby the thickness of a light-harvesting layer was precisely controlled to be comparable to the exciton diffusion length. Owing to the careful design of the thickness and interfacial structures, the internal quantum efficiency of the LbL-based solar cell was as high as ~50%.[4] However, the power conversion efficiency was still as low as 0.26% under AM1.5G simulated solar illumination at 100 mW cm^{-2}. This is mainly because the light-harvesting layer was as thin as ~10 nm and has an absorption band as short as 400 nm, resulting in inefficient photon absorption.

In the previous device, the electron-transporting layer is a blend film of C_{60} and polystyrene (PS) where PS serves as just a binder because of no absorption in the visible region but rather acts as an insulator for the charge transport.[4] Herein the author therefore replaced PS with poly(3-hexylthiophene) (P3HT) that has a large absorption in the visible region and a high hole mobility. As a result, the device structure is considered to be a hybrid solar cell integrating the LbL-based solar cell with bulk heterojunction solar cell. Furthermore, the author replaced C_{60} with C_{70} because C_{70} has a relatively high electron mobility[9,10] but also an absorption band in the visible region.[11,12] Consequently, the short-circuit current (J_{SC}) significantly increased from 0.8 to > 4 mA cm^{-2} and the open-circuit voltage (V_{OC}) remained as high as > 0.7 V, which is higher than that achievable by P3HT-based bulk heterojunction solar cells (~0.6 V).[13] The author discusses the increase in J_{SC} in terms of the photon absorption efficiency and the relatively higher V_{OC} in terms of the role of the LbL layer in the hybrid solar cells.

6.2. Experimental Section

6.2.1. *Device Fabrication*

Indium-tin-oxide (ITO) coated glass substrates (10 Ω square^{-1}) were cleaned by ultrasonication in detergent, acetone, and ethanol for 15 min, respectively, and exposed to UV–ozone atmosphere for 1 h. The first layer was prepared by spincoating on the ITO substrate from an aqueous solution of poly(3,4-ethylenedioxythiophene):poly(4-styrenesulfonate) (Aldrich, PEDOT:PSS) mixed with 20 wt% ethylene glycol. The PEDOT:PSS film was thermally annealed at 70 °C for 14 h in air and at 140 °C for 2 h under vacuum to give insoluble film as reported previously.[4] The thickness of the first layer was ~80 nm. This layer serves as a hole-transporting layer. The second layer was prepared by the LbL deposition with several combinations of a polycation and a polyanion listed in Figure 6–1: poly(*p*-xylene tetrahydrothiophenium chloride) (Aldrich, pre-PPV), poly(2-methoxy-5-propyloxysulfonate-1,4-phenylenevinylene) (Aldrich, MPS-PPV), poly(4-styrenesulfonate) (Aldrich, M_w = 70,000, PSS), and poly(dimethyldiallylammonium chloride) (Aldrich, M_w = 100,000–200,000, PDDA). This layer mainly serves as a light-harvesting layer but also a hole-transporting layer as the author will discuss later. The third layer was prepared by spincoating from an *o*-dichlorobenzene solution of several combination of a polymer and a fullerene (1:4 w/w for C_{60}, 1:5 w/w for C_{70}) listed in Figure 6–1: poly(3-hexylthiophene) (Aldrich, regioregular, M_w = 87,000, P3HT), polystyrene (Aldrich, M_w = 280,000, PS), C_{60} (Frontier Carbon), and C_{70} (Aldrich). Before the spincoating, each solution was ultrasonicated followed by the filtration through a 0.45-μm membrane filter. The thickness of the third layer was 30–40 nm unless otherwise noted. This layer serves as an electron-transporting layer or as a bulk heterojunction layer. The pre-PPV layer was converted to poly(*p*-phenylenevinylene) (PPV) by thermal annealing at 100 °C for 2 h under vacuum after the spincoating of the third layer. Finally, Al was thermally deposited as a counter electrode at 2.5×10^{-6} Torr on top of the multilayered film through a metal mask to give an active area of 6 mm^2 (2 × 3 mm^2).

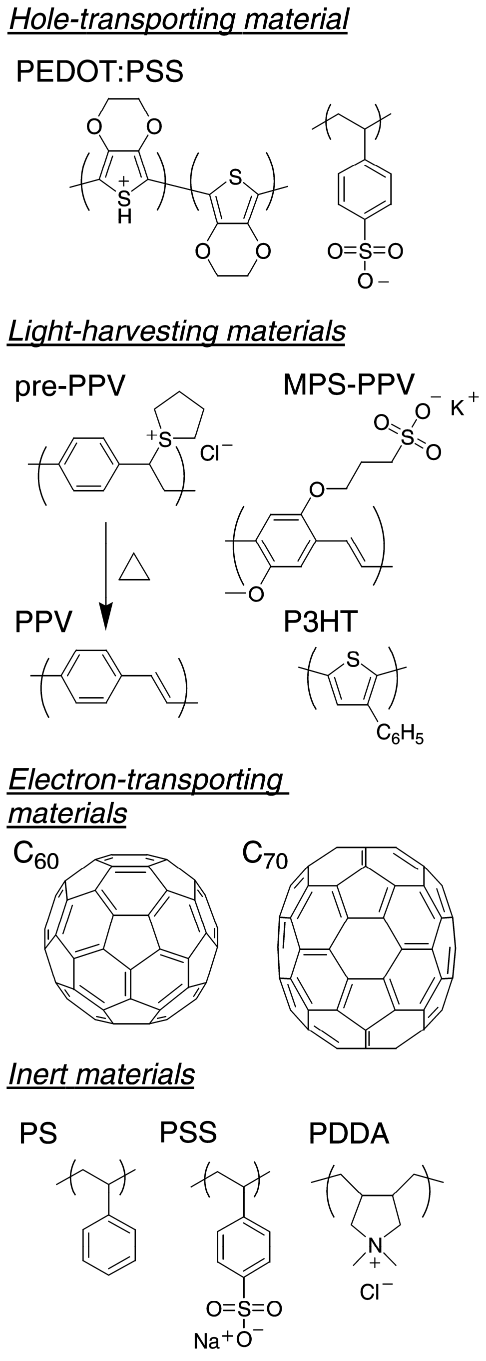

Figure 6–1. The chemical structures of various materials used in this chapter.

6.2.2. *Measurements*

Absorption spectra of the film were measured with a spectrophotometer (Hitachi, U-3500). For the absorption measurements, glass or quartz substrates were used instead of ITO-coated glass. The thickness and surface morphology of the film were measured with an atomic force microscope (Shimadzu, SPM-9500J) in the contact mode at room temperature. The current density–voltage (*J*–*V*) characteristics were measured with a DC voltage current source/monitor (Advantest, R6243) in the dark and under AM1.5G simulated solar illumination at 100 mW cm^{-2}. The external quantum efficiency spectra were measured with a digital electrometer (Advantest, R8252) under monochromatic light illumination from a 500-W Xe lamp (Thermo Oriel, Model 66921) with a monochromator (Thermo Oriel, UV–visible Conerstone) and several optical cut-filters (IRQ80, HOYA L-38, and AND-50S-25). The ionization potential of films was measured by ambient ultraviolet photoelectron spectroscopy (UPS) with a UPS spectrometer (Riken Keiki, AC-2). All measurements were performed in air at room temperature.

6.3. Results

6.3.1. *Device Performance of Hybrid Cells*

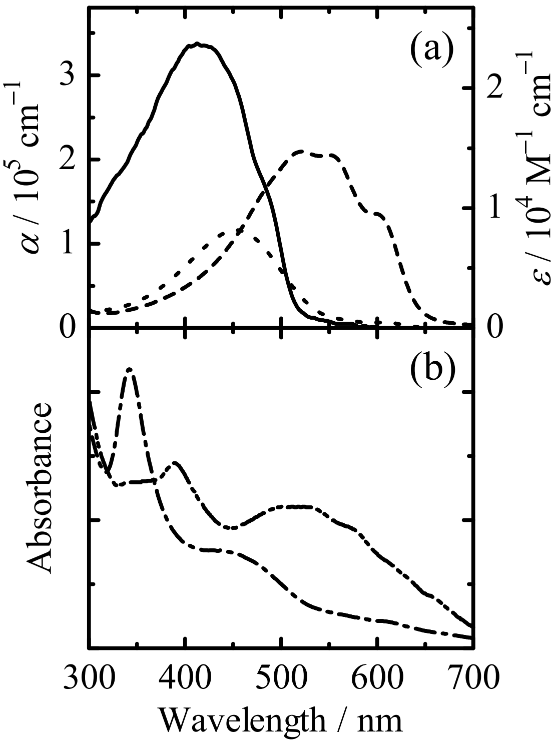

Figure 6–2. (a) Left: The absorption coefficient of pristine films of PPV (solid line) and P3HT (broken line). Right: The molar absorption coefficient of P3HT in toluene (dotted line). (b) The absorption spectra of blend films of C_{60}:PS (4:1 w/w) (dashed-dotted line) and C_{70}:PS (5:1 w/w) (dashed-two dotted line). The absorbance was normalized by the film thickness.

As shown in Figure 6–2, PPV has an absorption band around 400 nm, which overlaps with only a small portion of the solar spectrum with a photon flux peak around 700 nm. This is one of the reasons for the low power conversion efficiency of the PPV-based polymer solar cell the author reported previously.[4] The author therefore introduces light-harvesting materials to improve absorption efficiency for the solar light. In the previous photovoltaic cell, PS was employed as a binder for C_{60} in the electron-transporting layer. However, PS has no absorption in the visible region and rather acts as an insulator for the charge transport. Consequently, the author replaced PS with P3HT that has an absorption band in the longer wavelength than PPV, leading to the better spectral overlap with the solar light. Furthermore, the author replaced C_{60} with C_{70} that has substantial absorption up to 700 nm as shown in Figure 6–2b as well as relatively high electron mobility. The author should note that the electron-accepting layer incorporated with P3HT instead of PS is exactly bulk heterojunction structure. In other words, the photovoltaic device incorporated with P3HT can be considered to be a hybrid solar cell of LbL thin film with bulk heterojunction. Figure 6–3 shows *J–V* characteristics of a hybrid polymer solar cell (solid line) and an LbL-based solar cell (broken line) measured under AM1.5G simulated solar illumination at 100 mW cm^{-2}. Compared with the LbL-based solar cell, J_{SC} of the hybrid cell significantly increased from 0.8 to >4 mA cm^{-2} and V_{OC} slightly decreased but still remained as high as >0.7 V.

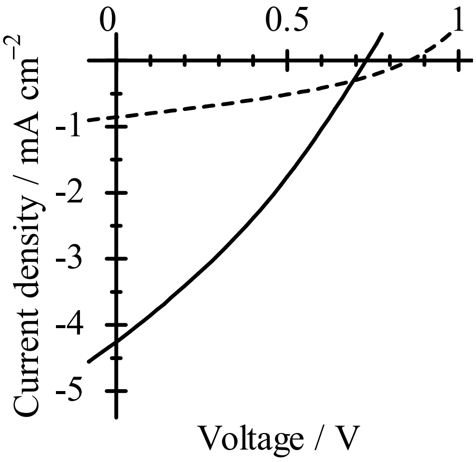

Figure 6–3. The *J–V* characteristics of a hybrid solar cell with a layered structure of ITO|PEDOT:PSS|$(PPV/MPS\text{-}PPV)_{2.5}$|$C_{70}$:P3HT|Al (solid line) and an LbL-based solar cell with a layered structure of ITO|PEDOT:PSS|$(PPV/PSS)_{2.5}$|C_{60}:PS|Al (broken line) under AM1.5G simulated solar illumination at 100 mW cm^{-2} in air.

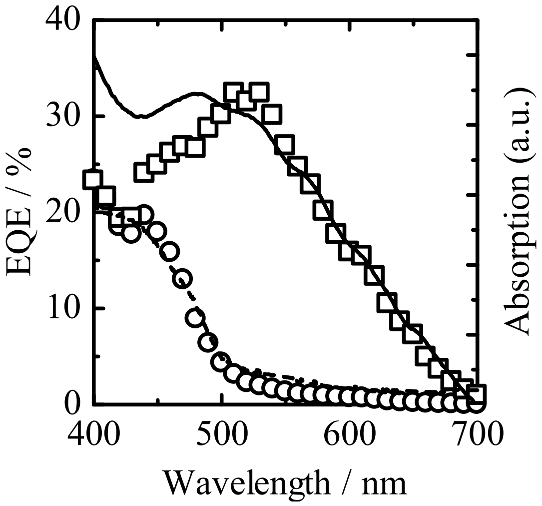

Figure 6–4. The external quantum efficiency spectra of the hybrid solar cell (open squares) and the LbL-based solar cell (open circles). The solid and broken lines represent absorption spectra of the hybrid solar cell and the LbL-based solar cell, respectively.

To address the origin of the photocurrent, the author measured the external quantum efficiency spectra of the hybrid solar cell (open squares) and the LbL-based solar cell (open circles). As shown in Figure 6–4, the action spectrum of the LbL-based solar cell was in good agreement with the absorption spectrum of PPV, suggesting that the photocurrent mainly originates from the PPV LbL layer. On the other hand, the action spectrum of the hybrid solar cell was consistent with the absorption spectrum of C_{70}:P3HT blend film (solid line) at the wavelength longer than 500 nm but slightly different around 400–500 nm. The longer wavelength range corresponds to the absorption of C_{70} and P3HT as shown in Figure 6–2. Therefore, the significant increase in J_{SC} is readily attributed to the improvement in photon absorption efficiency due to the introduction of the bulk heterojunction layer of C_{70}:P3HT as the author will discuss later.

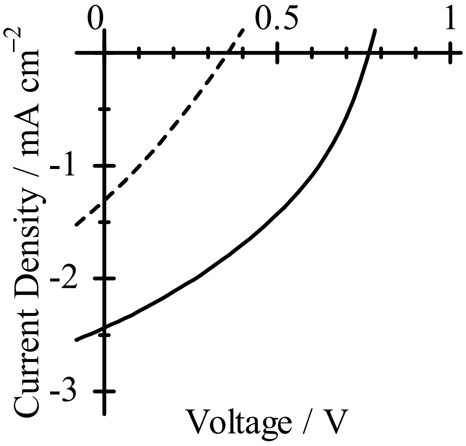

Figure 6–5. The *J–V* characteristics of photovoltaic devices with the PPV LbL layer with a layered structure of ITO|PEDOT:PSS|(PPV/PSS)$_{2.5}$|C$_{60}$:P3HT|Al (solid line) and without the PPV LbL layer with a layered structure of ITO|PEDOT:PSS|C$_{60}$:P3HT|Al (broken line) under AM1.5G simulated solar illumination at 100 mW cm^{-2} in the air.

Of particular interest is the relatively high V_{OC} >0.7 V of the hybrid solar cell. Recent studies have demonstrated that V_{OC} of bulk heterojunction solar cells is directly correlated with the highest occupied molecular orbital (HOMO) level of conjugated polymers.[13] The HOMO level of the PPV LbL film was estimated to be lower by ~0.2 eV than that of the C$_{60}$:P3HT blend film from UPS measurements. Thus, the observation of V_{OC} >0.7 V indicates that V_{OC} of the hybrid solar cell is governed by the PPV LbL thin layer rather than P3HT in the blend. To address the role of the PPV LbL thin layer in the hybrid solar cell, the author furthermore fabricated two photovoltaic cells with and without the PPV LbL thin layer: ITO|PEDOT:PSS|(PPV/PSS)$_{2.5}$|C$_{60}$:P3HT|Al (solid line) and ITO|PEDOT:PSS|C$_{60}$:P3HT|Al (broken line). Figure 6–5 shows *J–V* characteristics of the two photovoltaic cells under AM1.5G simulated solar illumination. In comparison with the photovoltaic cell without the PPV LbL layer, the hybrid solar cell with the PPV LbL layer showed remarkable improvements in J_{SC} and V_{OC}. The increase in J_{SC} is safely attributed to the light-harvesting effect of the PPV LbL layer, because the external quantum efficiency of the hybrid cell increased around 400–500 nm corresponding to the PPV absorption as shown in Figure 6–6. On the other hand, the increase in V_{OC} indicates that the PPV LbL layer effectively suppresses the charge recombination, as the author will discuss later.

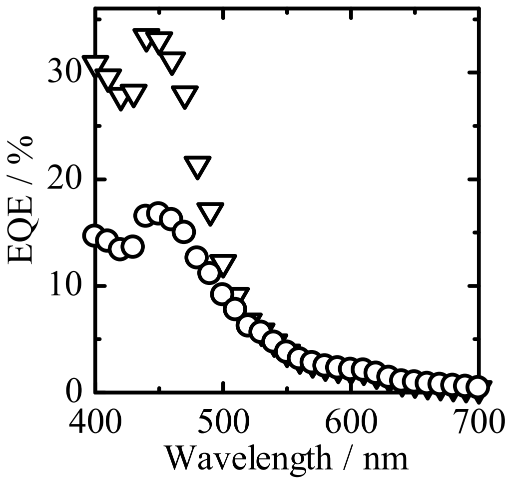

Figure 6–6. The external quantum efficiency spectra of the photovoltaic devices with the PPV LbL layer with a layered structure of ITO|PEDOT:PSS|(PPV/PSS)$_{2.5}$|C_{60}:P3HT|Al (open triangles) and without the PPV LbL layer with a layered structure of ITO|PEDOT:PSS|C_{60}:P3HT|Al (open circles).

6.3.2. *Thickness Dependence of LbL Layers*

The effect of light harvesting and suppressing in the charge recombination by the LbL layer should be dependent on the thickness of the LbL layer and materials employed in the layer. The author therefore fabricated two types of hybrid solar cells having different LbL layers with different thicknesses. One device employs the PPV/PSS LbL layer as a conductive material. The other employs PDDA/PSS LbL layer as an insulating material. Figure 6–7 shows the dependence of device parameters on the thickness of the LbL layer. For the hybrid solar cell with the PPV/PSS LbL layer, J_{SC} showed the maximum around 10 nm in thickness and V_{OC} saturated above 10 nm, resulting in the best performance at ~10 nm. This trend is consistent with the previous report for PPV-based multilayered polymer solar cells,[4] suggesting that the 10-nm-thick LbL layer completely covers the surface of the underlayer and prevents the direct contact between neighboring two layers. For the hybrid solar cell with the PDDA/PSS LbL layer, on the other hand, all device parameters steeply decreased with increasing thickness.

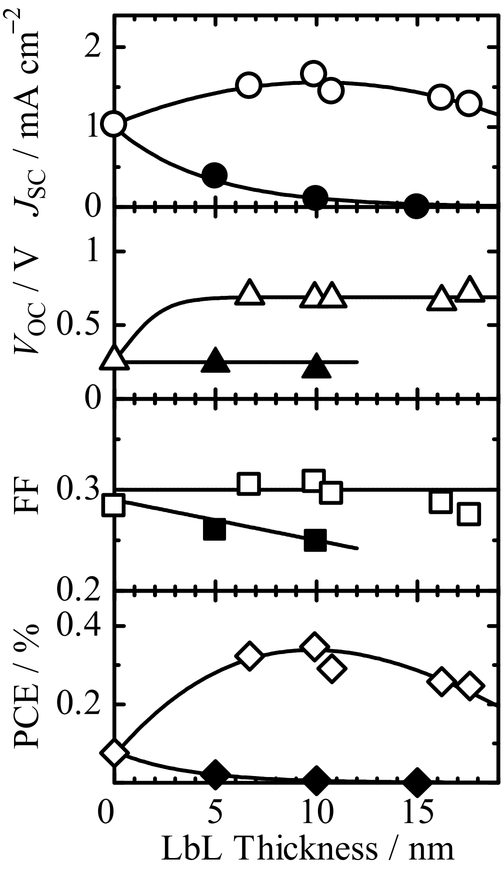

Figure 6–7. The thickness dependence of the device parameters for the hybrid solar cells with several PPV/PSS (open symbols) or PDDA/PSS LbL layers (closed symbols). The solid lines are guided just by eye.

6.4. Discussion

6.4.1. *Photon Absorption Efficiency*

Compared with the LbL-based solar cell, the hybrid solar cell exhibited significantly improved performance. As mentioned above, this was safely ascribable to the photon absorption extended to the longer wavelength by the introduction of light-harvesting materials such as P3HT and C_{70}. The extended action spectrum was similar to the absorption spectrum of C_{70} rather than that of P3HT. Considering the large fraction of C_{70} (>80 wt%) in the blend film, it can be safely said that the increase in the photon absorption efficiency is mainly due to C_{70} although the absorption coefficient α is about half of that of P3HT.[11,12,14] Furthermore, the absorption spectrum of the blend film cannot be reproduced by a simple spectral superposition of C_{70} and P3HT films shown in Figure 6–2, suggesting that the crystallinity of P3HT in the blend film is not so high that there should be amorphous domains because of the small fraction of P3HT (<20 wt%). The amorphous P3HT film presumably exhibits an absorption peak around 400–500 nm as is the case with that of a regiorandom P3HT film[15] or P3HT in solution as shown in Figure 6–2a. For P3HT/fullerene blend films, several research groups have reported that the device performance is much improved with the increase in the crystallinity of P3HT by careful selection of solvents,[16] solvent annealing,[17,18] blend ratio,[19] and thermal annealing.[20–23] Therefore, the amorphous P3HT domain with a low hole mobility may result in the relatively low efficiency in the photocurrent generation around 400–500 nm. The internal quantum efficiency around 500 nm was roughly estimated to be ~50% from the absorption of the blend film considering the reflection at the Al electrode. This is comparable to that for the PPV/C_{60} LbL heterojunction reported previously.[4]

6.4.2. *Role of the LbL Layer*

As mentioned above, J_{SC} showed the maximum when the thickness of the PPV LbL layer was around 10 nm. This thickness is consistent with the apparent exciton diffusion length the author reported previously, suggesting that PPV excitons in the LbL layer efficiently migrate to the interface of C_{60}:P3HT blend followed by the charge separation. The increase in the external quantum efficiency around 400–500 nm by the introduction of the PPV LbL layer is roughly comparable to that observed for the LbL-based solar cell reported before.[4] In other words, the PPV LbL layer can effectively contribute to the photocurrent generation irrespective of the presence of P3HT. On the other hand, the increase in V_{OC} suggests that the charge recombination is suppressed by the introduction of the LbL layer. The saturation of V_{OC} above 10 nm is also consistent with the previous study, indicating full coverage of the PPV LbL layer on the PEDOT underlayer. In bulk heterojunction solar cells, undesirable contacts may occur at each electrode interface. For example, as shown in Figure 6–8a, some fullerene domains in the blend may directly contact with the PEDOT layer. This contact would cause the reverse electron flow from Al to PEDOT through fullerene domains, resulting in the reduction in V_{OC}. The relatively low V_{OC} observed for the C_{60}:P3HT device without the PPV LbL layer may be ascribed to the direct contact of large C_{60} domains to the PEDOT layer because of the high C_{60} fraction (80 wt%). The PPV LbL layer introduced can effectively suppress the reverse electron flow owing to the lowest unoccupied molecular orbital (LUMO) higher than that of C_{60} or C_{70}, which also would lead to the improvement in V_{OC}. Furthermore, V_{OC} >0.7 V is rather comparable to that of the PPV-based solar cell. Recent systematic studies demonstrated that V_{OC} of polymer/fullerene bulk heterojunction solar cells is directly correlated to the HOMO level of the conjugated polymer[13] and the LUMO level of fullerene molecule;[24] V_{OC} is proportional to the energy difference between the HOMO and LUMO levels. In other words, the larger HOMO–LUMO difference would give the larger V_{OC} because the larger HOMO–LUMO difference can effectively suppress the current flow until higher forward voltages. On the basis of the correlation, V_{OC} of bulk heterojunction solar cells with PPV can be estimated to be larger by ~0.2 eV than that with P3HT (~0.6 eV), which is consistent with many experimental results.[1,16–23] This simple estimation is consistent with the observation of V_{OC} >0.7 V. The author should note that the lower HOMO level of PPV is thermodynamically unfavorable to the hole transport from P3HT to the PEDOT layer as shown in Figure 6–8b. Nevertheless, the device performance of the hybrid solar cell was improved. This is probably due to the small difference in the

HOMO levels between P3HT and PPV enough for the hole transport, because no improvement was observed for hybrid solar cells with PDDA/PSS LbL layers that are insulating materials with much lower HOMO levels. The energy difference is as small as ~0.2 eV but the resultant improvement in V_{OC} is substantial. Therefore, these findings suggest that V_{OC} is tunable by the introduction of ultrathin LbL layer of a conducting polymer with an appropriate HOMO level.

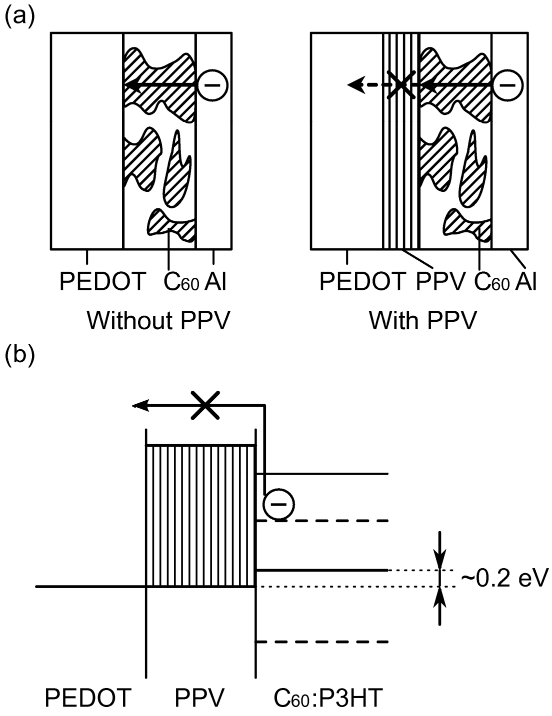

Figure 6–8. (a) Schematic illustrations of interfacial structures of polymer/fullerene blend. A large C_{60} domain directly contacts with the PEDOT layer as well as the Al electrode, which would result in the reverse electron flow indicated by arrow. (b) The energy diagram for a hybrid solar cell with the PPV-based LbL layer and the C_{60}:P3HT blend layer. The solid lines in the C_{60}:P3HT blend layer denote the HOMO and the LUMO levels of P3HT. The broken lines in the layer denote the HOMO and the LUMO levels of C_{60}. The energy difference between the HOMO level of PPV and P3HT is ~0.2 eV, which is thermodynamically unfavorable to the hole transport from P3HT to PPV.

6.5. Conclusions

The author fabricated hybrid organic solar cells integrating a PPV-based LbL ultrathin film with a P3HT/fullerene bulk heterojunction blend film, which exhibited PCE ~1% under AM1.5G simulated solar illumination. The introduction of the PPV-based LbL ultrathin layer to bulk heterojunction solar cells improved both J_{SC} and V_{OC} compared with a reference bulk heterojunction cell. The external quantum efficiency spectra showed that the PPV-based LbL ultrathin layer substantially contributed to the photocurrent generation around 400–500 nm while the blend layer >500 nm. The improved V_{OC} >0.7 V is higher than that achievable by P3HT-based bulk heterojunction solar cells, suggesting that V_{OC} of the hybrid solar cell is governed by the PPV-based LbL ultrathin film rather than the blend materials. These improvements showed the maximum when the PPV-based LbL layers was as thin as ~10 nm, which is comparable to the apparent exciton diffusion length and enough to prevent the direct contact between the neighboring layers. On the other hand, no improvements in J_{SC} or V_{OC} were observed for a hybrid solar cell with several LbL layers of insulating materials. Therefore, the author concludes that J_{SC} and V_{OC} can be improved by introduction of an ultrathin LbL layer of conducting polymers to bulk heterojunction solar cells. In particular, the finding suggests that V_{OC} is tunable by careful selection of a conducting polymer with an appropriate HOMO level and careful design of the thickness of the LbL ultrathin layer.

References

(1) Chen, H.-Y.; Hou, J.; Zhang, S.; Liang, Y.; Yang, G.; Yang, Y.; Yu, L.; Wu, Y.; Li, G. *Nat. Photonics* **2009**, *3*, 649–653.

(2) Kim, J. Y.; Lee, K.; Coates, N. E.; Moses, D.; Nguyen, T.-Q.; Dante, M.; Heeger, A. J. *Science* **2007**, *317*, 222–225.

(3) Ogawa, M.; Kudo, N.; Ohkita, H.; Ito, S.; Benten, H. *Appl. Phys. Lett.* **2007**, *90*, 223107.

(4) Benten, H.; Ogawa, M.; Ohkita, H.; Ito, S. *Adv. Funct. Mater.* **2008**, *18*, 1563–1572.

(5) Wakizaka, D.; Fushimi, T.; Ohkita, H.; Ito, S. *Polymer* **2004**, *45*, 8561–8565.

(6) Fushimi, T.; Oda, A.; Ohkita, H.; Ito, S. *J. Phys. Chem. B* **2004**, *108*, 18897–18902.

(7) Fushimi, T.; Oda, A.; Ohkita, H.; Ito, S. *Langmuir* **2005**, *21*, 1584–1589.

(8) Fushimi, T.; Oda, A.; Ohkita, H.; Ito, S. *Thin Solid Films* **2005**, *484*, 318–323.

(9) Haddon, R. C. *J. Am. Chem. Soc.* **1996**, *118*, 3041–3042.

(10) Haddock, J. N.; Zhang, X.; Domercq, B.; Kippelen, B. *Org. Electron.* **2005**, *6*, 182–187.

(11) Zhou, W.; Xie, S.; Qian, S.; Zhou, T.; Zhao, R.; Wang, G.; Qian, L.; Li, W. *J. Appl. Phys.* **1996**, *80*, 459–463.

(12) Kazaoui, S.; Minami, N.; Tanabe, Y.; Byrne, H. J.; Eilmes, A.; Petelenz, P. *Phys. Rev. B* **1998**, *58*, 7689–7700.

(13) Scharber, M. C.; Mühlbacher, D.; Koppe, M.; Denk, P.; Waldauf, C.; Heeger, A. J.; Brabec, C. J. *Adv. Mater.* **2006**, *18*, 789–794.

(14) Kim, Y.; Cook, S.; Tuladhar, S. M.; Choulis, S. A.; Nelson, J.; Durrant, J. R.; Bradley, D. D. C.; Giles, M.; McCulloch, I.; Ha, C.-S.; Ree, M. *Nat. Mater.* **2006**, *5*, 197–203.

(15) Jiang, X. M.; Österbacka, R.; Korovyanko, O.; An, C. P.; Horovitz, B.; Janssen, R. A. J.; Vardeny, Z. V. *Adv. Funct. Mater.* **2002**, *12*, 587–597.

(16) Vanlaeke, P.; Vanhoyland, G.; Aernouts, T.; Cheyns, D.; Deibel, C.; Manca, J.; Heremans, P.; Poortmans, J. *Thin Solid Films* **2006**, *511–512*, 358–361.

(17) Li, G.; Yao, Y.; Yang, H.; Shrotriya, V.; Yang, G.; Yang, Y. *Adv. Funct. Mater.* **2007**, *17*, 1636–1644.

(18) Li, G.; Shrotriya, V.; Huang, J.; Yao, Y.; Moriarty, T.; Emery, K.; Yang, Y. *Nat. Mater.* **2005**, *4*, 864–868.

(19) Nakamura, J.; Murata, K.; Takahashi, K. *Appl. Phys. Lett.* **2005**, *87*, 132105.

(20) Reyes-Reyes, M.; Kim, K.; Carroll, D. L. *Appl. Phys. Lett.* **2005**, *87*, 083506.

(21) Ma, W.; Yang, C.; Gong, X.; Lee, K.; Heeger, A. J. *Adv. Funct. Mater.* **2005**, *15*, 1617–1622.

(22) Li, G.; Shrotriya, V.; Yao, Y.; Yang, Y. *J. Appl. Phys.* **2005**, *98*, 043704.

(23) Kim, Y.; Choulis, S. A.; Nelson, J.; Bladley, D. D. C.; Cook, S.; Durrant, J. R. *Appl. Phys. Lett.* **2005**, *86*, 063502.

(24) Kooistra, F. B.; Knol, J.; Kastenberg, F.; Popescu, L. M.; Verhees, W. J. H.; Kroon, J. M.; Hummelen, J. C. *Org. Lett.* **2007**, *9*, 551–554.

Summary

In this thesis, the author designed and fabricated multilayered films by the layer-by-layer (LbL) deposition technique, and investigated the conductive and photovoltaic properties of those LbL films. The thickness of each layer in LbL films was controlled on a scale of nanometers, which is comparable with the hopping distance of charge carriers or the exciton-diffusion length. Therefore, the LbL films of fullerene or titanium oxide can be employed as effective electron-transporting films. Furthermore, the author discussed the correlation between internal nanostructures and the photovoltaic conversion process in multilayered solar cells, and optimized the structure of the solar cells.

In Chapter 1, the background and motivation of this thesis were described to clarify the significance of this thesis.

In Chapter 2, fullerene ultrathin films were fabricated by the LbL deposition, and were characterized in the layer structure and the conductive properties. Two types of water-soluble fullerenes were employed: one is an anionic fullerene $C_{61}(COO^-)_2$ (FDCA) and the other is a cationic fullerene $C_{60}C_2H_4N(CH_3)_2^+$ (FMAC). The fullerene ultrathin films were successfully deposited at nanometer precision by LbL assembly of PDDA/FDCA and FMAC/PSS. The monolayer thickness of FMAC in the LbL film was consistent with the shell thickness of FMAC vesicles in aqueous solutions, suggesting that fullerene LbL films consist of counter polymer films and fullerene bilayer films formed by rupture of fullerene vesicles. In terms of conductivity σ, and electron mobility μ_e, fullerene LbL films are comparable to C_{60}:PS blend films, suggesting that there exist effective percolating networks in the fullerene LbL films. Consequently, the LbL assembly of water-soluble fullerenes is useful for fabricating efficient electron-transporting ultrathin films of fullerene materials with a precisely-controlled thickness.

In Chapter 3, the author fabricated titania-based ultrathin films by the LbL assembly of TALH and PDDA or PPV where TALH was completely converted into TiO_x in the LbL films by thermal annealing at 95 °C for 24 h. The thickness of ultrathin films was successfully controlled by the LbL deposition on a scale of nanometers. The conductivity σ and the electron mobility μ_e of PDDA/TiO_x LbL films were as high as those of nanoporous TiO_2 film, suggesting that there exist effective percolating networks of TiO_x in the direction normal to the substrate in the LbL films. Furthermore, photovoltaic cells including TiO_x-based LbL films exhibited higher device performance than the reference cells with d-TiO_2 layer, suggesting that TiO_x-base LbL films in this chapter can serve not only as an electron-transporting but also an electron-accepting material.

In Chapter 4, the device performance was explained on the basis of the device structure in terms of all solution-processed organic thin-film solar cells consisting of a hole-transporting PEDOT:PSS layer, a light-harvesting PPV/PSS LbL layer, and an electron-transporting C_{60}:PS layer. First, the photon absorption efficiency was estimated by the transfer matrix method. It was demonstrated that the C_{60}:PS layer serves as an effective optical spacer to enhance the optical intensity in the light-harvesting layer. Second, the efficiency of exciton diffusion was evaluated using the one-dimensional diffusion model. As a result, the exciton diffusion constant to be 8×10^{-4} cm^2 s^{-1}, and the exciton diffusion length to be 10 nm, which is comparable to the optimized thickness of the PPV/PSS LbL layer. Third, the efficiency of exciton dissociation by charge transfer at a donor/acceptor interface was assumed to be η_{CT} ~1. Finally, the efficiency of charge collection to the electrodes η_{CC} was estimated to be ~0.5 for the PPV/PSS LbL layer with a thickness of >7 nm. These results demonstrated that the device performance can be quantitatively explained in terms of the device structure. Therefore, the author can rationally improve the device performance by optimizing the device structure on the basis of these device analyses, which is a great advantage of multilayered organic thin-film solar cells as reported for small molecule-based solar cells so far.

In Chapter 5, the optical properties of LbL films with MPS-PPV conjugated polymer were shown to be tuned by changing the solvent of LbL deposition. By using the water/DMSO mixed solution of MPS-PPV for the LbL deposition, the absorption at around 500 nm became more remarkable compared with the reference LbL film with MPS-PPV fabricated from the aqueous solution. As a result, J_{SC} of multilayered polymer solar cells was improved by >10% relative to the reference cell fabricated from the aqueous solution. Therefore, the light-harvesting efficiency of LbL-based multilayered solar cells can be improved by careful tuning of optical properties of LbL films.

In Chapter 6, the author fabricated hybrid organic solar cells integrating a PPV-based LbL ultrathin film with a P3HT/fullerene bulk heterojunction blend film, which exhibited PCE ~1% under AM1.5G simulated solar illumination. The external quantum efficiency spectra showed that the PPV-based LbL ultrathin layer substantially contributed to the photocurrent generation around 400–500 nm while the blend layer >500 nm. The improved V_{OC} >0.7 V is higher than that achievable by P3HT-based bulk heterojunction solar cells, suggesting that V_{OC} of the hybrid solar cell is governed by the PPV-based LbL ultrathin film rather than the blend materials. These improvements showed the maximum when the PPV-based LbL layers were as thin as ~10 nm, which is comparable to the apparent exciton diffusion length and enough to prevent the direct contact between the neighboring layers. Therefore, the author concludes that J_{SC} and V_{OC} can be improved by introduction of an ultrathin LbL layer of conducting polymers to bulk heterojunction solar cells. In particular, this finding suggests that V_{OC} is tunable by careful selection of a conducting polymer with an appropriate HOMO level and careful design of the thickness of the LbL ultrathin layer.

List of Publications

Chapter 2

"Fabrication and Conductive Properties of Multilayered Ultrathin Films Designed by Layer-by-Layer Assembly of Water-Soluble Fullerenes"

Masuda, K.; Abe, T.; Benten, H.; Ohkita, H.; Ito, S.

Submitted to *Langmuir*.

Chapter 3.

" Conductive and Photovoltaic Properties of Multilayered Ultrathin Films Designed by Layer-by-Layer Assembly of Titanium Oxides "

Masuda, K.; Morita, S.; Benten, H.; Ohkita, H.; Ito, S.

Submitted to *Thin Solid Films*.

Chapter 4.

"Exciton Generation and Diffusion in Multilayered Organic Solar Cells Designed by Layer-by-Layer Assembly of Poly(*p*-phenylenevinylene)"

Masuda, K.; Ikeda, Y.; Ogawa, M.; Benten, H.; Ohkita, H.; Ito, S.

ACS Appl. Mater. Interfaces **2010**, *2*, 236–245.

Chapter 5.

"Solution-Processed Multilayered Polymer Solar Cells Designed by Layer-by-Layer Assembly of Poly(*p*-phenylenevinylene)s with Dimethylsulfoxide "

Masuda, K.; Ikeda, Y.; Ohkita, H.; Ogawa, M.; Benten, H.; Ito, S.

Trans. Mater. Res. Soc. Jpn **2010**, *35*, 31–34.

Chapter 6.

"Hybrid Solar Cells of Layer-by-Layer Thin Film with Polymer/Fullerene Bulk Heterojunction"

Masuda, K.; Ogawa, M.; Ohkita, H.; Benten, H.; Ito, S.

Sol. Energy Mater. Sol. Cells **2009**, *93*, 762–767.

Other Publications.

"Surface Segregation at the Aluminum Interface of Poly(3-hexylthiophene)/Fullerene Solar Cells"

Orimo, A.; Masuda, K.; Honda, S.; Benten, H.; Ito, S.; Ohkita, H.; Tsuji, H.

Appl. Phys. Lett. **2010**, *96*, 043305.

Acknowledgements

The studies presented in this thesis were carried out at Department of Polymer Chemistry, Graduate School of Engineering, Kyoto University, Japan, from October 2006 to July 2010, under the guidance of Professor Shinzaburo Ito. The author expresses sincere gratitude to Professor Shinzaburo Ito for his kind guidance, valuable advices, and heartful encouragement thoughout this work, and for giving this oppotunity to do a PhD's work at his Laboratory. The author is deeply and heartily grateful to Associate Professor Hideo Ohkita for his kind supports, advices, and continuous discussion thoughout this work. So many ideas in this thesis were born from these fruitful discussion. The author is also indebted to Associate Professor Hiroyuki Aoki and Assistant Professor Hiroaki Benten for their valuable suggestions and discussion.

Professor Kazuo Akagi, Department of Polymer Chemistry, Graduate School of Engineering, Kyoto University, and Professor Yoshinobu Tsujii, Institute for Chemical Research, Kyoto University, are espesially ackowledged for their critical review of this thesis.

The author wishes to express his thanks to Dr. Li-Ting Lee, Dr. Hiroyuki Fujimoto, Dr. Michihiro Ogawa, and Dr. Jiamo Guo, for their attentive advices and helpful discussion. The author is also thankful to all members of Professor Ito's group for their active collaboration. The author is much obliged to Mrs. Aki Yamasaki for her assistance during the author's school life.

The author is deeply grateful to Mr. Masayasu Itoh, General Manager of Polymer Engineering Center, Ecology & Energy Laboratory, Research & Development Division, the Furukawa Electric Co., Ltd. for his reception and encouragement to the author's challenges.

The author is in acknowledgements of the Japan Student Services Organization, the 21st century COE program and the GCOE program for a United Approach to New Material Science for finantial support.

Finally, the author also expresses his heartful thanks to his parents, Teruji and Reiko, and his brothers, Yoshiharu and Atsushi, for their hearty assistances and encouragement.

Kohji Masuda

July 2010